PROBING THE NATURE OF DARK MATTER IN THE UNIVERSE

A Thesis
Submitted For The Degree Of
Doctor Of Philosophy
In The Faculty Of Science

by

Abir Sarkar

Under the supervision of

Prof. Shiv K Sethi
Raman Research Institute

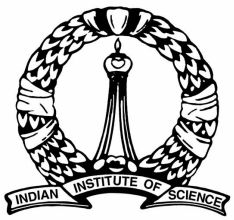

Joint Astronomy Programme (JAP)
Department of Physics
Indian Institute of Science
BANGALORE - 560012

JULY, 2017

Declaration

I, Abir Sarkar, hereby declare that the work presented in this doctoral thesis titled 'Probing The Nature of Dark Matter in the Universe', is entirely original. This work has been carried out by me under the supervision of Prof. Shiv K Sethi at the Department of Astronomy and Astrophysics, Raman Research Institute under the Joint Astronomy Programme (JAP) of the Department of Physics, Indian Institute of Science.

I further declare that this has not formed the basis for the award of any degree, diploma, membership, associateship or similar title of any university or institution.

Department of Physics
Indian Institute of Science
Bangalore, 560012
INDIA

Abir Sarkar
Date :

TO

My family,

without whose support this work could not be done

Acknowledgements

First and foremost I would like to thank my supervisor Prof. Shiv K Sethi in Raman Research Institute(RRI). He has always spent substantial time whenever I have needed for any academic discussions. I am thankful for his inspirations and ideas to make my Ph.D. experience productive and stimulating.

I am also grateful to our collaborator Prof. Subinoy Das of Indian Institute of Astrophysics, Bangalore, India. I am thankful to him for his insightful comments not only for our publications but also for the thesis.

I would also like to thank all the faculties at the Department of Astronomy and Astrophysics in Raman Research Institute and the Indian Institute of Science(IISc) astrophysics group for all the fruitful discussions and critical comments on various occasions throughout my Ph.D. career. A special mention goes to all the scientists who taught us in the first year course work of the JAP Ph.D. program.

Profound gratitude goes to all the administrative staffs of RRI and IISc physics department. Special thanks to Vidya, the ex-secretary of the Department of Astronomy and Astrophysics at RRI for helping me out with anything and everything regarding any administrative issues. I also greatly appreciate all the discussions and comments I have received from all my fellow Ph.D. students, the juniors and the juniors at both RRI and IISc.

Finally, but by no means least, loads of thanks go to my family members. They were always my strength in any emotional or spiritual matters. I would also like to convey my

gratitude towards my relatives in Bangalore who helped me enormously in settling down and also supported me a lot during my hard times in this city.

Synopsis

The dark matter is the most dominating matter candidate and a key driving force for the structure formation in the universe. Despite decade-long searches, the precise nature and particle properties of dark matter are still unknown. The standard cold dark matter candidate, the Weakly Interacting Massive Particle(WIMP) can successfully describe the large-scale features of the universe. However, when it comes to the scales comparable to a galaxy or a group of galaxies, it fails to explain the observations. The nature of the small-scale anomalies suggests a lower amount of dark matter at the scales of interest and can be tackled with different strategies. The simulation suites, used to produce the small-scale universe theoretically, can be equipped with varieties of baryonic phenomena, leading to a better agreement with observation. Another way is to use some new dark matter candidate altogether that reduces the small-scale power. Many such alternative dark matter candidates have been suggested and explored in the literature. The aim of the work presented in this thesis is to study the effects of small-scale power reduction due to new dark matter physics on different cosmological observables.

In Chapter 2 of this thesis, we have discussed the particle physics properties of three dark matter candidates proposed as alternatives of the WIMP. The first one is the Late Forming Dark Matter(LFDM), where dark matter is created due to a phase transition in the massless neutrino sector [1] long after the Big Bang Nucleosynthesis(BBN). Another candidate is the Ultra Light Axion Dark Matter(ULADM), which is born due to spontaneous symmetry breaking in the early universe and is stuck to its initial condition because of the Hubble drag. When the mass of the particle exceed the Hubble parameter, it decouples from the drag and starts behaving like dark matter [2], with a free-streaming length that is dependent on its mass. The last candidate we consider is the Charged Decaying Dark Matter (CHDM), which is born in

the radiation dominated era, after an instantaneous decay of a massive charged particle [3]. All of these dark matter candidates suppress small-scale power, though because of different physical reasons. In the next three chapters, we have studied their effects on various cosmological observables. The methods of study, along with the data used to validate the theoretical predictions and results are discussed below.

Chapter 3:

This chapter is based on the work performed in [4]. In this chapter, we focus on the LFDM and study its effects on linear matter power spectra at both small and large scales.

Method of Study: The LFDM model is specified by two parameters: The effective massless neutrino degrees of freedom(DOF) $N_{\rm eff}$ and the redshift of formation z_f. We have generated a set of matter power spectra using publicly available code `CAMB` for different sets of $N_{\rm eff}$ and z_f, and performed a χ^2 analysis using matter power spectrum data to constrain the model parameters. We have also considered a scenario, where a fraction $f_{\rm lfdm}$ of the total dark matter is LFDM and repeated the exercise. We have computed multi-parameter contours and posterior probabilities by marginalization over redundant parameters that allow us to estimate the model parameters.

The Data: The two parameters—z_f and $N_{\rm eff}$—affect the linear power spectrum at different scales. The main impact of changing $N_{\rm eff}$ is to alter the MRE epoch, shifting the peak of the matter power spectrum, which is located at $k \simeq 0.01\,{\rm hMpc}^{-1}$ in the standard model of cosmology. We use the SDSS DR7 data [5] for our analysis. As the SDSS data on the galaxy power spectrum gives the power at scales: k=0.02–0.1 h/Mpc, this data is sensitive to the variation of $N_{\rm eff}$. On the other hand, the main effect of formation redshift z_f is to suppress the power at scales $k > 0.1\,{\rm h/Mpc}$. In this scales, we use the linear matter power spectrum, reconstructed from Lyman-α forest power spectrum in the range: $0.2 < k < 4.8\,{\rm h/Mpc}$ from [6,7]. We use 45 band-powers from the SDSS galaxy data and 12 points from the reconstructed linear power spectrum from the Lyman-α data.

Results: Our results can be summarized as follows. If all the presently observed CDM is late forming, then both the data sets lead to upper limits on the redshift of formation of LFDM, with Lyman-α data resulting in tighter bounds: $z_f < 3 \times 10^6$ at 99% confidence limit.

On the other hand, if we allow only a fraction of the CDM to form at late times, then we improve the quality of fit as compared to the standard ΛCDM model for the Lyman-α data. This is suggestive that the present data allows for a fraction 30% of the CDM to form at $z_f \simeq 10^5$. Therefore, our result underlines the importance of the Lyman-α data for studying the small-scale power spectrum in alternative dark matter regime.

Chapter 4:

This chapter is based on the work performed in [8]. Here, we have studied the effects of small-scale power suppression on the Epoch of Reionization(EoR) and the evolution of collapsed fraction of gas at high redshift. We have considered two of the alternative dark matter candidates discussed in Chapter-2 in this chapter: the LFDM and the ULADM.

Method of Study: Our method of constructing the reionization fields consists of three steps: (i) Generating the dark matter distribution at the desired redshift, (ii) Identifying the location and mass of collapsed dark matter halos within the simulation box, (iii) Generating the neutral hydrogen map using an excursion set formalism. The assumption here is that the hydrogen exactly traces the dark matter field and the dark matter halos host the ionizing sources. Given the uncertainty of reionization history, we do not assume a particular model for reionization history $\bar{x}_{\rm HI}(z)$, where $\bar{x}_{\rm HI}$ is the fraction of neutral hydrogen in the universe. Instead, we fixed the redshift at $z = 8$ and the ionization fraction at $\bar{x}_{\rm HI} = 0.5$ and compared these models. We have produced HI power spectra, and photon brightness temperature fluctuation(δT_b) maps to compare the alternative models with the standard ΛCDM model. We discard the models where no halo is formed to host the ionizing sources, or an absurdly high number of ionizing photon is necessary to make $\bar{x}_{\rm HI} = 0.5$ at $z = 8$ successfully.

The collapsed fraction, defined as the fraction of collapsed mass in haloes with masses larger than a threshold mass M at a redshift z, is sensitive to the mass function of the haloes. As obtaining the mass function from N-body simulation is numerically expensive, we integrate the Sheth-Tormen mass function above the density threshold of collapse at a given redshift for computing the collapsed fraction in case of LFDM models. For computing the collapsed fraction for ULADM models, we integrate the halo mass functions derived by [9]. The collapsed fractions are calculated for two threshold halo masses, $10^{10} M_\odot$ and $5 \times 10^{10} M_\odot$ in the redshift

range $2 < z < 5$ and compared to observational data. Models that are unable to produce the observed collapsed fractions at high redshifts are discarded.

The Data: From absorption studies of the Damped Lyman-α(DLA) clouds, the evolution of average mass density of HI in the universe can be inferred. Assuming that the collapsed fraction of baryons traces dark matter, this allows us to get an approximate measure of the minimum amount of collapsed fraction of the total matter in the redshift range $2 < z < 5$. We have used the data of density of gas trapped in DLAs (Ω_{HI}), at the mentioned redshift range from [10, 11] and converted them to collapsed fraction of gas. The re-constructed collapsed fractions are used to compare the theoretical predictions.

Results: Our method predicts an 'inside-out' reionization where the high-density regions are ionized first. We find that the HI power for LFDM and ULADM models is greater than the ΛCDM model over a large range of scales $0.1 < k < 4\,\mathrm{Mpc}^{-1}$. In the maps of δT_b, there are two main differences between ΛCDM and alternative models. The size of the ionized regions is larger in the LFDM (ULADM) models and the HI fields have stronger density contrast. Checking the facts that halos are actually formed to host stars and a realistic number of ionizing photons are produced to achieve the desired level of ionization, we put a rough limit on $z_f \sim 4 \times 10^5$ and $m_a \simeq 2.6 \times 10^{-23}$ eV as lower cut-offs. Comparing the estimated collapsed fraction with data we found weaker constraints on $z_f \lesssim 2 \times 10^5$ and $m_a \lesssim 10^{-23}\,\mathrm{eV}$. All these constraints are in good agreement with previous constraints.

Chapter 5:

This chapter is based on the work performed in [12]. The observable of interest here is the spectral distortion in the Cosmic Microwave Background(CMB).

Method of Study: The distortion on the CMB spectra can occur due to heating or cooling of the medium owing to several mechanisms at different times in the history of the universe. In this work, we consider heating due to the dissipation of acoustic waves, well-known as the Silk Damping. The fraction of energy injected into the photon bath is a function of the evolution of the fluctuation in gravitational potential Φ and the CMB dipole Θ_1. We have computed the evolution of Φ and Θ_1 for all the three dark matter candidates studied in Chapter 2, along with the WDM, using the publicly available code `CMBFAST` and `axionCAMB`. Using them, we

estimate the evolution of the heating rate and integrate it to get the distortion parameters. The distortion parameters thus found are used to calculate the distorted CMB spectrum. The final output is the percentage change of the distortion parameters for the alternative dark matter models with respect to the ΛCDM model.

Results: The two earlier spectral distortions, namely the μ- and the i-distortion, are not found to be affected due to new dark matter physics. The y-distortion is the only one that carries the signatures of small-scale power suppression. We conclude that, unless the constraints on the model parameters found in previous studies are violated, the change in the y-distortion parameter is not more than $\sim 14\%$ compared to the standard model with identical spectral shapes. y-distortion occurring from later phenomena, i.e., structure formation and tSZ effects in the galaxy clusters have orders of magnitude higher distortion parameters than the Silk Damping, again with the same spectral shape. Thus, unless these foregrounds are understood and cleared correctly, distinguishing between dark matter candidates which reduce small-scale power is next to impossible.

Finally, our study shows that changing matter power at small scales can have noticeable impacts on other observables of the universe. However, to see the difference, the phenomena themselves are to be understood properly. The constraints found on the models using different probes are in good agreement with each other. In future, we will extend our research by investigating whether it is possible to accommodate an O(10 eV) particle as a dominating cold dark matter candidate, by exploring its effects on linear matter power spectrum and CMB spectral distortion.

List of Publications

1. Abir Sarkar, Subinoy Das, Shiv K. Sethi, "How Late can the Dark Matter form in our universe?", JCAP 03(2015)004, arXiv:1410.7129

2. Abir Sarkar, Rajesh Mondal, Subinoy Das, Shiv.K.Sethi, Somnath Bharadwaj, David J. E. Marsh, "The effects of the small-scale DM power on the cosmological neutral hydrogen (HI) distribution at high redshifts ", JCAP 04(2016)012, arXiv:1512.03325

3. Abir Sarkar, Shiv.K.Sethi, Subinoy Das "The effects of the small-scale behaviour of dark matter power spectrum on CMB spectral distortion", JCAP 07(2017)012, arXiv:1701.07273

Abbreviations

DM - Dark Matter

C(H,W)DM - Cold(Hot, Warm) Dark Matter

SUSY- Supersymmetry

WIMP - Weakly Interacting Massive Particle

LFDM - Late Forming Dark Matter

ULADM - Ultra Light Axion Dark Matter

CHDM - Charged Decaying Dark Matter

BBN - Big Bang Nucleosynthesis

MRE - Matter-Radiation Equality

CMB - Cosmic Microwave Background

EoR - Epoch of Reionization

HI - Neutral Hydrogen

DLA cloud - Damped Lyman-α cloud

SD - Silk Damping

COBE - Cosmic Background Explorer

WMAP - Wilkinson Microwave Anisotropy Probe

SDSS - Sloan Digital Sky Survey

PIXIE - Primordial Inflation Explorer

MW - Milky Way

L(S)MC - Large(Small) Magellanic Cloud

VDF - Velocity Distribution Function

dSph -Dwarf Spheroidal

Notations

m_e - Mass of the electron

m_p - Mass of the proton

k_B - Boltzmann's Constant

c - Velocity of light in vacuum

c_s - The speed of sound

$M_\odot$ - 1 Solar Mass $= 2 \times 10^{30}$ kg

z - Redshift

$a - 1/(1+z)$ - Scale factor of the universe

$z_{\rm eq}$ - Redshift of matter-radiation equality

$a_{\rm eq}$ - Scale factor at matter-radiation equality

η - Conformal time

H_0 - Hubble Constant at present

h - $H_0/100\,{\rm kms}^{-1}{\rm Mpc}^{-1}$

ρ_i - Background density of a component i of the universe

$\Omega_i - \rho_i/\rho_c$ - Density parameter of a component i of the universe

$\delta_i - \delta_{\rho_i}/\rho_i$ - Density fluctuation of a component i of the universe

θ_i - Velocity fluctuation of a component i of the universe

i - dm, wdm, b, HI , γ, ν for dark matter, warm dark matter, baryon, neutral hydrogen, photon and massless neutrino respectively

A_s - Amplitude of the power spectrum

n_s - Scalar spectral index of the power spectrum

σ_8 - mass dispersion at scale $R = 8\,{\rm h}^{-1}{\rm Mpc}$ at the present epoch

$m_{\rm wdm}$ - Mass of the WDM

$k_{\rm fs}$ - Free-streaming scale of the WDM

m_s - Mass of sterile neutrino

C_l - The CMB power spectrum amplitude

$\rho_{\rm lfdm}$ - Density of the LFDM

$N_{\rm eff}$ - Effective degrees of freedom of massless neutrino

z_f - Formation redshift of the LFDM

$f_{\rm lfdm}$ - Fraction of the LFDM in the universe

$k_{\rm lfdm}$ - Scale that enters the horizon when dark matter is formed

m_a - Mass of the the ULADM

k_m - Free-streaming scale of the the ULADM

$z_{\rm decay}$ - Redshift at which the CHDM is formed

k_e - Scale that enters the horizon at a certain time

$P(k)$ - Linear Matter Power Spectrum

$\Delta^2(k)$ - Dimensionless 3D Matter Power Spectrum

$\frac{dn}{d\ln M}$ - Halo mass function i.e, Number of haloes on a certain interval of mass

$\bar{x}_{\rm HI}$ - Fraction of neutral Hydrogen

$N_{\rm ion}$ - The number of ionizing photons emitted per baryon

δT_b - The photon brightness temperature fluctuation

$\Delta_b^2(k)$ - Brightness Temperature Power Spectrum

$N(Hi)$ - Column density of neutral hydrogen $f_{\rm coll}$ - Collapsed fraction of gas in haloes

σ_M - Mass dispersion of haloes

$n(\nu, t)$ - Photon distribution function

T_e - Temperature of electron

T_γ - Temperature of photon

n_e - Number density of electron

σ_T - Thomson scattering cross-section

ν - Frequency of the incident photon

$x(x_e)$ - Dimensionless frequency of photon(electron)

μ - Chemical potential of photon and the amplitude of the μ-distortion

y - Compton y-parameter and the amplitude of the y-distortion

R - The baryon loading factor defined as $R = 3\rho_b/4\rho_\gamma$

τ_c - Compton scattering optical depth

k_d - The scale that undergoes Silk damping at any time

$\Theta_1(k, \eta)$ - CMB dipole transfer function at a certain conformal time

Θ_{1D} - $\Theta_1(k = k_d)$

$\Phi(k, \eta)$ - Fluctuation of the cosmological gravitational potential at a certain conformal time

S_{SD} - The source function of heating due to Silk Damping

η_d - The conformal time at which the scale k_d undergoes Silk damping

Contents

List of Figures

List of Tables

Chapter 1

Introduction

Since the initiation of the civilization, humans have an infinite amount of curiosity about the world that is outside the homely planet earth. Through millennia many astronomers in different countries of the world have explored the night sky with telescopes and even naked eyes that helped them to find answers to some questions about the part of the universe immediately surrounding our planet. However, the vast universe outside our galaxy, The Milky Way(MW), remained beyond our vision for a very long time. Only recently, we have gathered enough theoretical understanding and experimental tools that have enabled us to visualize the beautiful and exciting world that is located outside the MW, leading to explore the universe as a whole and thus giving birth to the subject, Cosmology. Earliest research works in Cosmology trace back to early 1900. This classic subject of Physics tries to address the long wondered questions of humankind considering the universe as a whole. The famous paper of Albert Einstein in 1917 undoubtedly announced the birth of the subject we know today as Theoretical Cosmology. The century following has witnessed exciting progress in this field that has enriched human knowledge about the universe, turning it into a mainstream subject of Physics with many activities going on. The efforts of decades have come fruitful in various aspects, and we indeed gathered sufficient knowledge about the behavior of the universe as a whole. The first satellite that was dedicated to Cosmological observations was the Cosmic Background Explorer(COBE) which operated from 1989 to 1993. After the results obtained from the COBE mission, the theoretical predictions about the Cosmic Microwave Background (CMB) anisotropy got observational confirmation. The cosmological parameters were measured and constrained by the Wilkinson Microwave Anisotropy Probe(WMAP) experiment and almost pinpointed by the latest Planck

mission.

Despite getting such a sound knowledge about the universe, there are even more things those are still covered in the veil of mystery. One of the most exciting of these unknowns is the nature of the dark matter. This mysterious component of the universe reveals its presence through gravitational interaction only. The existence of the dark matter was first suspected by Dutch astronomer Jacobus Kapteyn in 1922 [13] while studying the distribution of mass the dynamics of stars in the local stellar neighborhood. The suspicion was strengthened by the radio astronomy pioneer Jan Oort in 1932 [14] and Fritz Zwicky in 1933 [15], independently. However, the existence of dark matter was found to be a possible reality by the observations of galactic rotation curves almost forty years after the works of Oort and Zwicky. The galaxy rotation curve is the distribution of orbital velocities of visible components of the galaxy. Now, the density of visible matters decreases as one goes further away from the galactic center, implying that the rotational velocity should fall at larger distances from the center. Several observations of the galaxy rotation curve were carried out using different tracers during the '70s and '80s by many astrophysicist groups, notably by Vera Rubin and A. Bosma. These observations revealed flat rotation curves instead of sharply falling curve at the outskirts of many galaxies, suggesting that either there is a large chunk of non-luminous matter in the outer parts of the galaxies or the Newtonian dynamics is modified there. Later, in the '90s the gravitational lensing observations in larger objects, like galaxy clusters, established that not only dark matter exists, but it can also be a key controlling factor of structure formation. The CMB observations performed by WMAP and Planck also favored a universe where dark matter is the dominating matter candidate. However, unfortunately enough, none of them has been able to shed any light on its fundamental particle nature.

Several dark matter candidates have been suggested so far. They can be majorly divided into two classes: baryonic and non-baryonic. The baryonic candidates consist of faint stars, planets, cold gas clouds and the warm-hot intergalactic medium. However, they did not seem to be very promising as dark matter candidates from theoretical grounds. Furthermore, some surveys found they have too little abundance to account for the entire dark matter of the universe. For non-baryonic dark matter, well-studied candidates are neutrino, axion, supersymmetric particles, mirror matter and so on. The most popular class of non-baryonic dark matter candidate is the Weakly Interacting Massive Particle(WIMP), encouraged by the well-known WIMP

miracle in the supersymmetric extension of the standard model of particle physics. The WIMP dark matter is very efficient in describing the large-scale structure of the universe. However, when it comes to scales as small as a galaxy or a group of galaxies, it fails to explain the observed facts. Furthermore, the detectors dedicated to estimating the mass of WIMP are also providing conflicting results.All these issues have inspired a drive to go beyond the standard WIMP picture of dark matter and consider alternative candidates for dark matter, which differ from WIMP on galactic scales (while reproducing its success on cosmological scales). One of such alternatives is the Warm Dark Matter(WDM), which also failed to solve the small-scale issues thoroughly.

The primary focus of this thesis is to probe the nature of dark matter by studying the effects of some alternative dark matter models on some important cosmological observable. After the inflation had taken place, it generated small density perturbations in the seemingly homogeneous and isotropic universe. The perturbations grew with time and formed the present-day structures. The properties of these density fluctuations are best studied by the power spectrum, which is the Fourier transform of the correlation function of the density fluctuations of several components that build the universe. Depending on how it was created, the dark matter can change the matter power spectrum at certain scales, preferably at scales comparable to the galactic scale as well as considerably smaller than the one that entered the horizon during matter-radiation equality(MRE). The modification of small-scale matter power spectrum has other interesting observational consequences which are possible probes of the nature of the dark matter.

The purpose of writing this chapter is to motivate the need of finding an alternative of WIMP. Therefore, we start this chapter by discussing the emergence of the concept of dark matter in Section 1.1. In Section 1.2, we discuss why the dark matter is inevitable for structure formation, and it must be non-relativistic(cold) in nature to successfully form the structures. We describe some potential dark matter candidates, both baryonic and non-baryonic, in Section 1.3. In Section 1.4, the principles of detection techniques of the dark matter are covered, with some recent results produced by these experiments. Section 1.5 argues the astrophysical problems with the standard WIMP dark matter, which is the first stepping stone for thinking about an alternative. In Section 1.6, we have discussed how these problems can be overcome using new dark matter candidates and including baryonic physics. The most studied alternative

of WIMP is the WDM, but as shown in the same section, it does not have enough potential to solve the problems either. Thus, we argue that it is necessary to go beyond WDM a look for some other alternative. The chapter concludes with a layout of the rest of the thesis, in Section 1.7.

1.1 The Emergence of Dark Matter in Astrophysics and Cosmology

At present, it is well established that the dark matter is present in the universe covering all scales ranging from galaxies and to vast superclusters. The presence of dark matter in different astronomical objects was revealed by various observational techniques, and it took decades of research to establish the fact that not only it exists, but is also the most dominating matter candidate of the universe. In the rest of this section, we provide a brief overview of the research works that answer the first question to motivate the thesis: "Why is the presence of dark matter unavoidable?"

1.1.1 Dark Matter in Galaxy

Rotation Curve of Galaxies

The existence of the dark matter was suspected in the MW galaxy for the first time by Jacobus Kapteyn in 1922 while studying the distribution of rotational velocities of stars at the outskirts of the galaxy. Babcock in 1939 [16] measured the rotation of the nearest big galaxy to us, the Andromeda galaxy (M31), using optical spectroscopy. It was found that the rotational velocity at long distances from the center was enormous and the total luminous matter present at the outskirt was not enough to give rise to such a high rotational velocity. These works together initiated the idea of dark matter which had to wait for forty more years to get solid physical ground. Furthermore, in 1959, Kahn and Woltjer [17] also studied the dynamics of the Local group by calculating the relative velocity of the MW and M31. They concluded that the system could only be dynamically stable if the system contains a considerable amount of intergalactic matter, which is preferably dark and has a very tiny fraction of stars.

In the 1970s, the existence of dark matter was confirmed by numerous observations of rotation curves of local galaxies in different wavebands by several groups. These observations

turned the mere concept of dark matter into a well-recognized field of active research. Optical and 21 cm emission studies of M31 during the '70s by various research groups [18–20] confirmed that a significant fraction of the mass of the galaxy is located in the outer part in the form of a dark halo. Kinematic investigations by [21, 22] of two other giant spirals M81 and M101 led to similar conclusions. These observations indicated that dark matter was not any particular content of MW but is present other galaxies too, irrespective of the fine details of their morphology. Ostriker and Peebles [23] performed a numerical study of the effect of dark matter on the stability of the Galactic disk. They found that models that start with disk characteristics of the MW and without a dark halo, rapidly evolve to unstable barred modes. On the other hand, if the galaxies are embedded in dark spherical halos with mass ~ 2.5 times the disk mass, the evolution is stable, which further confirmed the inevitability of dark matter.

In [24] the first indication of the existence of non-luminous matter in dwarf galaxies was shown by studying the nature of their tidal mass distribution, again derived from the rotation curve. Later, more studies [25,26] using better data demonstrated that not only dwarf galaxies contain dark matter, they are also dominated by dark matter. The first evidence of dark matter in elliptical galaxies came by the work of Stewart et al. in 1984 [27]. They studied the X-ray images and spectra of the elliptical galaxy M87, which is embedded in a large galactic halo in the Virgo Cluster. They calculated gravitational potential distribution around the galaxy and used it to simulate sample spectra to compare with observed spectra. It was seen that models with halo radius with a few tens of kpc match best with the observed spectra, suggesting an association of dark matter with the galaxy. The study was extended to many other ellipticals [28] and confirmed the existence of dark matter as the dominating candidate in all of them.

Hence, the two decades 1970 and 1980 formally gave the birth of dark matter which later proved to be inevitable for the present day structures to form.

Velocity dispersion of stars in elliptical galaxies

The stars in galaxies form bound systems that follow the virial theorem. Their velocity dispersion σ is related to the enclosed mass(M) and the distribution of mass in the halo where they are located. Different astrophysical systems have different $\sigma - M$ relations. For giant elliptical galaxies, the kinematics of stellar systems are dominated by random motions [29]. The velocity

dispersion of stars and their variations with radius is thus a messenger of the mass distribution in the ellipticals. However, there are two significant caveats. First, the outer parts of elliptical galaxies are too faint to provide enough data about the stellar kinematics in those regions, making it difficult to obtain information about the mass distribution. Second is the lack of knowledge about the nature of stellar orbits in the ellipticals. A poor fit of data with a mass model constructed with only luminous matter cannot, therefore, assure the existence of a dark halo.

In Figure 1.1 we show the velocity dispersion data of four elliptical galaxies, NGC 2434, 2663, 3706 and 5018 taken by Carollo et al. in 1995 [30]. It is evident that for all the galaxies apart from NGC 2663, the velocity dispersion decline slowly or remain flat in the outer regions. If the outer parts of the galaxies would contain only luminous matter or dominated by them, the velocity dispersion would decline more rapidly. This phenomenon can also be explained by the domination of tangential component of velocity dispersion of stars in the outer parts of the galaxy, as an alternative of this apparent existence of a dark halo. If velocity dispersion is dominated by tangential component, the radial counterpart will indeed seem to be falling slowly. In the lower panel of Figure 1.1, the radial profiles of one of the truncated Gauss-Hermite parameters(z_4) [31] are shown. If the tangential component indeed dominates the velocity dispersion of stars at the outskirt of the galaxy, the observed nature of z_4 predicts a steeply falling σ. However, the gentle fall of σ, as seen in Figure 1.1, rules out the possibility of tangential isotropy of orbits and confirms the existence of a dark halo for three of the four galaxies. For the galaxy, NGC 2663, the steep fall of σ does not assure a believable existence of a dark halo.

1.1.2 Gravitational Lensing and the Galaxy Clusters

The gravitational lensing is a vastly used technique to measure the mass of a distant massive object. When light from any background source comes through a massive object(Conventionally called the lens), for example, a galaxy cluster, its trajectory gets distorted due to the mass of the lens. Because of this, the image of the source can be elongated producing Einstein's rings, get sheared, or even multiple images can form depending on the nature of the lens. If the source is located directly behind the lens, the light from the source face the extremely complex space-time right near the lens and traverse many trajectories before reaching the telescope.

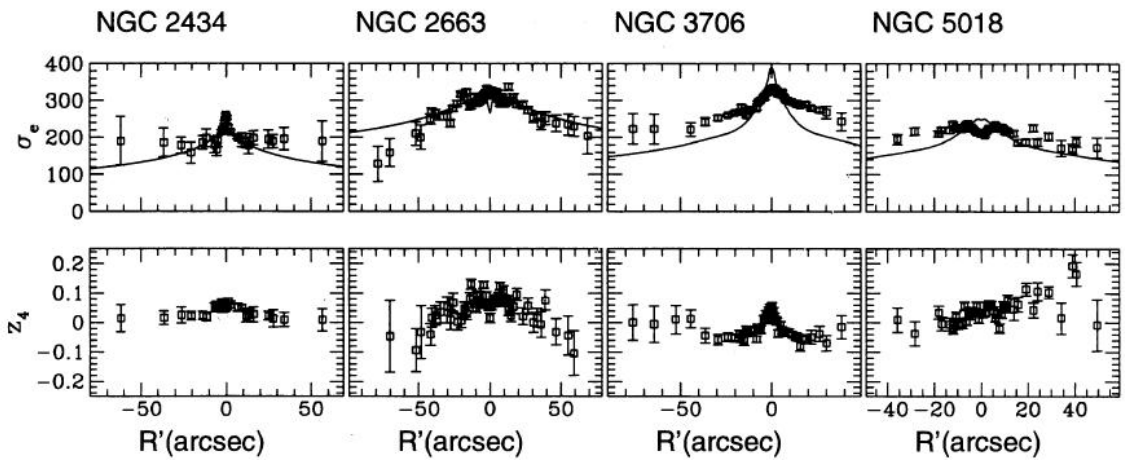

Figure 1.1: Velocity profile parameters of four elliptical galaxies, NGC 2434, 2663, 3706 and 5018, as a function of the effective radius projected on the Sky. Top Panel: The dispersion of the velocity σ_e and Bottom panel: the Gauss-Hermite parameter z_4. The picture is taken from [30].

This is called Strong Gravitational Lensing. If the lens is circular in nature, it gives rise to beautiful ring-like images of the source, called the Einstein's rings(Please refer to [32] for a nice review of strong gravitational lensing). On the contrary, if the source is far from the center of the cluster, the light path does not deflect very much, and the image is modified slightly by shear, amplification, and rotation. This is called Weak Gravitational Lensing [33, 34]. The amount of distortion depends crucially on the mass of the lens, and thus the measurement of the distortion can give a reasonable estimate of the mass of the lens.

The presence of dark matter in galaxy clusters was first suggested by Sinclair Smith in 1936 [35] who calculated the mass of the Virgo cluster from the line of sight velocity distribution function(VDF) of the cluster. The average mass of each galaxy calculated showed a discrepancy of ~ 200 that can be expected from Hubble's estimate that was then available. Also, the VDF shows no relation between the luminosity of the object and their velocity.

The next work on measuring the mass of another galaxy cluster, this time the Coma cluster, by the pioneering paper of Fritz Zwicky in 1937 [36], rose further suspicion. The paper contains an investigation of the luminosity data of the Coma Cluster taken by Schmidt Telescope in Mount Palomar, directed to model the Coma cluster theoretically. Assuming that the cluster is virialized, he found a discrepancy of a factor of 500 in the mass of individual galaxies, termed

as nebulae in the original paper. This was another indication that the luminous matter is a tiny fraction of total mass in galaxy clusters, though the discrepancy factors were very high for both the clusters because of low-quality data available at that time. He also noticed that the number density of nebulae in the cluster is very high near the core and decreases gradually in the outer parts of the cluster providing a much larger extension of the cluster than estimated by Hubble.

In the very paper by Zwicky, the idea of estimating the mass of galaxy clusters by gravitational lensing was first suggested, though the real observations started coming after almost 40 years. The first observation of gravitational lensing was made by Walsh et al. [37] in 1979. The strong gravitational lensing was first observed in 1987 [38] whereas the weak gravitational lensing was first observed by in 1990 [39]. The weak lensing observations in the '90s not only confirmed the existence of dark matter in clusters but also turned out to be a promising tool to map the dark matter distribution in galaxies using gravitational lensing. Recently, an observation made in 2006 [40] on 1E 0657-558, a unique cluster merger at z=0.296, demanded a direct detection of dark matter in that cluster. At present both strong and weak lensing are widely used to map the dark matter distribution in the galaxy clusters [41, 42].

1.2 Dark matter in Cosmology

In the last section, we have discussed how the existence of dark matter was found in galaxies and clusters of galaxies. However, today we know that it is the most dominant matter candidate of the universe and the key component to the structure formation. To appreciate the fact that, without dark matter, it would not be possible to form the structures as we see today, it is necessary to understand the dynamics of the building blocks of the universe. Below, is Section 1.2.1, we provide a brief description of the evolution of the components of the universe and show that dark matter is essential for structure formation and it has to be cold in nature. We also put emphasis on the fact that it is the cosmological evidence and not the galactic evidence that can provide information about the nature of dark matter. We have studied the effects of dark matter on the matter power spectrum and the CMB temperature power spectrum. The behavior of these two quantities is crucially dependent on a handful of cosmological parameters. The parameters are: The baryon density parameter Ω_b, the total

matter density parameter Ω_m, the curvature density Ω_K, the Hubble parameter h, the slope of the primordial power spectrum n_s, the amplitude of the primordial power spectrum A_s, and the effective neutrino degrees of freedom(DOF hereafter) $N_{\rm eff}$. We have computed these quantities using the publicly available simulation package `CAMB` [43]. Throughout this thesis, we have used the Planck TT+lowP best fit values of cosmological parameters: $\Omega_b h^2 = 0.02222$, $\Omega_m = 0.315$, $\Omega_K = 0.0$, $h = 0.6731$, $n_s = 0.9615$, $\ln(10^{10} A_s = 3.089$ and $N_{\rm eff} = 3.046$.

1.2.1 Structure Formation

The drivers of the evolution of the universe at present are the dark energy(covering up 68.3% of the ingredients of the universe) and the dark matter (contains 26.8% of the universe). The rest $\sim 4\%$ consist of the baryons, most of which is invisible, along with the neutrinos and the photons. The cosmological perturbation theory studies the evolution of the constituents of the universe. Depending on their transformation properties, there are three kinds of perturbations present in the universe: scalar, vector, and tensor perturbations. Out of these, it is the scalar perturbation that is relevant in the context of the structure formation in the universe. The evolution equations of different components of the universe are written in mainly two different gauges. The most fundamental one is the synchronous gauge, introduced by Lifschitz in 1946, where a set of comoving observers free fall in time without changing their spatial coordinates and termed as the fundamental observers. All the cosmological simulation codes are written in this gauge. However, in this gauge the choice of the initial hypersurface is arbitrary, leading to some gauge freedom which gives birth to spurious gauge modes. Another one is the conformal Newtonian gauge, formulated by Mukhanov et al. in 1992, which is more related to the physical quantities like the gravitational potential. It is also based on a diagonal metric tensor, making the calculations a lot easier. The perturbation theory is formulated in this gauge. Apart from these two, there also exists a gauge-invariant approach of perturbation theory as suggested by Bardeen in 1980.

While studying the evolution of the constituents of the universe, we will mainly consider their density fluctuation δ and the velocity fluctuation θ. We will also consider the anisotropic stress σ and other higher moments of perturbation, where ever applicable. These equations are derived using the perturbed energy-momentum conservation equation along with perturbed Einstein's equation and Boltzmann's equation, using the FRW metric as the background met-

ric. A brief description of the evolution and fluid properties of each of the components, other than the dark energy, is provided below. We have used the method that was provided in [44].

Cold Dark Matter: The dark matter is a collisionless fluid and interacts with other matter only gravitationally. It can thus be treated as a pressureless perfect fluid, and in the synchronous gauge, it will have zero velocity fluctuation and no anisotropic stress in any of the gauges. Its evolution equations are given by

Synchronous Gauge

$$\dot{\delta}_c = \frac{1}{2}\dot{h} \tag{1.1}$$

Conformal Newtonian Gauge

$$\begin{aligned} \dot{\delta}_c &= -\theta_c + 3\dot{\phi} \\ \dot{\theta}_c &= -\frac{\dot{a}}{a}\theta_c + k^2\psi \end{aligned} \tag{1.2}$$

Here h is the metric perturbation in the synchronous gauge, and ϕ and ψ are the same in the conformal Newtonian gauge.

Photons: There are two distinct eras that characterize the evolution of photons: the Pre-recombination and the post-recombination era. In the early universe, photons and baryons(electrons) were tightly coupled by Thomson scattering and the coupled system used to behave like a single fluid. It had to face a combined effect of gravity and photon pressure which made the system to oscillate with a sound velocity dependent on the ratio of the densities of baryons and photons. Despite being tightly coupled, photons did diffuse through the system with a diffusion scale much smaller than the horizon scale. This diffusion of photons killed the density fluctuation up to a certain extent, which is well-known as the Silk Damping(SD) [45]. Due to this, the density fluctuation of photons and baryons falls of exponentially along with the oscillations, as seen in Figure 1.2. Later, when the rate of Thomson scattering became equal to the Hubble expansion rate they decoupled from each other, and the photon started traveling almost freely in the universe.

The collision between photons and electrons depends on the polarization of the photons. The perturbative variables of the photon are written in terms of the moments of its momentum-averaged angular dependent phase-space distribution function. Both the summation and differ-

ence of the two polarization states of the photon is considered. In both cases, the momentum-averaged angular dependent phase-space distribution function is expanded in terms of the Legendre polynomials. The evolution equations of photon are given by,

Synchronous Gauge

$$\begin{aligned}
\dot{\delta}_\gamma &= -\frac{4}{3}\theta_\gamma - \frac{2}{3}\dot{h} \\
\dot{\theta}_\gamma &= k^2\left(\frac{1}{4}\delta_\gamma - \sigma_\gamma\right) + an_e\sigma_T(\theta_b - \theta_\gamma) \\
\dot{F}_{\gamma 2} &= 2\sigma_\gamma = \frac{8}{15}\theta_\gamma - \frac{3}{15}kF_{\gamma 3} + \frac{4}{15}\dot{h} + \frac{8}{5}\dot{\eta} - \frac{9}{5}an_e\sigma_T\sigma_\gamma + \frac{1}{10}an_e\sigma_T(G_{\gamma 0} + G_{\gamma 2}) \\
\dot{F}_{\gamma l} &= \frac{k}{2l+1}(lF_{\gamma(l-1)} - (l+1)F_{\gamma(l+1)}) - an_e\sigma_T F_{\gamma l} \\
\dot{G}_{\gamma l} &= \frac{k}{2l+1}(lG_{\gamma(l-1)} - (l+1)G_{\gamma(l+1)}) + an_e\sigma_T\left[-G_{\gamma l} + \frac{1}{2}(F_{\gamma 2} + G_{\gamma 0} + G_{\gamma 2})\left(\delta_{l0} + \delta_{l2}/5\right)\right] \quad \text{For } l \geq 3
\end{aligned} \tag{1.3}$$

Conformal Newtonian Gauge

$$\begin{aligned}
\dot{\delta}_\gamma &= -\frac{4}{3}\theta_\gamma + 4\dot{\phi} \\
\dot{\theta}_\gamma &= k^2\left(\frac{1}{4}\delta_\gamma - \sigma_\gamma\right) + k^\psi + an_e\sigma_T(\theta_b - \theta_\gamma) \\
\dot{F}_{\gamma 2} &= 2\sigma_\gamma = \frac{8}{15}\theta_\gamma - \frac{3}{15}kF_{\gamma 3} - \frac{9}{5}an_e\sigma_T\sigma_\gamma + \frac{1}{10}an_e\sigma_T(G_{\gamma 0} + G_{\gamma 2}) \\
\dot{F}_{\gamma l} &= \frac{k}{2l+1}(lF_{\gamma(l-1)} - (l+1)F_{\gamma(l+1)}) - an_e\sigma_T F_{\gamma l} \\
\dot{G}_{\gamma l} &= \frac{k}{2l+1}(lG_{\gamma(l-1)} - (l+1)G_{\gamma(l+1)}) + an_e\sigma_T\left[-G_{\gamma l} + \frac{1}{2}(F_{\gamma 2} + G_{\gamma 0} + G_{\gamma 2})\left(\delta_{l0} + \delta_{l2}/5\right)\right] \quad \text{For } l \geq 3
\end{aligned} \tag{1.4}$$

Here the subscripts γ and b stand for photons and baryons respectively. Due to coupling through Thomson scattering, baryons and photons transfer momentum to each other which is denoted by the $an_e\sigma_T(\theta_b - \theta_\gamma$ term. In this term a is the scale factor of the universe, n_e is the electron number density, and σ_T is the Thomson scattering cross-section. The momentum-averaged angular dependent part of the phase-space distribution functions of the sum and difference of the two photon polarization states are denoted by F_γ and G_γ, respectively.

Baryons: The baryons can be considered to be non-relativistic after the neutrino decoupling and all the higher moments of perturbation including the anisotropic stress σ can be neglected. Nevertheless, they are tightly coupled to the photons until the recombination and

the momentum transfer between them do take place. The evolution equation of the baryons are given by

Synchronous Gauge

$$\begin{aligned} \dot{\delta}_b &= -\theta_b - \frac{1}{2}\dot{h} \\ \dot{\theta}_b &= -\frac{\dot{a}}{a}\theta_b + c_s^2 k^2 \delta_b - \frac{4\rho_\gamma}{3\rho_b} a n_e \sigma_T (\theta_b - \theta_\gamma) \end{aligned} \tag{1.5}$$

Conformal Newtonian Gauge

$$\begin{aligned} \dot{\delta}_b &= -\theta_b + 3\dot{\phi} \\ \dot{\theta}_b &= -\frac{\dot{a}}{a}\theta_b + c_s^2 k^2 \delta_b + k^2\psi - \frac{4\rho_\gamma}{3\rho_b} a n_e \sigma_T (\theta_b - \theta_\gamma) \end{aligned} \tag{1.6}$$

Here ρ_γ and ρ_b are the background densities of photons and baryons respectively and c_s^2 is the speed of sound in the medium.

Massless Neutrino: Massless neutrinos behave as photons apart from the fact that they do not participate in any polarization dependent collision. The momentum-averaged angular dependent part of the phase space distribution function of the massless neutrinos, F_ν, can be expanded in Legendre polynomials as the photons. The energy-momentum relation for massless neutrino depends only on its momentum, allowing some of the perturbation variables to be related to the multipole moments of the phase space distribution function through simple algebraic relations. The evolution equations can be written as follows.

Synchronous Gauge

$$\begin{aligned} \dot{\delta}_\nu &= -\frac{4}{3}\theta_\nu - \frac{2}{3}\dot{h} \\ \dot{\theta}_\nu &= k^2\left(\frac{1}{4}\delta_\nu - \sigma_\nu\right) \\ \dot{F}_{\nu 2} &= 2\sigma_\nu = \frac{8}{15}\theta_\nu - \frac{3}{15}kF_{\nu 3} + \frac{4}{15}\dot{h} + \frac{8}{5}\dot{\eta} \\ \dot{F}_{\nu l} &= \frac{k}{2l+1}(lF_{\nu(l-1)} - (l+1)F_{\nu(l+1)}) \quad \text{For } l \geq 3 \end{aligned} \tag{1.7}$$

Conformal Newtonian Gauge

$$\begin{aligned} \dot{\delta}_\nu &= -\frac{4}{3}\theta_\nu + 4\dot{\phi} \\ \dot{\theta}_\nu &= k^2\left(\frac{1}{4}\delta_\nu - \sigma_\nu\right) + k^2\psi \\ \dot{F}_{\nu l} &= \frac{k}{2l+1}(lF_{\nu(l-1)} - (l+1)F_{\nu(l+1)}) \quad \text{For } l \geq 2 \end{aligned} \tag{1.8}$$

Massive Neutrino: Massive neutrinos are also collisionless particles as massless neutrinos. However, their energy-momentum relation depends on both their momentum and mass, which makes it impossible to integrate out the momentum dependent part. And thus making it impossible to connect the perturbation variables to the moments of the momentum averaged phase space distribution function through simple algebraic relations. Nevertheless, the same procedure for deriving the evolution equations of perturbations can be used for massive neutrino, using their total phase space distribution function Ψ this time. The equations are given by

Synchronous Gauge

$$\begin{aligned}
\dot{\Psi}_0 &= -\frac{qk}{\epsilon}\Psi_1 + \frac{1}{6}\dot{h}\frac{d\ln f_0}{d\ln q} \\
\dot{\Psi}_1 &= \frac{qk}{3\epsilon}(\Psi_0 - 2\Psi_2) \\
\dot{\Psi}_2 &= \frac{qk}{5\epsilon}(2\Psi_1 - 3\Psi_3) - \left(\frac{1}{15}\dot{h} + \frac{2}{5}\dot{\eta}\right)\frac{d\ln f_0}{d\ln q} \\
\dot{\Psi}_l &= \frac{qk}{(2l+1)\epsilon}(l\Psi_{(l-1)} - (l+1)\Psi_{(l+1)}) \quad \text{For } l \geq 3
\end{aligned} \tag{1.9}$$

Synchronous Gauge

$$\begin{aligned}
\dot{\Psi}_0 &= -\frac{qk}{\epsilon}\Psi_1 - \dot{\phi}\frac{d\ln f_0}{d\ln q} \\
\dot{\Psi}_1 &= \frac{qk}{3\epsilon}(\Psi_0 - 2\Psi_2) - \frac{\epsilon k}{3q}\psi\frac{d\ln f_0}{d\ln q} \\
\dot{\Psi}_2 &= \frac{qk}{5\epsilon}(2\Psi_1 - 3\Psi_3) - \left(\frac{1}{15}\dot{h} + \frac{2}{5}\dot{\eta}\right)\frac{d\ln f_0}{d\ln q} \\
\dot{\Psi}_l &= \frac{qk}{(2l+1)\epsilon}(l\Psi_{(l-1)} - (l+1)\Psi_{(l+1)}) \quad \text{For } l \geq 2
\end{aligned} \tag{1.10}$$

Here $\epsilon = \sqrt{(q^2 + m_\nu^2 a^2)}$ and f_0 are the zeroth-order phase space distribution function, which is a Fermi-Dirac distribution function for massive neutrino.

In the Figure 1.2 we have shown the transfer functions of the density fluctuation of different components of the universe including the dark matter, the baryon, the photon and the massive neutrino. These plots are generated using adiabatic initial conditions and initial power spectrum with scalar spectral index $n_s = 0.9615$. As evident from all of these plots, every element

behaves the same way in super-horizon scales, i.e., scales that have not entered the horizon yet, apart from a difference in normalization because of their different initial conditions. When a certain scale enters the horizon, i.e., in the sub-horizon regime, their transfer functions starts showing a difference.

The dark matter, being a collisionless fluid, has no interesting feature in the sub-horizon regime. They only interact in gravitational means, and thus their evolution is controlled by the background densities of the elements of the universe. When the universe is radiation dominated dark matter perturbation grows logarithmically and after the MRE it grows linearly. Therefore, the only interesting feature of the dark matter transfer function is a turnover denoting the MRE.

On the other hand, the transfer functions of baryons and photons show interesting features. The plot at the top-left panel of Figure 1.2 contains the transfer function at $z = 2000$ when baryons and photons were tightly coupled to each other. As seen from this figure, the transfer functions of baryons and photons are very similar to each other, and the photon-baryon fluid has much less density fluctuation at smaller scales due to SD. In the top-right panel, we showed the same plot but taken at $z = 100$. Decoupling of photons and baryons happened at $z \simeq 1100$, and after that, photons traveled almost freely inside the universe. Thus at $z = 100$, the density fluctuation of the photon is severely cut down at scales below the horizon. However, the baryonic transfer function has somewhat caught up with that of the dark matter. This feature becomes more visible at $z = 0$(bottom left panel of Figure 1.2), when the baryons exactly trace the dark matter. Hence we make the following conclusion, after the decoupling, the baryons start falling into the potential wells previously created by the dark matter, initiating the structure formation. If there were no dark matter, there would not be enough power in baryons to form structures on their own, as seen from the plot at the top-left panel of Figure 1.2. Hence, the fact that the dark matter is the key driving force to structure formation is established, and we will show in the next two paragraphs that it must be cold in nature to execute the structure formation successfully. The standard model of cosmology is comprised of cold dark matter(CDM) with a cosmological constant Λ. In the bottom-right panel of Figure 1.2, we plot the Sloan Digital Sky Survey(SDSS) DR11 CMASS monopole power spectrum [46] with the theoretical prediction of power spectrum by ΛCDM model. These plots agree with each other quite well at large scales.

Another component of the universe worth discussing is the massive neutrino. Massive

neutrinos with mass O(10 eV) were considered to be the dominant dark matter candidate of the universe in the early ages of cosmology. In the next paragraph, we provide a brief history of massive neutrino as a dark matter candidate followed by another paragraph where we discuss its cosmological implications.

The first paper that considered the role of neutrino and its mass in cosmology was by Gershtein and Zeldovich in 1966 [47]. In this pioneering work, they considered how the electron and muon neutrino could affect the expansion of the universe and their present number densities. By comparing the expansion rate of the universe with the available Hubble expansion rate, they found that each of these two neutrinos should have a mass, not more than 400 eV. They also concluded that heavier species could slow down the expansion rate or can even reverse the direction of it. However, this work was focused only on studying the effects of neutrinos in the expansion of the universe, and there was no mention of the fact that the neutrinos can account for the "missing mass" of the universe, prevalent in the galaxy clusters. Cowsik and McClelland in 1972 [48], again to constrain the expansion of the universe improved the upper limit on the mass of a Dirac neutrino species to 8 eV. Many other works followed to constrain the neutrino mass, but none of them considered the possibility of neutrinos to be a potential candidate to count for the missing mass. In 1976, Szalay and Marx [49] first examined the issue of missing mass and showed that a neutrino(electron or muon) with mass ≈ 13.5 eV could make up the missing mass of the universe successfully. This work was followed by a Gunn et. al in 1977 [50] which also advocated for a heavy stable lepton to be an excellent candidate for creating the galactic halo and binding the galaxies in the clusters, and reinforced by further works of Zeldovich and his group in 1980. Further interest on neutrino was created by the tritium beta decays experiment performed at the same time that measured the mass of electron anti-neutrino(and neutrino) to be 30 eV. This discovery though got refuted later, inspired the community to explore the cosmological signatures of the massive neutrinos.

By the middle of 1980, numerical simulations started showing up, giving an opportunity to study the effects of the massive neutrino in structure formation as dark matter and thus to distinguish between hot(relativistic) and cold(non-relativistic) dark matter. The terminologies of hot, cold and warm dark matters were first used in [51]. Standard model neutrinos are very light and have a very high free-streaming velocity. This leads to power suppression at scales below the free-streaming scale, as seen from Figure 1.2. A neutrino with mass O(10 eV)

has a free streaming scale of $l_\nu \approx 41(1+z)^{-1}\left(\frac{m_\nu}{30\,\mathrm{eV}}\right)^{-1}$ Mpc, which is as large as the size of a supercluster that enters the horizon long after the neutrino has become non-relativistic. Because of its higher free-streaming velocity, they used to be called as the hot dark matter(HDM). Hence, in an HDM dominated universe, larger structures form before, and smaller structures form by fragmentation of larger structures at later times. This top-down approach implies that the structure formation has started after the collapse of supercluster earliest at $z \sim 2$, where many quasars are observed at $z \gtrsim 3$. The first simulation of the universe taking HDM as dominating dark matter candidate by White et al. in 1983 [52]. They indeed found that the neutrino clustering scale is much higher than the observed galaxy clustering scale and an agreement can only be possible if the scalar spectral index n_s is > 3. Thus, it is evident that the HDM cannot make a significant portion of dark matter and dark matter has to be cold in order to make the observed structure formation possible. In 1993, Dodelson and Widrow suggested a production mechanism of an additional neutrino species with mass O(1 keV) that can count for the dark matter abundance of the universe. We will come back to this issue in Section 1.7

1.2.2 CMB Anisotropy

The CMB radiation was accidentally discovered by Arno Penzias and Robert Woodrow Wilson in 1964 as they were doing experiments using the Holmdel Horn Antenna intended for satellite communication. This great discovery was awarded the Nobel Prize in 1978. The basic concept of creation of the CMB is as follows. In the early universe, the baryons and the photons were tightly coupled to each other through Thomson scattering and used to behave like a single fluid. After almost 400 thousands of years of the big bang, the rate of Thomson scattering became less than the Hubble expansion rate, making the photon and baryon decouple. After the decoupling, photons started moving almost freely in the universe and gave rise to an afterglow of the early universe. The radiation is seen in the microwave band at present and is very uniform over the entire sky with a temperature of 2.7260 ± 0.0013 K [53]. However, the radiation does contain anisotropy of the order of 10^{-5} [54], which carries information about the universe when it was just 400 thousands year old. The map of CMB anisotropy, shown below in Figure 1.3, is the earliest possible picture of the universe.

The temperature field of photons in the universe can be written as $T(\vec{x}, \hat{p}, \eta) = T(\eta)[1 + \Theta(\vec{x}, \hat{p}, \eta)]$, where Θ denotes the fluctuation in the photon temperature. This quantity can be

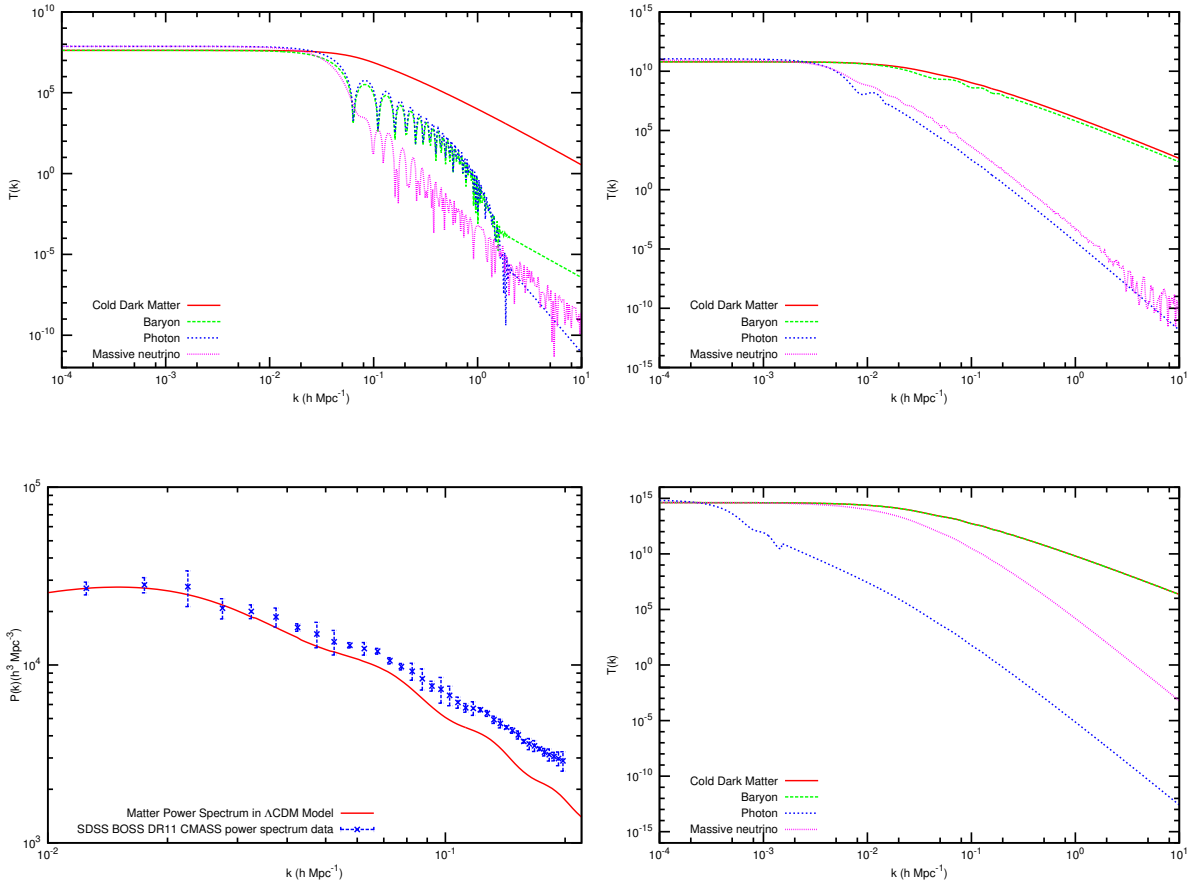

Figure 1.2: Clockwise from left :The transfer functions of different components of the universe at $z = 2000$, $z = 100$ and $z = 0$. The Bottom left panel shows the comparison of ΛCDM matter power spectrum with the SDSS BOSS DR11 CMASS power spectrum data. The components considered are the cold dark matter(red solid lines), the baryon(green long-dashed lines), the photon(blue short-dashed lines) and the massless neutrino(pink dotted lines).

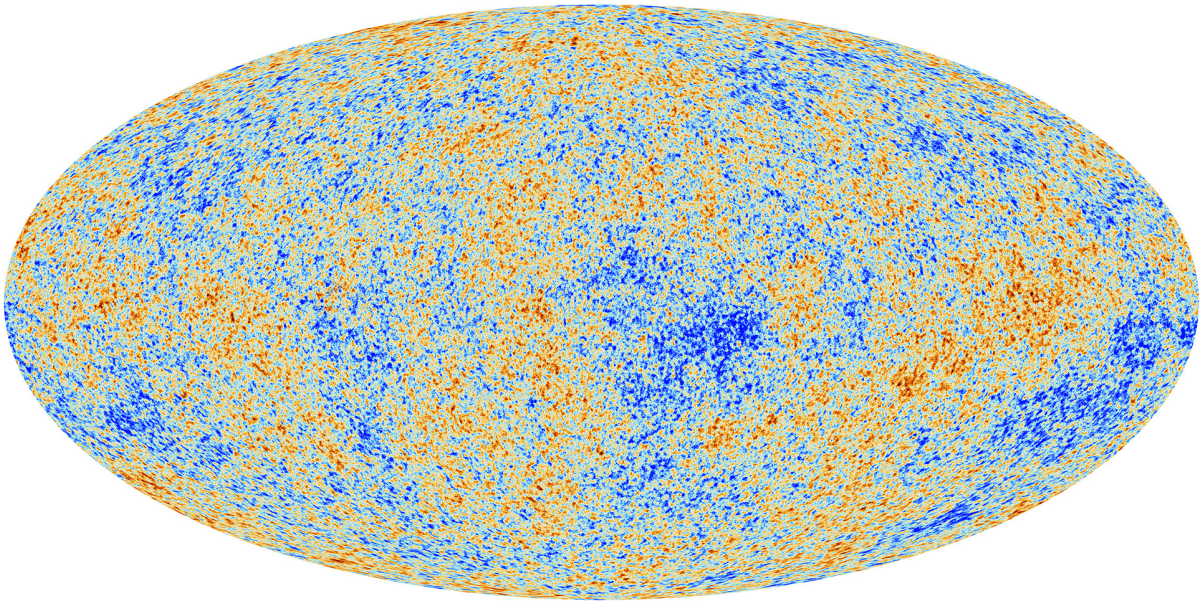

Figure 1.3: The CMB anisotropy map as seen by the Planck satellite. The picture is taken from `http://www.esa.int/`

expanded in terms of the spherical harmonics as

$$\Theta(\vec{x},\, \hat{p},\, \eta) = \sum_{l=1}^{\infty} \sum_{m=1}^{\infty} a_{lm}(\vec{x},\, \eta) Y_{lm}(\hat{p}) \tag{1.11}$$

It's the variance of a_{lm} given by $\langle a_{lm} a^*_{l'm'} \rangle = \delta_{ll'}\delta_{mm'}C_l$ that is measured as a function of l with proper normalization.

The power spectra of the CMB anisotropy, $l(l+1)C_l/(2\pi)(\mu K^2)$, are plotted in Figure 1.4 for different abundances of the constituents of the universe. The plots feature a series of damped peaks and deeps, preceded by a valley-like region. The precise nature of the power spectrum depends on various cosmological parameters, and there do exist degeneracy among these parameters. Nevertheless, measuring locations and heights of all the peaks can yield an accurate estimation of all the parameters. As this section is written to motivate the need for dark matter in cosmology, we will consider only the effects of dark matter and baryon on the CMB power spectrum. As we show below, the dark matter can have noticeable impacts on the CMB power spectrum.

1) Effects of changing $\Omega_{\rm dm}$ with a fixed Ω_b on CMB power spectrum:

In the left panel of Figure 1.4, we have shown a plot of CMB power spectrum for different values of $\Omega_{\rm dm}$ and a fixed Ω_b. We have considered both scenarios with less(more) dark matter density than its best fit value, including one with no dark matter at all. Changing the total matter density implies that the MRE will be earlier(later) for models with a more(less) dark matter abundance. The first effect that we can notice is that the first peak has shifted towards higher(lower) l for a smaller(larger) amount of dark matter. The second effect is the overall enhancement(suppression) of fluctuation at the peaks for lower(higher) dark matter density. If the universe is dominated by radiation for a longer time due to lower matter density, the potential decays because of the inability of radiation to cluster. This provides a strong driving force for oscillation and subsequently the peak height increases if dark matter density is decreased. It is the highest and an order of magnitude higher for the case when there is no dark matter at all. Another way dark matter affects the CMB spectrum is by modifying the Sachs-Wolfe(SW) plateau in the low l region. SW effect is the loss of energy of photons while climbing out the gravitational potentials at the Last Scattering Surface. If the matter density is high(low), photons will have to work harder(lesser) to get out of the gravitational wells and thus will lead to a depressed(an enhanced) SW plateau. Also, the second peak is absent when there is no dark matter at all.

2) Effects of changing Ω_b with a fixed $\Omega_{\rm dm}$ on CMB power spectrum:

In the middle panel of the Figure 1.4, we have plotted CMB power spectra for different baryon density keeping the dark matter density fixed. The first thing to note is the enhancement(suppression) of fluctuation in the odd peaks due to the lower(higher) frequency of oscillation in the presence of heavy(light) baryon. This is a unique effect of changing the baryon abundance. The peaks are also shifted accordingly because of changed sound horizon. The second effect is that the diffusion is decreased(increased) if the baryon density is increased(decreased) so that the fluctuation is higher(lower) for $l > 1000$) and the diffusion damping moves to smaller(larger) angular scale.

Thus the location and amplitude of the first peak along with the presence of the second peak undoubtedly confirm the existence of dark matter. In the right panel of Figure 1.4, we plot the CMB power spectrum data provided by Planck 2015 [55] with the one predicted by the standard ΛCDM model. The agreement with the data is remarkable implying that the

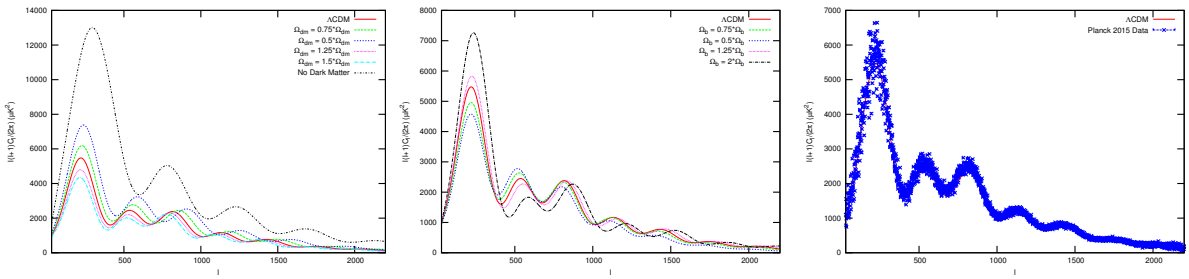

Figure 1.4: The CMB power spectrum as a function of the multipole l. The Left panel contains spectra for different values of $\Omega_{\rm dm}$ while the middle panel is for models with different Ω_b. The right panel contains the plot of Planck 2015 CMB power spectrum data, compared with the computed one using ΛCDM model.

dark matter is the dominating matter candidate, comprising of $\sim 85\%$ of all the matter in the universe.

The alternative theories of dark matter, i.e., the Modified Newtonian Dynamics(MOND) [56, 57] that was used to explain the galaxy rotation curve, can't provide any explanation for any of these cosmological signatures of dark matter.

1.3 Dark Matter Candidates

According to their particle nature, dark matter can be broadly classified into two types: Baryonic and Non-baryonic.

1.3.1 Baryonic Candidates

The baryonic dark matter candidates, as suggested in the older literature, consist of faint stars and remnants which are more popularly known as the Massive Compact Halo Objects(MACHOs)(Please refer to [58] for a review). Some other baryonic dark matter candidates can be the cold gas clouds in galaxies [59, 60], the Warm-Hot Intergalactic Medium(Hereafter IGM) and so on. The most explored baryonic dark matter candidate is the MACHO. They consist of faint compact objects with mass $\sim 10^{-3} M_\odot$, brown dwarf stars with mass $\sim 0.08 M_\odot$ or remnants of the first stars. The conventional way to detect these MACHOs is through gravitational microlensing. This is a powerful tool to detect an object in the mass range of

$10^3 M_\odot > M > 10^{-6} M_\odot$, which is just the theoretically allowed range of the mass of MACHOs. Quite a few of collaborations made an effort to detect them in the galactic bulge of the MW [61] and both of the Magellanic Clouds(MC) [62, 63] using microlensing. A very brief description of detection of a microlensing event is provided below.

If any small object comes in the way of the observer and a bright object the trajectory of the light coming from the source gets distorted due to the presence of the gravitational field of the compact object(the lens). This distortion can give rise to multiple images. The angular separation between the images is dependent on the mass of the lens and the distances to the lens and the source. For a lens with mass $1M_\odot$, the separation can be of the order of a few arcseconds. If the separation is too low to be resolved by the telescope being used, the amplification of the luminosity occurred due to the presence of the image is measured and used to calculate the lens mass. By monitoring the slight variation in the luminosity of the sources, a microlensing event can be detected and utilized to calculate the mass of the lens (here the MACHOs). Recently, this technique is getting popular to detect planets in stellar systems that are far from us.

The probability of observing a microlensing event in a distant galaxy is tiny. However, if millions of stars are observed for years, a significant amount of microlensing events can be recorded. The MACHO collaboration did a microlensing survey of Large Magellanic Cloud(LMC) covering 11.7 million stars during 5.7 years and found $13 - 17$ confirmed microlensing events [61], concluding that the MACHOs contain around 20% of the halo mass of LMC at 95% Confidence level(CL). They also found that the most likely mass of MACHOs can lie between $0.15M_\odot$ and $0.9M_\odot$. However, in more recent times, the EROS-2 Survey [63] of both the MCs found only one microlensing event after 6.7 years of observations of 33 million stars. This implies that just 8% halo mass fraction occupied by MACHOs. Also, MACHOs with mass range $0.6 \times 10^{-7} M_\odot < M < 15 M_\odot$ were ruled out as a primary occupant of the Galactic halo.

We have shown the density fluctuations of different components of the universe before and after decoupling previously in Figure 1.2. The density fluctuations of baryons and photons are same before decoupling as they are tightly coupled to each other. After the decoupling has taken place at, density fluctuation of photon dies out very fast, and the baryons fall into the potentials created by the CDM. It is clear that in the absence of non-baryonic CDM there is not enough power to initiate the structure formation by the baryons alone. Hence, if dark

matter were baryonic, we would not be able to observe the present-day structures. Therefore, the dark matter, whatever it is, cannot be baryonic in nature. Moreover, the abundance of MACHOs discussed in the last paragraph is also discouraging to consider the majority of the dark matter to be baryonic in nature.

1.3.2 Non-baryonic Candidates

In literature, lots of non-baryonic dark matter candidates have been proposed and explored. As argued in Section 1.2, the dark matter has to be cold in nature to form the observed structures. The most studied class of non-baryonic CDM candidates is the Weakly Interacting Massive Particle. No known particles in the standard model of particle physics meet the criteria to be a WIMP candidate while the supersymmetric(SUSY) extension does accommodate a handful of potential WIMP candidates. The emergence of this candidate is inspired by the well-known WIMP miracle which is in fact shown to be possible in the SUSY extension of the standard model of particle physics. Let us suppose that along with all the standard model particles, a massive particle χ with mass m_χ was in thermal equilibrium when the temperature of the universe was very high ($T \gg m_\chi$) and used to convert to lighter particles very fast. When the temperature of the universe falls below m_χ, the particle came out of equilibrium. The rate of the conversion to lighter particles became less than the Hubble expansion rate of the universe, and a relic density of χ was set. In Figure 1.5 the number density of χ is shown as a function of m_χ/T.

An approximate value of this relic density, after solving the Boltzmann equation of the evolution of this particle is given by [64]

$$\Omega_\chi h^2 \simeq \frac{m_\chi n_\chi}{\rho_c} \approx \left(\frac{3 \times 10^{-2t}\,\mathrm{cm}^3\,\mathrm{s}^{-1}}{\langle \sigma_A v \rangle} \right) \tag{1.12}$$

where σ_A is the annihilation cross-section of χ to lighter particles and v is its velocity. The electroweak cross-section for a particle is given by $\sigma_{\mathrm{ew}} = \alpha^2/m_{\mathrm{ew}}^2$ and the value of σ_{ew} is $\approx 10^{-9}\,\mathrm{GeV}^{-2}$ for $\alpha \sim \mathrm{O}(0.01)$ and $m_{\mathrm{ew}} \sim \mathrm{O}(100\ \mathrm{GeV})$. A particle with this self-annihilation cross-section and mass and also a freeze-out velocity v, which is a significant fraction of the speed of light, produces the correct cosmological relic density of CDM according to Equation 5.2. As the evolution of the universe has no apparent connection to electroweak interaction theory, this came to be a miraculous discovery and thus termed as the WIMP miracle. This discovery

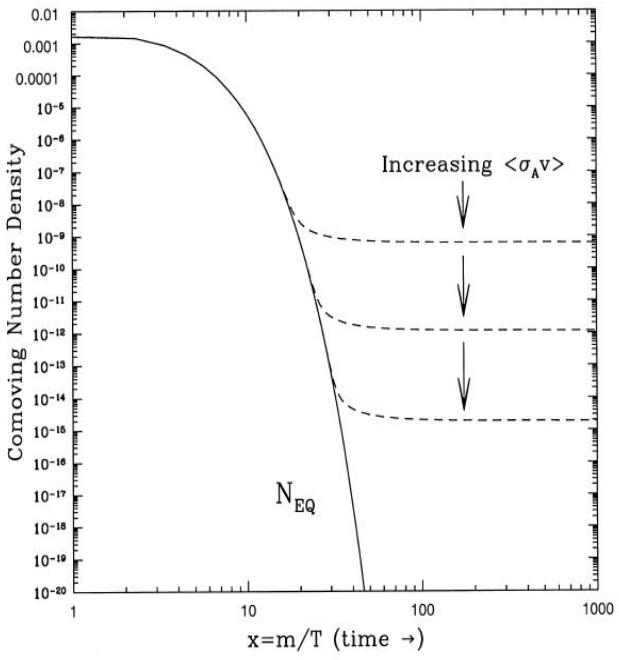

Figure 1.5: Comoving number density of WIMP in the early universe as a function of m_χ/T. The dashed curves are actual abundances depending on various $\langle \sigma_A v \rangle$ and the solid one is the equilibrium number density. The picture is taken from [64].

led to many experiments to detect the WIMP with mass O(100 GeV). The WIMP interacts only gravitationally and at most, weakly. To be a dark matter candidate, it has to be charge neutral too. Due to their very high mass, they are very slowly moving particles, thus satisfies the "cold" criterion. Because of their weakly interacting nature, they are hard to detect, even the flux of these particles on Earth is very high.

The SUSY extension of the standard model can also give rise to light CDM such as Weakly Interaction Sub-eV particle(WISP) that can couple to the photon field. Some examples are the Axion-like Particles, Pseudoscalar Axion or a hidden photon, that can couple to the "visible photon". (Please refer to [65] for an excellent review of WISPs). Other non-baryonic dark matter candidates are Neutrinos, Axions, Mirror Matter [66], Quark Nuggets [67], WIMPzillas [68] and so on. In some models, dark energy can also behave like dark matter depending on its equation of state, formally known as the Chaplygin gas [69].

1.4 Detection of Non-baryonic Dark Matter

Depending on the detection technique, there are 3 different types of dark matter search: Direct, Indirect and Collider.

1.4.1 Direct Detection

The main principle of direct dark matter search is to make the dark matter particle, coming from the MW halo, to hit the material of the detector, which is usually set underground to avoid cosmic rays and radioactive decays of the rocks. One of the most notable examples of such underground detector is The Large Underground Xenon experiment (LUX). The collision of dark matter with the detector material can deposit energy as phonons in cryogenic detectors. It can also create scintillation or ionize the detector medium. The localized scattering volume defined by the scattering event is shielded by the detector material which can be semiconductor crystals [70, 71] or liquid neutral gas [72, 73]. The direct detection rate depends on the local dark matter density and velocity distribution. The quantity that is measured is the collision cross-section, either depending on the spin of the target nucleus or not.

For spin-independent cross-section, three direct detection experiments have claimed to find out signals created by the dark matter-nucleon collision. The DAMA/LIBRA detector at

Gran Sasso finds an annual modulation of singe-hit events in the 2-6 keV energy interval with amplitude (0.0112 ± 0.0012) counts/kg/keV/day in the 9.3σ CL. This detection cost 14 annual cycles and a total exposure of 1.33 ton years. All of these results are in good agreement with those expected for dark-matter particles [74]. The CoGent detector in Soudan Underground Laboratory demands to detect a 2σ dark-matter excess and annual modulation [71]. Along with these two, the CDMS-II at SNOLAB observes three low-energy events in their Silicon detector data sample, whose origin was not clearly understood. After upgrading the detector, the new CRESST-II experiment no longer finds any excess signal that was previously claimed by the first version of the detector [75]. All other direct detection searches have set exclusion limits on the SI dark matter-nucleus cross section which contradict the claims mentioned above. They are shown in Figure 1.6 as full lines. The signal claims also seem to be in conflict with the first PANDA-X results [76].

Spin-dependent cross sections are smaller than spin-independent cross sections by a factor A_N^2, the atomic number of the target nucleus. Currently, the best upper limits from XENON100 [77] for protons and neutrons as targets are shown in Figure 1.7. For comparison, SD cross-section measurements performed by other experiments are also displayed.

1.4.2 Collider Detection

As the dark matter is non-baryonic in nature and its interaction cross-section with the detector material is minuscule, it is challenging to detect them directly, like the neutrinos. On the other hand, if they are produced in a collider, it can create a missing energy signal. In LHC or similar colliders, the missing energy can be observed only in the transverse direction and determined by studying the recoiling objects such as jets, heavy quarks, photons, and leptons. Monte Carlo simulations are performed considering both the missing energy signal and the background, using a dark-matter particle with certain properties and its interactions with standard model particles. The standard model backgrounds can be largely eliminated by defining a specific kinematic cut off in the energy, and thus the model expectations with experimental data can be confronted. An excess of the kinematic distributions may then be attributed to the dark matter particle that is being looked for. A notable example is a search for the lightest supersymmetric particle (LSP), in the pair production and subsequent cascade decay of squarks and gluinos to jets and two LSPs.

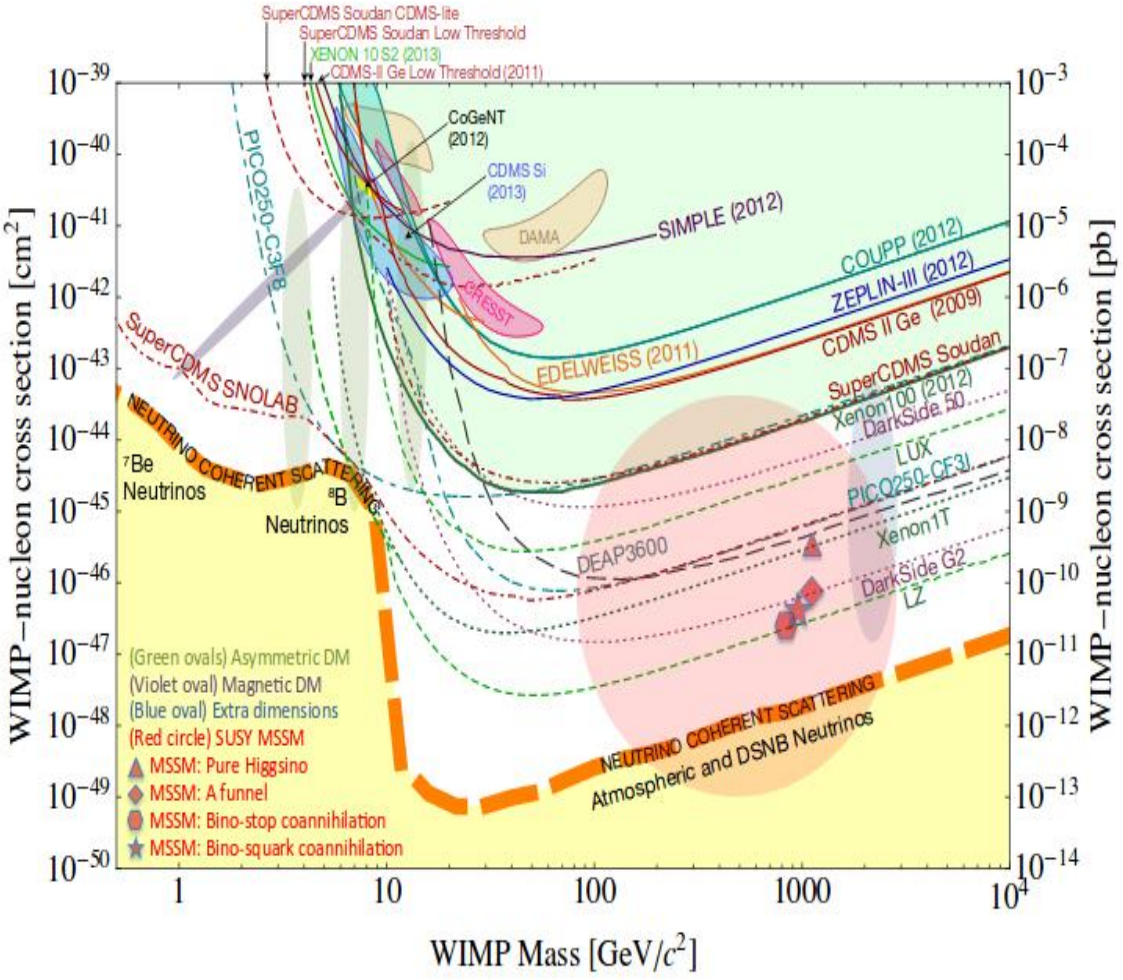

Figure 1.6: A compilation of direct dark matter detection results for spin-independent WIMP-nucleon scattering for high mass WIMPs. The figure is taken from [78].

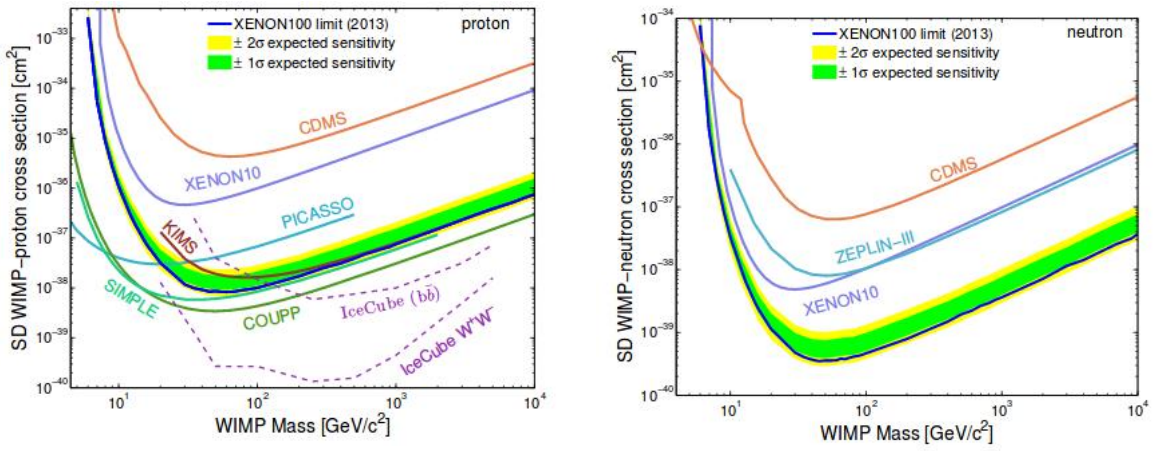

Figure 1.7: Direct dark matter detection results for spin-dependent WIMP-nucleon scattering with protons(Left) and neutrons(Right). Both of these figures are taken from [79].

1.4.3 Indirect Detection

Along with directly colliding with nucleons of the detector material, dark matter can also reveal its existence indirectly. Though the total number of dark matter particles does not change significantly after freeze-out in the early universe, their spatial distribution does change substantially during the structure formation creating density peaks in certain parts of the universe. The very self-annihilation that plays a central role in the freeze-out of dark matter can give rise to a significant flux of γ-rays, neutrinos, and even antimatter, especially in regions where the dark matter density is high. The energy of the secondary particles can be comparable to the mass of the dark matter itself which is typically a few hundred GeV. Since dark-matter annihilation scales with the square of its density, indirect detection is more sensitive to cosmological and astrophysical processes than the direct detection, along with the distribution of dark matter in galaxy and galaxy clusters. Some notable indirect dark matter experiments are PAMELA [80], VERITAS [81] and SPI/INTEGRAL [82].

1.5 The Troubles with WIMP: Looking for a new dark matter candidate

The WIMP describes the large-scale structure of the universe reasonably well. However, when it comes to the scales comparable to galaxies and groups of galaxies, it fails to explain some of the observational facts, giving rise to some well-known problems in cosmology. The first one of them is the cusp-core problem in dwarf and low surface brightness(LSB) galaxies [83]. This issue is about the discrepancy between theoretically simulated [84] increasing dark matter halo profile (cusp) towards the center of the galaxy while observationally flatter density profiles are found. Another issue with the WIMP is the missing satellite problem [85, 86]; N-body simulations of structure formation with CDM produce much more satellite halos of an MW type galaxy than observed. One more small-scale problem of WIMP is the "too big to fail." problem [87, 88], which is found out more recently. This issue underlines the fact that, based on N-body simulations, a majority of the most massive subhalos of the MW are too dense to host any of its bright satellites. The problems are discussed in more detail in the following subsections.

1.5.1 The Cuspy Halo Problem

The universe, at different scales, has been using several N-body simulations in the standard CDM cosmology. One of the most significant results is the computation of the density profile of dark matter in galaxies. The density profile is computed in both the outer and inner regions of the halo hosting the galaxy. The first simulation, performed in 1995 [89], has shown that the density profiles of the dark matter halos follow a power-law profile with slope $\alpha_s = -1$. Due to poor numerical resolution, the inner part of the halos could not be simulated appropriately, and thus the nature of slope in the central part of the halo was not properly estimated.

Later, Navarro et al. in 1995 [84] performed a more detailed N-body simulation with CDM using different sets of cosmological parameters. They found that regardless the cosmological parameters, as well as the mass and size of the halos, the inner part of the halo, can be described by a power-law density profile with slope $\alpha = -1$. For outer regions of the halo, the slope changes to $\alpha = -3$. The obtained density profile is described by the well-known global

NFW density profile

$$\rho_{NFW}(r) = \frac{\rho_i}{(r/R_s)(1+r/R_s)^2} \tag{1.13}$$

where ρ_i is related to the density of the universe at the time when the collapse took place. The radius R_s represents the characteristic radius of the halo. The observational quantity, i.e., the rotation curve is given by

$$V(r) = V_{200}\sqrt{\frac{\ln(1+cx) - cx/(1+cx)}{x[\ln(1+c) - c/(1+c)]}} \tag{1.14}$$

with $x = r/R_{200}$. Here R_{200} is the radius where the density fluctuation becomes equal to 200 times the critical density of the universe. This is also roughly the virial radius of the halo. $c = R_s/R_{200}$ is the concentration parameter and V_{200} is the velocity at R_{200}. These two parameters are tightly constrained by cosmology, with a small scatter, as follows [90]

$$\log c = 1.191 - 0.064 \log V_{200} - 0.032(\log V_{200})^2 \tag{1.15}$$

Later, [91] also found support for the NFW profile but with steeper inner slope with $\alpha = -1.5$ and same outer slope of $\alpha = -3$. With the advancement of technology more sophisticated simulations were performed by different groups [92, 93], to mention a few). Despite their different analytic and numerical techniques they all tend to provide the slope $\alpha \lesssim -1$ in the inner region of the halo, i.e., at one kpc from the center of the halo. Some simulations have been successful [94] to probe deeper into the halo, yielding shallower profile with $\alpha \simeq -0.8$ at 0.1 kpc from the center. This implies that up to this radius the halo profile can be safely represented by the NFW profile.

When it comes to real observations, the data is found to be in tension with the theoretical predictions. The initial observations of dark matter dominated dwarf galaxies were performed by different groups [95, 96]. As these galaxies are dark matter dominated they were expected to provide ideal laboratories to test the NFW profile of halo. The authors found that the inner density profile is considerably flatter than that was predicted by the NFW density profile and the density profile can be represented by the Pseudo Isothermal(PI) profile given by

$$\rho_{PI}(r) = \frac{\rho_0}{1+(r/R_c)^2} \tag{1.16}$$

With ρ_0 to be the central density and R_c the core radius of the halo. The velocity profile is asymptotic for this case and is given by

$$V_{asy} = \sqrt{4\pi G\rho_0 R_c^2[1 - (R_c/R)\arctan(R/R_c)]} \tag{1.17}$$

In [95] this disagreement was attributed to the resolution and projections effects of the data, as well as the consequences of pressure support. However, the conclusion of this work was that those effects are not influential enough to change the result abruptly. HI observations of gas-rich and dark matter dominated LSB galaxies were first performed by Zwann et al. in 1995 [97]. Though the resolution of the observation was poor, the derived density profile was similar to that of the late-time dwarf galaxies as observed by [98]: slowly rising density followed by an almost flat profile. Due to low resolution, these results were not compared with the theoretical predictions, but this attempt was taken by [99] with higher resolution data. The comparison showed that the NFW profile provides a too steep rise of the inner density profile, provided that the well-constrained $c - V_{200}$ relation be followed. The so-called "beam-smearing" effect was suspected to be a reason for this discrepancy [98]. However, it was argued in [100] that, though the "Beam smearing" does distort the information about the density profile up to some extent, it is not strong enough to disguise the cuspy profile to a cored profile. Later, many other studies [101, 102] were performed with larger samples of LSB galaxies and a better modeling of the systematics and "Beam smearing". It was found that the HI data of most of the LSB galaxies are consistent with both cored and cuspy haloes. In fact, one of the galaxies in their samples, the NGC247, found to be containing a cuspy halo.

The results of the HI observations were further compared with the Hα observations which have an order of magnitude better resolution than that of HI . The first Hα observation of long-slit rotation curves of the LSB galaxies by Swaters et al. [103] indicated that the density profile obtained by Hα observation is steeper than that achieved by HI observation. Interestingly, for one of the galaxies in the sample, it was found that the density profile is rising very steeply and somewhat agreeing with the NFW profile. However, when the beam smearing effect was taken into account, the HI and Hα observations turn out to agree with each other. A larger sample study with a better resolution by [104, 105] revealed the presence of the beam smearing effect in most of the galaxies, but again not strong enough to alter the result substantially as also found by [90]. These Hα rotation curves thus establish the fact that the cored profiles are not originating from resolution effects and there exists a discrepancy between the theoretical

predictions and observed facts.

1.5.2 The Missing Satellite Problem

The hierarchical structure formation theory states that the smaller size halos should collapse earlier than the larger halos when the universe had a higher density. So, it is possible that some of the satellite haloes formed before the formation of the main MW halo. Some of these satellite haloes, containing galaxies, got accreted into the MW or the local group during the formation of the MW galaxy. The accretion is not 100% efficient as satellites are indeed observed.

The significant discrepancy between the number of satellites of an MW type galaxy estimated using simulations, and the number of satellites found observationally is called the missing satellite problem. In 1993, Kauffmann et al. [106] performed a semi-analytic calculation to get the abundance of satellite halos around an MW like halo, using hierarchical structure formation theory in the presence of CDM. Using the efficiency of dynamical friction as a free parameter, they found that the calculation produces far too many satellites than observed. They argued for increasing the effectiveness of dynamical friction to account for the destruction of halos. However, it was found that this can eventually destroy a significant fraction of the satellites, making it impossible for the MC-like satellites to survive.

In 1995 Klypin et al. [85] performed an N-body simulation to calculate the number of surviving satellites in an MW size halo. Using high-end cosmological simulations, they calculated the VDF, defined as the number of satellites in a certain circular velocity($V_{\rm circ}$) interval, and compared them with the then available data for the Local group.

The VDF was found to be a power law function of $V_{\rm circ}$, approximately. The number of satellites and VDF calculated are shown in Figure 1.8, also shown are the observed values of the same for the MW and Andromeda. The analytical expression of the VDF is valid up to $V_{\rm circ} > 20\,{\rm km\,s^{-1}}$, but are extrapolated to as low as $V_{\rm circ} \simeq 10\,{\rm km\,s^{-1}}$, in [85]. It is seen that the observed and estimated VDFs agree with each other at $V_{\rm circ} = 50 - 60\,{\rm km\,s^{-1}}$ and above. However, at lower velocities, the simulations over-predict the number of satellites almost five times more than the observed values. When the analytical expression is extrapolated to $V_{\rm circ} = 10\,{\rm km\,s^{-1}}$, the disagreement rises to 15 times. Moore et. al. independently performed another analysis in the same year [86], and they found a similar order of over production of satellites while agreeing with VDF produced by [85]. The VDF computed by Moore et. al.

work is shown in Figure 1.8.

Together these two works lead to the belief that either the hierarchical structure formation theory is wrong or the halos did not attract baryons to form satellite galaxies. It is also possible that some of the satellites are too faint to observe or got destroyed later by tidal stripping. It is worth mentioning that many MW satellites have been discovered by the recent SDSS survey and it is now believed that a huge number of satellites ($\simeq 5 - 20$ times the bright satellites) are not yet discovered.

1.5.3 The "Too-Big-to-Fail" Problem

This problem addresses the marked breakdown of the galaxy luminosity- halo mass relation [107] observed in the bright satellites of the MW [88] and in the Local Group(LG) of galaxies [87]. The issue is elaborated below.

In the left panel of Figure 1.10, a comparison of rotation curves of nine bright dwarf spheroidals(dSph) satellites of the MW, all at $z = 0$, with curves predicted by the NFW profile are shown. The sizes of the data points are proportional to the luminosity of the individual dwarfs. The bands show the scatter of $r_{\rm max}$ at a fixed $V_{\rm max}$, where $V_{\rm max}$ and $r_{\rm max}$ are the maximum circular velocity and the radius where it is maximum.

It is evident from Figure 1.10 that all of the nine luminous dSphs are consistent with $V_{\rm max} \leq 18 - 24\,{\rm km\,s^{-1}}$ other than Draco, with no definite trend between the luminosity and mass of host halo. Two of the faintest dwarfs, Draco and Ursa Minor, are hosted in very massive haloes, whereas the three brightest dwarfs, i.e., Sculptor, Leo I and Fornax are held inside halos which are far less massive than the hosts of the faint ones. This observation either questions the well-established relation between the satellite luminosity - halo mass relation or conveys that the MW is just a statistical anomaly of the stochastic structure formation process. In the same work, the relation was checked at two other redshifts between $z = 0$ and $z = 10$ for ten most massive subhaloes used in the simulation, and it was found that the relation is not maintained in any of the redshifts either. This means that the formation process of MW dSphs in the ΛCDM regime, at least after the onset of the Epoch of Reionization(EoR), is highly affected by baryonic phenomena that can change the global luminosity - halo mass relation or the nature of dark matter is different from CDM at galactic scales.

The right panel of Figure 1.10 represents the rotation curves for a collection of luminous

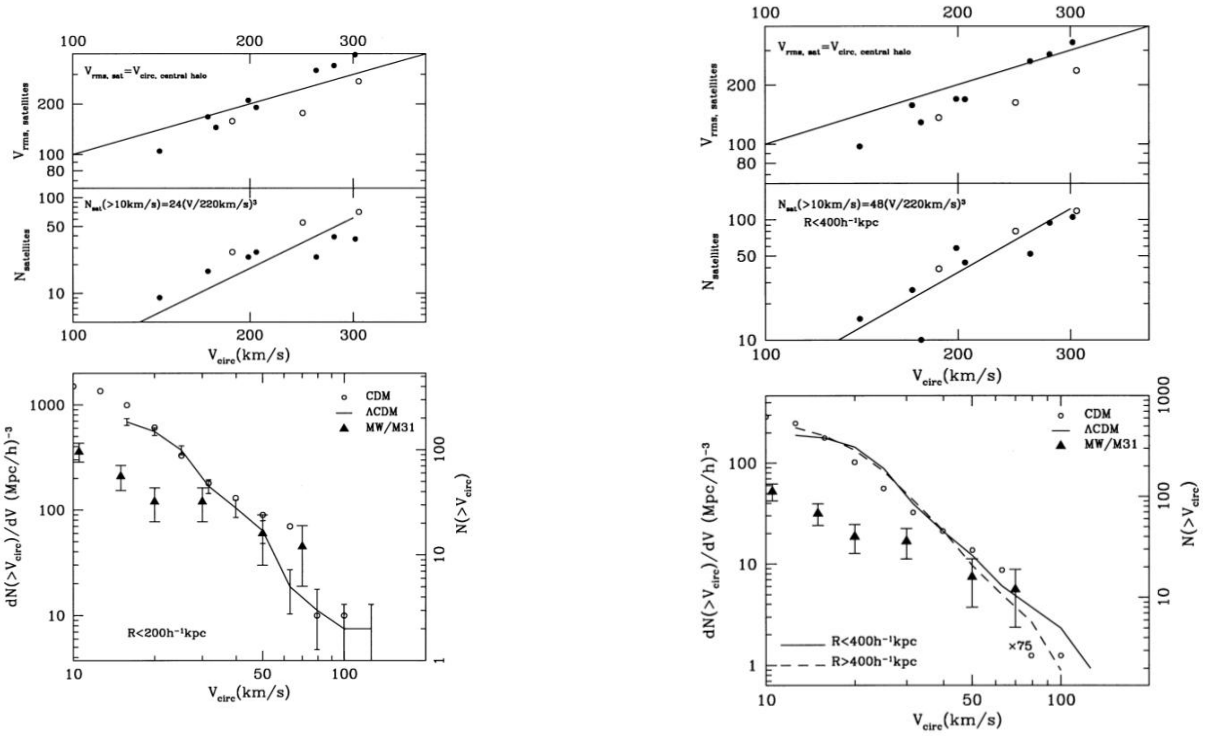

Figure 1.8: Properties of satellite systems within $200h^{-1}$(Left) and $400h^{-1}$ kpc from the host halo. In each figure the upper panel shows the RMS velocity dispersion, the middle panel indicates the number of satellite and the lower panel shows the VDF, all as functions of circular velocity. The discrepancy between theory and observation are more at lower circular velocities. All the figures are taken from [85].

dSphs that lie within 1.2 Mpc of the MW or M31 but farther than 330 kpc from both of them. The phrase "massive failure" written in the plot stands for the fact that a halo with $V_{\rm max} > 30\,{\rm km\,s^{-1}}$ does not host a luminous galaxy. It is evident from this plot that the breakdown is not a phenomenon related to the MW only but also seen in the local group of galaxies too. Curiously the brightest dwarf, IC1613 is hosted by one of the lowest massive haloes.

1.6 Possible Remedies of the Problems

The problems mentioned above appear to question the validity of the standard ΛCDM model in galactic scales. Primarily, there are two ways to solve these problems. One is to include

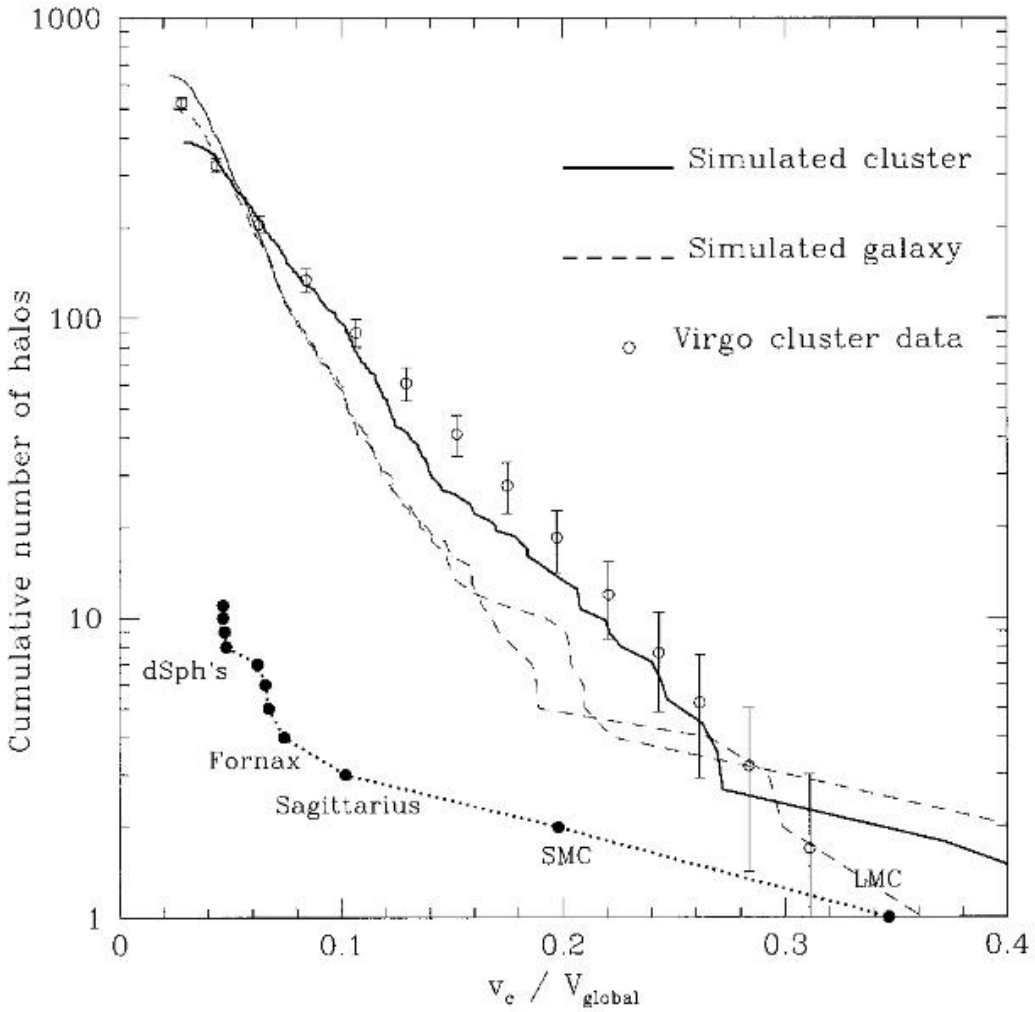

Figure 1.9: VDF for different satellites as a function of circular velocity of a halo, normalized to the global circular velocity of the parent halo. This figure is taken from [86].

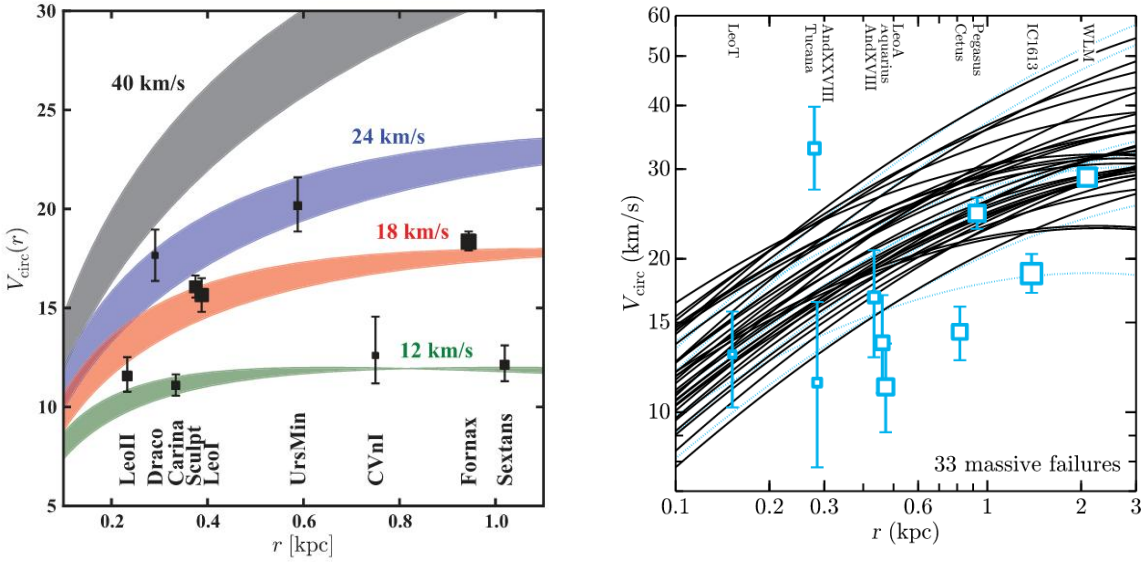

Figure 1.10: The Too big to fail problem as seen in The MW(Left) and the Local group(Right). Each of these plots show the circular velocities of host haloes of the respective dwarfs as a function of the radius. The sizes of each squares are proportional to the luminosity of the dwarfs. As seen clearly,the most luminous dwarfs are not hosted by the most massive haloes. The figures are taken from [88] and [87], respectively.

baryonic physics in the simulations. The old N-body simulations contain mostly CDM to study the evolution of structures in the universe and do not consider the details of the baryonic phenomena, which is not the case in reality. Many following works have considered baryonic physics including star formation, feedback, supernova explosion, tidal disruption of satellites by giant galaxies into their simulations. These modifications seem to solve the problems partially on the galactic scale, but when it comes to the group of galaxies, which is too large to be affected by the baryonic phenomena, these formalisms eventually fail to reproduce the observations [108]. Moreover, including baryonic physics in simulations is a complicated job and often involves a case-specific study, including environment dependence.

Another way to approach these problems is to change the dark matter candidate altogether. Dark matter particles having low mass, and thus higher free-streaming velocity, erase structures below their free-streaming scales. Dark matter with different formation mechanism can also have a lower amount of small-scale power. Because of low power at small scales, the mass

function, defined as the number of objects at a particular interval of mass, is lower at a lighter mass range. Thus, the small-scale power suppression naturally tends to decrease the number of satellites for an MW type galaxy or the density of dark matter in the central part of a galactic halo. Unlike treatments involving baryons, invoking new dark matter candidate may have the potential to solve all the problems in one stroke.

1.6.1 Including Baryonic Physics

The core-cusp problem was first addressed using baryonic physics by Navarro et. al. in 1996 [109]. In this work, the authors proposed that the central dark matter profile of the galaxy can be cored due to huge mass outflow from the galaxy. The mass outflow can be triggered by massive supernova bursts in the disk of the galaxy, which takes place shortly after the baryonic materials got assembled in the disk but before they end up forming stars. These bursts throw out gas from the disk and allow the dark matter to expand. The core thus created has a radius depending sensitively on the mass and size of the disk. As these parameters are already constrained by Big Bang Nucleosynthesis(BBN) and angular momentum conservation, this analysis puts a strong upper bound on the central concentration of matter for a halo of a given mass, and the core radius turns out to be a tiny fraction of the original halo radius. The possibility of the presence of CDM in the haloes are not ruled out, and the expulsion of baryonic materials can explain the observed low baryon abundance in the dwarfs. The same work was repeated by de Blok and Bosma in 2002 [104] with larger samples which strengthened this proposal.

More recently, a few other works [110,111] have also addressed this issue. In 2012, Pontzen and Governato [111] proposed a scenario where energy is transferred to dark matter particle orbits, through rapid and repeated oscillations of the central gravitational field. The oscillations are caused by concentrated star formation bursts that heat up the surrounding gas. Their simulations show that this process quantitatively accounts for the core formation during $2 < z < 4$. Models with lower star formation threshold do not produce core even after forming more stars, implying that it is the star formation rate that controls the core formation. This study prefers not to throw out a massive amount of material as suggested by [112] and allows to form a thin stellar disk at later times. Later in 2014, Ogiya and Mori [110]] has suggested the reason for the transition of cusp into core is the resonance between the dark matter particle

and the density wave generated by the external oscillating potential, causing kinetic energy transfer to the collisionless dark matter particles. The resonance, responsible for the cusp-core transition, happens when the oscillation frequency of the baryonic potential becomes equal to the local dynamical time: the overtone modes being the resonant states. The analytical model was compared to N-body simulation, and reasonable agreement was found.

Some conventional solutions proposed for the missing satellite problem are to consider suppression of gas accretion and photoevaporation by cosmic ionizing sources [113–115], as well as ram pressure stripping along with tidal mass loss [116]. In 1996, Quinn et al. explored [113] the effects of photoionizing background at $z \simeq 2.4$ by simulating five halos with circular velocity $\simeq 46\,\mathrm{km\,s^{-1}}$. This work concluded that the effect is moderate on gas that collapses into halos and reduces the amount of collapsed gas by $40 - 90\%$. However, the amount of the radiation was found to have significant effects on the formation of smaller objects hosted by halos with virial mass $\lesssim 4 \times 10^9 M_\odot$ and circular velocity $\lesssim 37\,\mathrm{km\,s^{-1}}$. Three years later, Barkana et al. [114] extended this research to the EoR. During reionization, most of the cosmic gas was incorporated into halos with virial temperature $\lesssim 10^4$K, which was pulled out of the host halos by the cosmic UV background that started the reionization. Assuming spherical dark matter halo and Press-Schechter(PS) mass function [117], they calculated the photoionization heating of gas and found that $50 - 90\%$ of the gas is heated above the virial temperature and thus expelled out of the halos. Though this amount of gas depends crucially on the reionization redshift and the star formation history, it is not very sensitive on the halo and gas profile. The small amount of gas located at the core of the halos is shielded from ionization. This process lasted for almost one Hubble time and made the halos highly dark matter dominated. The results of this work were further reinforced by later research by Bullock et. al. in 2000 [115]. The main result of this study was that for halos with circular velocity $\lesssim 30\,\mathrm{km\,s^{-1}}$, the mass accretion is highly suppressed by the UV background during EoR and a small fraction (30%) of halos that retained substantial fraction of their baryonic mass are visible today. Using EoR redshift to be at $z_{re} = 8$ and PS mass function they successfully produced the VDF that was theoretically calculated using NFW halo profile, assuming that 30% of the subhalo mass was already there before z_{re} so that they are visible today. This fraction of gas that survives inside the halo was also reproduced by a more recent work [116] which shows that the progenitors of the dark matter dominated satellites carried a considerable amount of baryonic matter in

earlier times. A combination of tidal stripping and ram pressure took away most of its baryonic materials from it which was loosely bound to them. With improved data provided by SDSS DR7, more faint satellites have been found, and it is believed that many other dark matter dominated satellites will be found with better instruments.

Tidal Stirring of satellites has been explored as a potential solution to the "Too big to fail" issue in recent times [118]. The authors used a high-end cosmological simulation suite that includes both dark matter and baryonic physics and has a forced resolution as good as 10 pc, to study the tidal effects of a host halo with a size comparable to that of the MW. The stellar feedback can modify the central dark matter profile, changing it to core from cusp. The tidal effects after the infall can snatch baryonic material from the dwarfs, along with repeated tidal shocks that further modified the dark matter and baryonic profiles. The stellar mass-halo mass relation was found to be modified most for halos with mass $\lesssim 10^9 M_\odot$, making it difficult to use the abundance matching techniques to dwarf galaxies. A more recent work [119] has also reached the same decision by analyzing the HI kinematics of the dwarf galaxies. It is found that the VDF that is inferred from the HI data are often underestimated, with respect to the one which is extracted from the enclosed mass. The total mass of the host halo is also underestimated if the HI kinematics is fitted with the theoretical halo profile. The reason for this discrepancy can be the violent nature of the interstellar mediums(ISM) of the dwarfs, because of the continuous tidal stirring due to massive supernova explosions. This violent nature of the ISM makes it impossible to trace the underlying gravitational field by using the velocity profile and thus an underestimation of mass is natural leading to an apparent breakdown of the global halo mass- galaxy luminosity relation. Supernova feedback has also been suggested as a solution for this problem [120], as proposed by the core-cusp problem too.

1.6.2 Changing the nature of Dark Matter

Cutting down power at small scales by lighter particles can be another approach to solving the small-scale issues. The HDM cuts power at small scales due to its high free-streaming velocity. However, it can never be the right alternative of CDM for solving the small-scale problems because it gives rise to even more serious issues, as discussed in Subsection 1.2.1. The next step was to introduce a dark matter candidate that has a free-streaming velocity considerably smaller than HDM so that the problems created by HDM do not come back. However, the

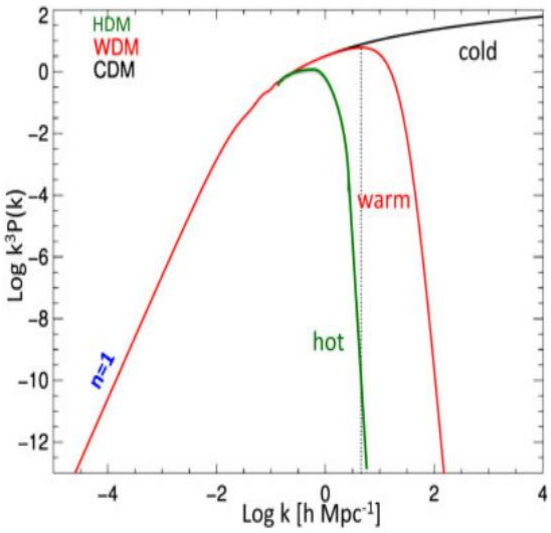

Figure 1.11: The power spectra for hot, war and cold dark matter. The HDM, with mass of O(10 eV) and thus having the highest free-streaming velocity, cuts power at the largest scale. The WDM, with mass O(1 keV), cuts power at smaller scale. This plot is taken from [121]

candidate must also cut power at small scales so that it can have the potential to solve the small-scale issues. These necessities, together, bring the attention of the community to the WDM: a cooled down version of HDM. For comparison, we have shown the power spectra of the three types of dark matter below:

Warm Dark Matter

Warm dark matter(WDM) particles with a mass of $\simeq 1\,\mathrm{keV}$, inspired by particle physics models of sterile neutrinos, have been advocated as a solution to the small-scale anomalies of CDM. Sterile neutrinos in this mass range cannot be detected in standard WIMP searches, at least with current experimental capabilities. Nevertheless, in galactic X-ray data, its imprint can be captured if a dark matter sterile neutrino decays to a photon and a relativistic active neutrino. This photon would have keV energy which, in principal, can be detected as a galactic X-ray excess. Recent X-ray anomalies from XMM-Newton and Chandra data can be explained by the decay of a 7 keV WDM [122].

WDM can be produced thermally or non-thermally in the early universe. If they are not produced thermally, there are many formation scenarios suggested in the literature. The most

well-studied candidate of these non-thermal WDM is the sterile neutrino. Broadly, they can form by oscillation of active neutrino to sterile neutrino or decay of a primordial heavy particle. For WDM produced by oscillations, the oscillations can be "non-resonant" or "resonant." The resonance happens at an energy where production of the sterile neutrino is sharply enhanced. These two mechanisms can be connected through a primordial lepton number asymetry. The lepton number asymetry in the Neutrino Sector vanishes in case of the "non-resonant" production and does not when the production is "resonant." We briefly provide a description of sterile neutrino production by oscillation in the next few paragraphs.

The "non-resonant" mechanism is well-known as the Dodelson-Widrow(DW) Mechanism [123]. In this scenario, sterile neutrino produced in the early universe at $T \simeq 100$MeV, plays the role of WDM and the ratio of the number density of sterile neutrino and active neutrino reaches its peak at $T_{\rm max} \simeq 133$MeV. It falls off as T^3 and T^{-9} at very low and very high temperatures respectively. At high temperature, finite temperature and damping effects suppress the formation of sterile neutrino whereas at low temperature the fading of collision is responsible for cutting down the sterile neutrino production. At very low temperature the sterile neutrino distribution function becomes identical to the active neutrino with an effective suppression ξ in the normalization.

Recently a more detailed study [124] has provided a better fit of the WDM mass with the observed dark matter density using the following relation

$$m_{\rm wdm} = 3.40\,{\rm keV}\left(\frac{\sin^2(2\theta)}{10^{-8}}\right)^{-0.615}\left(\frac{\Omega_{\rm dm}}{0.26}^{0.5}\right) \times \left(0.527\,{\rm erfc}\left[-1.15\left(\frac{T_{QCD}}{170\,{\rm MeV}}\right)^{2.15}\right]\right) \tag{1.18}$$

here $\Omega_{\rm dm}$ is the relic density of dark matter, $m_{\rm wdm}$ is the mass and T_{QCD} is the QCD phase transition temperature.

In the resonant production of sterile neutrino, the Shi-Fuller(SF) Mechanism [125], the sterile neutrino distribution function is peaked at a certain energy in the energy spectrum. The resonant production is driven by a primordial lepton number asymmetry. To make the oscillation adiabatic, the energy at which the resonance happens ($\epsilon_{\rm res}$) and mass of WDM obey the following condition

$$4\times 10^9\left(\frac{m_{\rm wdm}}{10^2{\rm eV}}\right)\left(\frac{\mathbf{L}}{0.1}\right)^{3/4}\epsilon_{\rm res}^{-1/4}\times\sin^2(2\theta)\left(\frac{1}{1-(d\mathbf{L}/dt)/4H\mathbf{L}}\right) > 1 \tag{1.19}$$

where **L** denotes the contribution of leptonic asymmetries in the effective potential for oscillation. The transition is only adiabatic when **L** is a significant fraction of its initial value which means that only the low-energy states of the non-thermal sterile neutrino energy spectrum are populated in this mechanism. The higher energy states are resonantly produced through non-adiabatic process leading to no significant active-sterile conversion.

Any particle that decouples in the early universe when still relativistic can be a thermal WDM candidate. The temperature of any such species is given by

$$T_x = T_\gamma \left(\frac{4}{11}\right)^{1/3} \left(\frac{10.75}{g_*(T_D)}\right)^{1/3} \tag{1.20}$$

where T_D is the temperature when the species decouples and g_* is its effective DOF at $T = T_D$. From the equation, it is understood that the distribution function of a particle that decouples when $g_* \gtrsim 11$ will have a lower temperature and number density. Hence, the particle will have a lower velocity dispersion and higher mass than the HDM and thus can be a thermal WDM candidate.

The present day abundance of WDM is given by

$$\Omega_{\rm wdm} = \beta \left(\frac{m_{\rm wdm}}{94.7{\rm eV}}\right) \tag{1.21}$$

where $\beta = (T_{\rm wdm}/T_\nu)^3$ for thermally decoupled WDM and $\beta = \xi$ for WDM produced by oscillation. For WDM with Fermi-Dirac distribution function the mass of thermally decoupled WDM and WDM produced by DW mechanism are related as follows

$$m_{\rm DW} = 4.46\,{\rm keV} \left(\frac{m_{\rm thermal}}{1\,{\rm keV}}\right) \left(\frac{0.12}{\Omega_{\rm wdm}}\right) \tag{1.22}$$

In the early universe, WDM is highly relativistic, and its free-streaming scale is the horizon at that time. As time proceeds, it cools down and passing through its semi-relativistic phase; it finally becomes non-relativistic CDM. The free-streaming scale during its semi-relativistic phase is given by [126]

$$k_{\rm fs} \simeq \left(\frac{0.3}{\Omega_{\rm wdm}}\right)^{0.15} \left(\frac{m_{\rm wdm}}{\rm keV}\right)^{1.15} {\rm Mpc}^{-1} \tag{1.23}$$

In the matter power spectrum produced by WDM, power is cut at the WDM free-streaming scale, and it falls smoothly because the thermal velocity of WDM decays as $1/a$ and is not small enough to allow clustering at small scales for a long time (Figure 2.1 in Chapter 2). Clearly,

lighter WDM will cut power at larger scales (e.g. [126]). This free-streaming also suppresses the formation of low-mass halos or sub-halos and its finite phase-space density prevents the development of density cusps [127, 128].

The first simulation of structure formation in WDM cosmology was done by Bode et. al. in 2001 [126]. The mass below which structures form by top-down hierarchy was found to be decreased by several orders of magnitude. There are visible differences between the density contrasts of the matter distribution in the ΛCDM cosmology and the WDM cosmology, as shown in Figure 1.12 below. The small-scale structures were rarer in WDM and became even rarer if the mass of WDM is decreased. The WDM halos exhibited lower densities and central concentrations than the CDM halos. It was also shown in the same work that the dwarf galaxies were formed after the MW sized galaxies, which is again not the case for ΛCDM. The WDM thus appears to provide better agreement with the available observations. Further investigations involving simulations of the Lyman-α forest power spectra, the study of the history of the structure formation and most importantly, verification of its credibility to solve the small-scale problems were yet to be done.

The Lyman-α forest power spectra have been simulated by many groups [127, 129]. One of the most recent simulations is performed by Baur et. al. [130] using a large sample of quasar spectra and state-of-the-art numerical techniques. The mass of WDM is constrained as follows: $m_\chi > 4.09$keV for an early decoupled thermal relic, and $m_s > 24.4$keV for a non-resonantly produced right-handed sterile neutrino, both at 95% CL. The small-scale problems were also approached by various groups. The core-cusp problem was considered in [131] and they found that to create a core of radius one kpc in a dwarf galaxy with halo mass $10^{10} M_\odot$, a WDM candidate with mass 0.1 keV is required. Unfortunately, such a light WDM candidate will not allow structure formation at that scale due to its high free-streaming velocity. To allow structure formation a WDM candidate with mass $\simeq 1-2$ keV is required, which gives rise to a core of radius ten kpc for a dwarf with the same halo mass. Thus, the WDM cannot be a viable solution for the core-cusp problem. Another simulation of non-linear structure formation in WDM paradigm was performed in the same year [131] using five WDM candidates with masses ranging from 0.25 to 1.25 keV. The authors found that on small scales WDM and CDM behave identically. The NFW profile was again a good description of halos in WDM cosmology and no central density core was found. The missing satellite problem was approached by Polisensky

et al. in 2010 [132]. Assuming that the simulation produces satellites in equal or more number than observed, they found the constraints on WDM mass to be > 2.3 keV for the thermal relic, and > 13.3keV for non-resonantly produced WDM. Finally the too big to fail problem was addressed by Lovell et al. in 2011 [133]. By using a resonantly produced WDM candidate with mass 2 keV, which is equivalent to ~ 0.53 keV thermal relic, this issue can be solved. Therefore, the allowed mass ranges of WDM, those are found to solve the small-scale issues, are evidently in conflict with each other.

Going beyond WDM

The previous discussion shows that the small-scale issues are either not solved by WDM or if they are solved, the constraints thus put on the mass of WDM, are in conflict with each other. So, it is clear that some alternative of WDM must be found to solve the small-scale problems, with constraints on dark matter properties that are consistent with each other. Various other alternatives are suggested in the literature. One of them is the Late Forming Dark Matter(LFDM) [1] which is formed by phase transition in the neutrino sector long after the BBN. Another is the Ultra Light Axion Dark Matter(ULADM) [2, 134] where a very light axion-like particle is formed in the early universe by spontaneous symmetry breaking. The particle then produced was stuck to its initial condition by Hubble drag, and later after getting rid of this drag, it starts behaving like dark matter. The last candidate we consider in this thesis is the Charged Decaying Dark Matter(CHDM), where the dark matter is formed after an instantaneous decay of a massive charged particle [3], again long after the BBN. The light neutral particle produced after the decay behaves as dark matter. In the following chapters, we provide descriptions of these models and also study how these new candidates can affect the evolution of the universe.

1.7 Organization of this Thesis

The thesis is comprised of four chapters based on three publications. The thesis is organized as follows:

- In Chapter 2 we have described three non-standard dark matter candidates: LFDM, ULADM, and CHDM. We have discussed their origins in particle physics along with

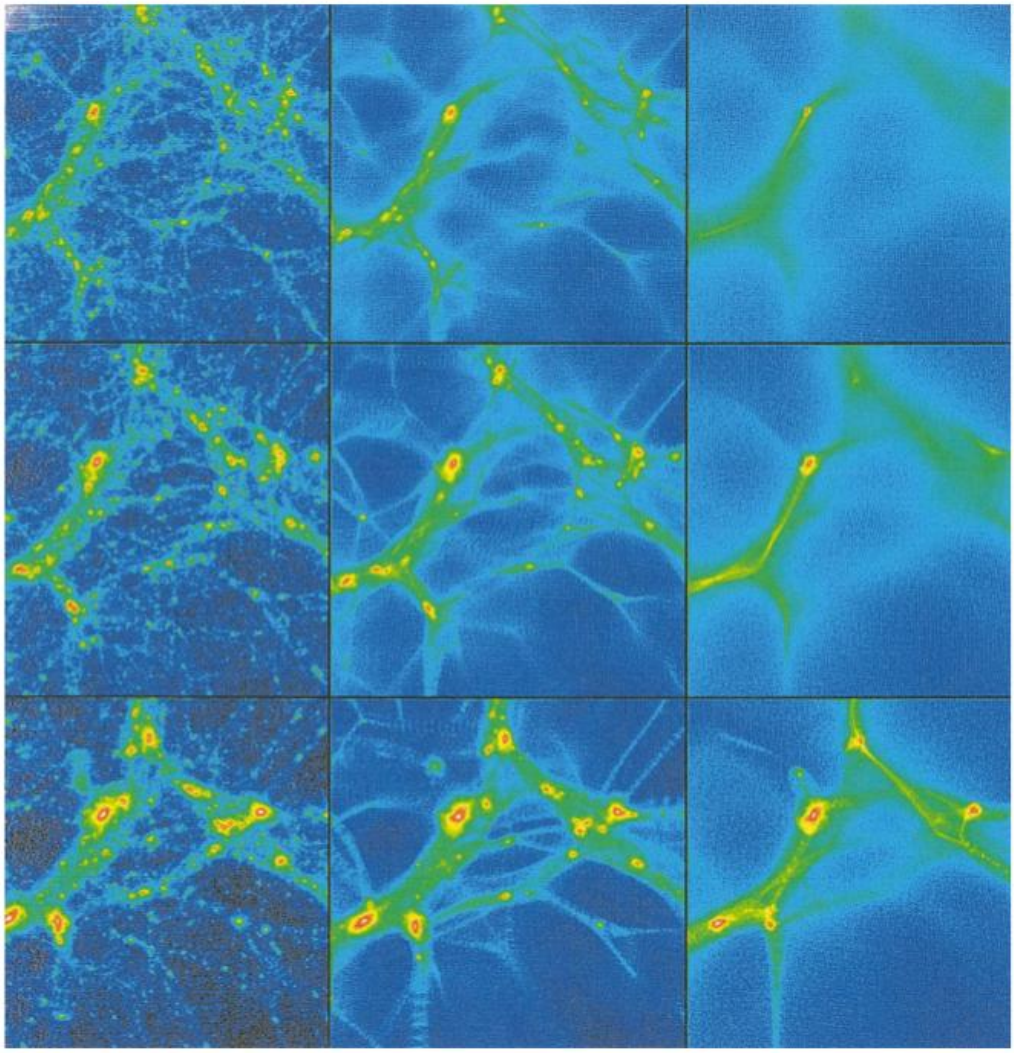

Figure 1.12: Projected density fluctuation map for ΛCDM, WDM with mass 350eV and 175eV from left to right panel at z=3,2 and 1 as plotted from top to bottom. The small-scale structures are rarer in WDM and become even rarer if the mass of WDM is decreased. The clustering becomes stronger at late time, as expected. This figure is taken from [126]

their particle properties. We have also explored how they can modify the matter power spectrum, especially the small-scale region.

- In Chapter 3, we have performed a more detailed study of one of the three new candidates, the LFDM. We have created a set of matter power spectra changing the model parameters and performed a χ^2 analysis to compare the predictions with observational data. We have used data in both large and small scales and produced contours that constrain the dark matter properties.

- In Chapter 4 we have studied effects of the non-standard dark matter candidates on the EoR. We have also explored the evolution of collapsed fraction of gas at high redshifts in the presence of new dark matter physics, along with the WIMP CDM. We have included another dark matter model here, the ULADM, and constrain the properties of both of these models using real arguments and observational data.

- In Chapter 5 we have considered the spectral distortion in the CMB as our cosmological probe of interest. We have studied how the amplitude of the y-distortion parameter and the spectral nature of y-distortion changes with small-scale power suppression due to new dark matter candidates. We also argue why only late time spectral distortions will be affected by the small-scale power suppression. We have discussed the possibilities of detecting the differences induced in the distortion parameter and the distorted spectrum by future experiments.

- In Chapter 6, we provide a comprehensive overview of the results of Chapter 3, 4 and 5. We also discuss some projects that will be considered in future to extend this study further.

Chapter 2

Some Alternatives of the WIMP: LFDM and Friends

In the last chapter, we have explained that the dark matter is an essential candidate to form structures in the universe, along with the fact that dark matter is all over in the universe starting from sub-galactic scales to largest structures seen so far. It has also been pointed out that the standard WIMP dark matter scenario, though quite successful in describing the large-scale features of the universe, does suffer from some small-scale issues. It was suggested in that context that a suppression of power at small scales may help to solve those problems. This chapter contains more focused discussion on the small-scale power suppression. Here, we consider three well-motivated dark matter candidates, proposed as alternatives to the WIMP dark matter: Late Forming Dark Matter(LFDM), Ultra Light Axion Dark Matter(ULADM) and Charged Decaying Dark Matter(CHDM). Though all the four dark matter candidates have diverse physical origins, they exhibit unity in one sense: "All of them suppress the power at small scales". Depending on their origins and particle properties, the corresponding power spectra show different behaviors at small scales. In this chapter, we describe the particle physics origins of the models considered in this work and briefly discuss their cosmological signatures. We also show the time evolution of their transfer functions. The LFDM, ULADM and CHDM models are discussed in Section 2.1, 2.2 and 2.3, respectively. Finally, the evolutions of theirs transfer functions are presented in Section 2.4.

2.1 Late Forming Dark Matter

In this section, we discuss how LFDM models differ with respect to their production mechanism and the formation epoch as compared to the other dark matter candidates. For the case of electroweak WIMP, the dark matter is formed through freeze-out when the temperature of the universe falls to $m_{\rm dm}/T \simeq 20$—so the production happened at very early times ($T \simeq$ a few GeV) much before the epoch of BBN. For the case of keV sterile neutrino WDM, when it is produced through active-sterile oscillation, the production epoch is $T \simeq 150\,\text{MeV}$. For the case of axion dark matter, the scalar starts its coherent oscillation when the mass of the scalar field becomes of the order of Hubble parameter $m_\phi \sim H(T)$. For the accepted mass scale of sub-eV axion $m_a \simeq 10^{-5}\,\text{eV}$, the production happens at the QCD scale $T \simeq 100\,\text{MeV}$ which also precedes the epoch of BBN.

The main difference between the models discussed above and LFDM models is that the formation of CDM can be as late as epoch corresponding to $T \simeq$ eV. It is instructive to note that for WDM models, one gets suppression in matter power owing to the free streaming effects which are governed by the dark matter mass. However, in our case, the suppression is controlled by the redshift of LFDM formation rather than its mass scale. This is the reason that in LFDM models the existing cosmological data directly constrain the redshift of the dark matter formation.

2.1.1 Scalar LFDM

In this scenario, the dark matter is formed as a consequence of phase transition of a scalar field. The scalar field, which was initially trapped in a metastable minimum by thermal effects or due to its interaction with other scalar fields resulting in a hybrid potential in the early universe, makes a phase transition (which is generally between the redshift of BBN and MRE in this model) to the true minima. After this, the scalar field starts oscillating coherently and its equation of state changes from $w = -1$ to $w = 0$, making it clump exactly like the CDM. The dynamics of the phase transition is very similar to the case of the hybrid inflation [135], where the scalar field plays the role of the waterfall field and behaves like dark matter after the phase transition. The hybrid potential for two scalar fields in the context of LFDM was

derived in [1, 136] and is given by

$$V(\phi_1, \phi_2) = (\lambda\phi_1^2 - \mu^2)^2 + 4\,\lambda^2\phi_1^2\phi_2^2 + M^2\phi_2^2 \tag{2.1}$$

For a high value of $\phi_2(T)$ in the early universe, the scalar field is trapped in a metastable minimum $\phi_1 = 0$ behaving like the cosmological constant. Later, at a critical redshift z_f, ϕ_1 becomes Tachyonic and rolls down to the true minima. After reaching the true minima, ϕ_1 exhibits coherent oscillations and behaves exactly like the CDM. For details of this model, we refer the reader to [1].

As discussed in [1] it is possible to achieve it by interactions beyond the standard model in the neutrino sector; these interactions allow the scalar field to be held in a metastable minimum. Once the neutrino temperature drops below a critical value, the LFDM is formed. One of the advantages of the LFDM appearing from neutrino dark energy theories is that the epoch of phase transition is naturally predicted to be very late and is subjected to constraints arising from linear perturbation theory. The range for LFDM formation epoch stemming from neutrino dark energy is given by [1]: $1\text{eV} < \mathrm{T_f} < 10^3\text{eV}$. The length scales corresponding to the horizon entry for this range of epochs are: $2 \times 10^{-2} h Mpc^{-1} < k_f < 20\, h\, Mpc^{-1}$. This bound is purely theoretical assuming natural values of the coupling constants.

2.1.2 Fermionic LFDM

A light fermion-like eV sterile neutrino can be trapped into a fermion nuggets by a phase transition driven by a strong scalar interaction. Initially, the idea of fermion nugget formation was proposed in [137]. However, in their work, the dark matter like nuggets form much later than MRE. In a recent work (section 3 of [138]), it was shown that light sterile fermion behaving like dark radiation could be trapped in heavy dark matter nuggets. The stability of the nugget is achieved when attractive fifth force is balanced by degenerate Fermi pressure of the light fermions inside the nuggets. There are mainly two main equations which need to be solved to get the nugget mass, radius, and density:

$$\begin{aligned} \phi'' + \frac{2}{r}\phi' &= \frac{dV(\phi)}{d\phi} - \frac{d[\ln(m(\phi))]}{d\phi} T^{\mu}_{\mu} \\ \frac{dp}{d\phi} &= \frac{d[\ln(m(\phi))]}{d\phi}(3p - \rho) \end{aligned} \tag{2.2}$$

We refer to [139] for detailed derivation of these equation. Briefly, the first one is the Klein Gordon equation for $\phi(r)$ under the potential $V(\phi) = \lambda\phi^4$ where the fermions act as a source term for $\phi(r)$. The other equation tells us how the attractive fifth force is balanced by local Fermi pressure.

From the above discussion, it is clear that the most important parameter of this model is the redshift of formation z_f. Once the phase transition happens, there is a fractional drop in neutrino degrees of freedom $N_{\rm eff}$, as the radiation component starts behaving as CDM immediately after the phase transition. This gives us one more parameter of interest: $N_{\rm eff}$.

Since the epoch of phase transition until the present, LFDM redshifts as normal CDM, one gets

$$\rho_{\rm lfdm}^{(z_f)} = \rho_{\rm lfdm}^{(0)}(1+z_f)^3 \tag{2.3}$$

Now assuming that a fraction of excess radiation component got converted into a fraction of CDM density, $f_{\rm lfdm}$, at $z = z_f$, we get the decrement in the effective number of neutrino degrees of freedom, $\Delta N_{\rm eff}$ to be:

$$\Delta N_{\rm eff}\rho_\nu^{(z_f)} = f_{\rm lfdm}\rho_{\rm lfdm}^{(0)}(1+z_f)^3 \tag{2.4}$$

where $\rho_\nu^{z_f}$ is the energy density of one neutrino-like radiation species at the formation redshift. This yields:

$$\Delta N_{\rm eff} = f_{\rm lfdm}\frac{\rho_{\rm dm}^{(0)}}{\rho_\nu^{(0)}} = 1.7 f_{\rm lfdm}\Omega_{\rm dm}h^2\left(\frac{10^5}{1+z_f}\right) \tag{2.5}$$

It should be noted that $\Delta N_{\rm eff}$ is inversely proportional to the redshift of formation. As the effective number of neutrino degrees of freedom dynamically change in this model, observational constraints on $N_{\rm eff}$ from different observations need to be interpreted properly.

For instance, for $z_f < 10^{10}$, the BBN constraints, which depend on the in situ value of $N_{\rm eff}$ during the era of BBN, apply to the value of $N_{\rm eff}$ before the epoch of dark matter formation. [140, 141]. On the other hand, CMB and galaxy clustering data, which are influenced by the history of changes in $N_{\rm eff}$, are also sensitive to the final $N_{\rm eff}$. Throughout this thesis $N_{\rm eff}$ corresponds to the initial degrees of freedom. We also note that, for most of the range of z_f of interest, $\Delta N_{\rm eff}$ is generally smaller than the current precision on $N_{\rm eff}$ from different datasets; for instance, it follows from Eq. (2.5) that even if $f_{\rm lfdm} = 1$, $\Delta N_{\rm eff} = 0.2$ for $z_f = 10^5$, assuming the best fit Planck parameters for $\Omega_{\rm dm}h^2$. As noted above we also consider the case when the LFDM contributes only a fraction to the observed CDM at present and this fraction is denoted

by $f_{\rm lfdm}$.

For both of the scenarios mentioned above, LFDM gets its initial conditions for evolution from the massless neutrino. If LFDM is formed at $z = z_f$, power is suppressed sharply at a scale $k = k_{\rm lfdm}$ that entered the horizon at that redshift. Unlike WDM, the suppression is sharp as the dark matter is assumed to form via an almost instantaneous phase transition (Figure 2.1). At $k < k_{\rm lfdm}$, the matter power spectrum carries damped oscillations, a typical feature exhibited by the massless neutrino. This is in contrast to WDM where the power falls monotonically without any oscillation. Earlier the dark matter forms, smaller is the scale where the decrement of power occurs. The cosmology of this model is studied in [4] and it is found that dark matter should form deep inside the radiation dominated era and before $z_f \simeq 0.98 \times 10^5$. In the present work, we consider LFDM having formation redshift in the range $5 \times 10^4 < z_f < 5 \times 10^5$. To generate the power spectrum and transfer function in the LFDM regime we have modified the codes as follows:

$$\begin{aligned} \dot{\delta}_{\rm lfdm} &= \dot{\delta_\nu} \\ \dot{\theta}_{\rm lfdm} &= \dot{\theta_\nu} \quad \text{For z} \leq \text{z}_\text{f} \end{aligned} \tag{2.6}$$

$$\begin{aligned} \dot{\delta}_{\rm lfdm} &= \dot{\delta_c} \\ \dot{\theta}_{\rm lfdm} &= \dot{\theta_c} \quad \text{For z} > \text{z}_\text{f} \end{aligned} \tag{2.7}$$

We will discuss the modification of the codes in detail in Chapter 3.

2.2 Ultra Light Axion Dark Matter

Another very well studied dark matter is the dark matter from ultra light axion (ULA) fields in the context of string axiverse [142]. Before going into the details of the ULA model, we will briefly discuss the potential of axions as a CDM candidate.

The concept of Axion was first brought into the picture as a solution to the strong CP problem of the Quantum Chromodynamics(QCD). The QCD Lagrangian contains a term

$\bar{\Theta}\frac{g^2}{32\pi^2}G^{\alpha\mu\nu}\tilde{G}_{\alpha\mu\nu}$, where $G^{\alpha\mu\nu}$ is the gluon field strength tensor and $\bar{\Theta}$ is related to the phase of the QCD vacuum. If the quantity $\bar{\Theta}$ is of the order of unity, it can give rise to a strong CP violating effect and make the electric dipole moment of the neutron to be 10^{10} times higher than the observed value. Thus, to agree with the observation the value of $\bar{\Theta}$ should be 10^{-10} times smaller. This disagreement is described as the strong CP problem. This issue was first approached by Peccei and Quinn in 1977. They have shown in their classic works that the value of $\bar{\Theta}$ can be pushed down close to zero due to a spontaneous breaking of a global U(1) symmetry. Later in 1977, Weinberg and Wilczek found independently that this spontaneous breaking of symmetry can give rise to a massive Nambu-Goldstone boson which is termed as the axion. The mass of this boson is given by $m_a \sim \lambda_{QCD}^2/f_a$, where f_a is the scale where symmetry is broken and λ_{QCD} is a parameter denoting the strength of the QCD potential. Initially, f_a was considered to be at the weak scale, leading to the mass of Axion to be 10MeV. However, it was eventually found that Axion with a mass greater than 1 eV could result in a very rapid cooling of the red giant stars than observed. Further observation of the Supernova 1987A put a stronger constraint on $m_a \lesssim 10^{-3}$ eV. Thermal production of such light particles can produce a deficient quantity of axions, which can make up only a tiny fraction of the total dark matter abundance. However, axions with lower mass can be produced non-thermally by misalignment of the Peccei-Quinn field. These axions are one of the very well-studied dark matter candidates, and misalignment mechanisms can produce axions with a density comparable to the present density of dark matter, for mass $m_a \sim 10^{-5}$ eV.

In this work, we consider axion-like particles with tiny mass, $m_a \sim 10^{-22}$ eV. These particles are well-known as the Fuzzy Cold Dark Matter [143]. The Compton wavelengths of such particles are inversely proportional to their mass and are comparable to the size of galaxies or cluster of galaxies. This hinders clustering of dark matter at smaller scales and offers a natural solution to the small-scale problems. An axion-like particle as a dark matter candidate can be described by [2, 134, 143, 144] a two-parameter model, whose action is given by:

$$I = \int d^4x\sqrt{g}\left[\frac{1}{2}F^2 g^{\mu\nu}\partial_\mu\phi_a\partial_\nu\phi_a - \mu^4(1-\cos\phi_a)\right] \tag{2.8}$$

where ϕ_a is a dimensionless and periodic scalar field, represented as $\phi_a \to \phi_a + 2\pi$. F and μ are the two parameters of the model. For sufficient small value of μ (which is the case for dark matter), it can be shown that mass of the scalar is given by $m_a = \frac{\mu^2}{F}$. For a cosmologically and astrophysically acceptable dark matter candidate, a reasonable value for the mass is

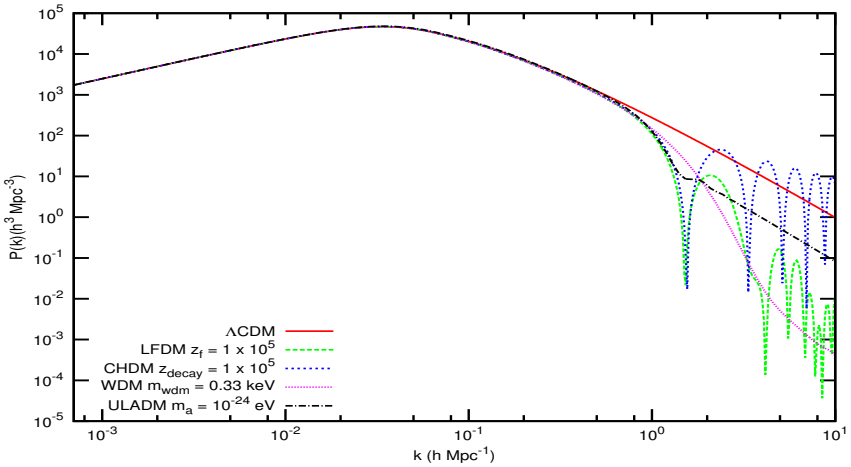

Figure 2.1: Normalized matter power spectra of the four dark matter candidates considered in this work along with ΛCDM are shown. For each of the non-standard dark matter candidate, the parameters are chosen such that the power is cut at nearly the same scale $k \simeq 0.3h\text{Mpc}^{-1}$. The specifications of the models are mentioned in the legend.

$m_a \simeq 10^{-22}$ eV. All models of particle physics derived from string theory have several periodic scalar fields such as ϕ_a and it has been argued that such a low mass is quite reasonable from particle physics perspective.

ULA obtains its initial conditions after spontaneous symmetry breaking in the early universe and behaves like a coherent scalar field. Early when H is high, the friction term dominates, and the field is stuck at some random initial value and behaves like the cosmological constant. Later, when $m_a \sim H(z)$ at a certain redshift, the field rolls off and start oscillating coherently around the nearest minima of the periodic potential and starts behaving like CDM. The adiabatic perturbations in the scalar field have a momentum-dependent and thus mass-dependent effective sound speed. At scales below the effective sound horizon, perturbations are washed out due to free-streaming, and the matter power spectrum features very similar to LFDM (Figure 2.1) are found in the matter power spectrum. The free-streaming scale is given by [134]

$$k_m \simeq \left(\frac{m_a}{10^{-33}eV}\right)^{1/3} \left(\frac{100\,\text{kms}^{-1}}{c}\right) h\,\text{Mpc}^{-1}. \tag{2.9}$$

This means that lighter axions will push the scale of suppression to a higher value. The

cosmologically relevant mass of ULA ranges from 10^{-18} and can be as tiny as 10^{-33} eV. Some recent works have put a lower limit on the mass of ULA: $m_a \lesssim 2.6 \times 10^{-23}$ [8,145]. In this work, we consider the mass range: $10^{-21}\,\mathrm{eV} > m_a > 10^{-25}\,\mathrm{eV}$. The matter power spectrum and other cosmological outputs for ULADM candidates are computed with the publicly available code `AxionCAMB`.

In a recent work [146] it was shown that self-gravitating bosonic fields like ULA could give rise to stable solitonic field configurations in the galactic halo. The thermodynamics of these solitons in the halo can lead to an NFW like profile of dark matter density in the outer parts of the halo while following a core profile near the center. Hence, this dark matter candidate can also be able to solve the core-cusp issue. The mass of ULA that can address the problem should be $< 10^{-22}$eV at 95% CL, as shown by the analysis done by the authors in the same work.

2.3 Charged Decaying Dark Matter

This model, its variants, and their cosmological implications have been investigated in detail [3, 147–149]. We consider a model in which a heavy negatively charged particle of mass $M_{\rm ch}$ decays into a heavy neutral particle of mass $M_{\rm neu}$ and a relativistic electron (supersymmetric models in which a selectron decays into an electron and a gravitino might achieve this scenario [3]). These two masses and the decay time τ parameterize the model. The decay time and the mass difference between the two heavy particles $\Delta M = M_{\rm ch} - M_{\rm neu}$ are tightly constrained because the relativistic electron thermalizes with electron-photon coupled system, thereby causing spectral distortion of CMB if the decay time corresponds to redshifts $z_{\rm decay} < 10^6$. The three-momentum of the relativistic electron $p = \Delta M$ and in the limit all this relativistic energy is transferred to the photon gas, we get the fractional energy increase:

$$\delta\rho_\gamma/\rho_\gamma \simeq 4.2 \times 10^{-2} \left(\frac{\Omega_{\rm dm}h^2}{0.11}\right)\left(\frac{10^5}{1+z}\right)\left(\frac{\Delta M}{M_{\rm ch}}\right) \tag{2.10}$$

Using the current bounds on μ and y-parameters, we get $\Delta M \lesssim 10^{-2}$–$10^{-3}$ for decay times in the redshift range $10^6 > z_{\rm decay} > 10^5$.

This constrains the energy density of the relativistic electrons to be dynamically unimportant and allows us to assume that the masses of the two heavy particles are the same. This means that the main difference between models such as the LFDM model and the decay charged

particle model is that whereas the initial conditions (density and velocity perturbations) in the former case arise from massless neutrino, they are inherited from the baryon-photon fluid in the latter case. This results in a qualitative difference between the two cases as seen in Figure 2.1. While density and velocity perturbations of massless neutrinos decay after horizon entry, these perturbations oscillate with nearly constant amplitude for the photon-baryon fluid after horizon entry for $\eta < \eta_{\rm decay}$.

It is seen in Figure 2.1 that the matter power spectrum, in this case, oscillates for scales that are sub-horizon during the pre-decay phase but its value can exceed the matter power spectrum for the ΛCDM model for the same cosmological parameters.

This can be understood as follows. In the ΛCDM model, the density perturbations of the CDM component, in Synchronous gauge, $\delta_{\rm cdm} = -h/2$ or they are completely determined by metric perturbations and are independent of velocity perturbations which are zero at all times, $\theta_{\rm cdm} = 0$. In this case, the CDM density perturbations at sub-horizon scales grow logarithmically during the radiation-dominated era. However, in the decaying charged particle model, the initial velocity perturbations of the CDM component (the post-decay neutral particle) are derived from the photon-baryon fluid and constitute an additional source of density perturbations. For wavenumbers at which the velocity perturbations of the initial conditions combine in phase with density perturbations of the CDM component, the density perturbations can overshoot perturbations in the ΛCDM model. On the other hand, this effect also serves to increase the decrement as compared to the ΛCDM model for wavenumbers at which velocity perturbations act to suppress the growth of density perturbations.

To generate the power spectrum and transfer function in the CHDM regime we have modified the codes as follows:

$$\begin{aligned} \dot{\delta}_{\rm chdm} &= \dot{\delta}_b \\ \dot{\theta}_{\rm chdm} &= \dot{\theta}_b \quad \text{For } z \leq z_{\rm decay} \end{aligned} \tag{2.11}$$

$$\begin{aligned} \dot{\delta}_{\rm chdm} &= \dot{\delta}_c \\ \dot{\theta}_{\rm chdm} &= \dot{\theta}_c \quad \text{For } z > z_{\rm decay} \end{aligned} \tag{2.12}$$

2.4 Evolution of Transfer Functions of Different Dark Matter Candidates

In this section, we briefly describe how the dark matter transfer function evolves for different dark matter candidates considered in this work. The transfer functions are given in Figure 2.2 at $z = 10^4$, 10^5, 2×10^6 and 10^7. The model specifications are identical to that used in Figure 2.1.

WDM: In this work, we have considered keV-mass thermally produced WDM candidates, which become non-relativistic at $z \sim 10^6$–10^7. So in the very early universe, when they are still relativistic, the transfer function at sub-horizon scales will be similar to that of a relativistic particle like the massless neutrino. As time progresses they become non-relativistic but still cause suppression as compared to the ΛCDM model at small scales owing to their free-streaming velocity that decays at a slower pace, as $1/a$. We have shown the evolution of transfer functions for WDM with of mass 0.33 keV in Figure 2.2, which is relativistic until $z \simeq 1.4 \times 10^6$, so the sub-horizon features at $z = 10^7$ and $z = 2 \times 10^6$ are essentially the same. WDM with higher masses become non-relativistic earlier, before the onset of the μ-distortion era (discussed in the next section).

ULADM: The ULADM forms due to spontaneous symmetry breaking in the early universe and behaves like a coherent scalar field. Once the mass of the field drops below the Hubble constant, the field starts oscillating coherently around the true minima of the potential and behaves like cold dark matter. We have plotted the evolution of transfer function for $m_a = 10^{-24}\,\mathrm{eV}$. ULADM with this mass decouples from the Hubble drag at $z \simeq 2 \times 10^4$ and the suppression occurs at scales smaller than $k \simeq 0.3\,\mathrm{hMpc}^{-1}$.

LFDM: As mentioned in Section 2.1, LFDM is formed due to phase transition in the neutrino sector and gets its initial conditions from the massless neutrino. In Figure 2.2, we show the evolution of the transfer function for $z_f = 10^5$. We notice that the transfer functions of LFDM and the WDM with mass 0.33 keV are identical at $z = 10^6$ and 10^7 because at high redshifts both behave like massless neutrinos. At $z = 10^5$, the WDM has already become non-relativistic but LFDM continues to be relativistic which explains greater suppression in

the LFDM power spectrum. After $z = z_f$, the LFDM behaves as CDM, but WDM continues to cause suppression of power at small scales owing to its slowly decaying but still significant free-streaming velocities. At more recent time, i.e., $z = 10^4$, the LFDM transfer function is identical to that of CDM at scales $k \gtrsim 0.3\text{hMpc}^{-1}$, the scale that enters the horizon at the formation redshift, but smaller scales still carry the massless neutrino-like features.

CHDM: This model is qualitatively different from the other models as the dark matter candidate, in this case, is charged and coupled to the photon-baryon plasma at early times. The time evolution of CHDM transfer function is identical to that of baryons at high redshifts with $R = 3(\rho_b + \rho_{\text{dm}})/(4\rho_\gamma)$ as explained in subsection 2.3. At lower redshifts and at scales larger than the scale that entered the horizon at $z_{\text{decay}} = 10^5$, its transfer function is identical to CDM. At smaller scales, the transfer function can exceed the matter power of the ΛCDM model.

The small-scale power suppression can have its distinct imprints on various universal observables. The rest of the thesis is devoted to exploring some of those effects. In the next chapter, we study the effects of LFDM on linear matter power spectrum in more detail. We also perform a χ^2 analysis with observational data to constrain the model parameters. In the later two chapters, we extend our study to the EoR and the spectral distortion in the CMB, both being sensitive to the nature of power spectrum.

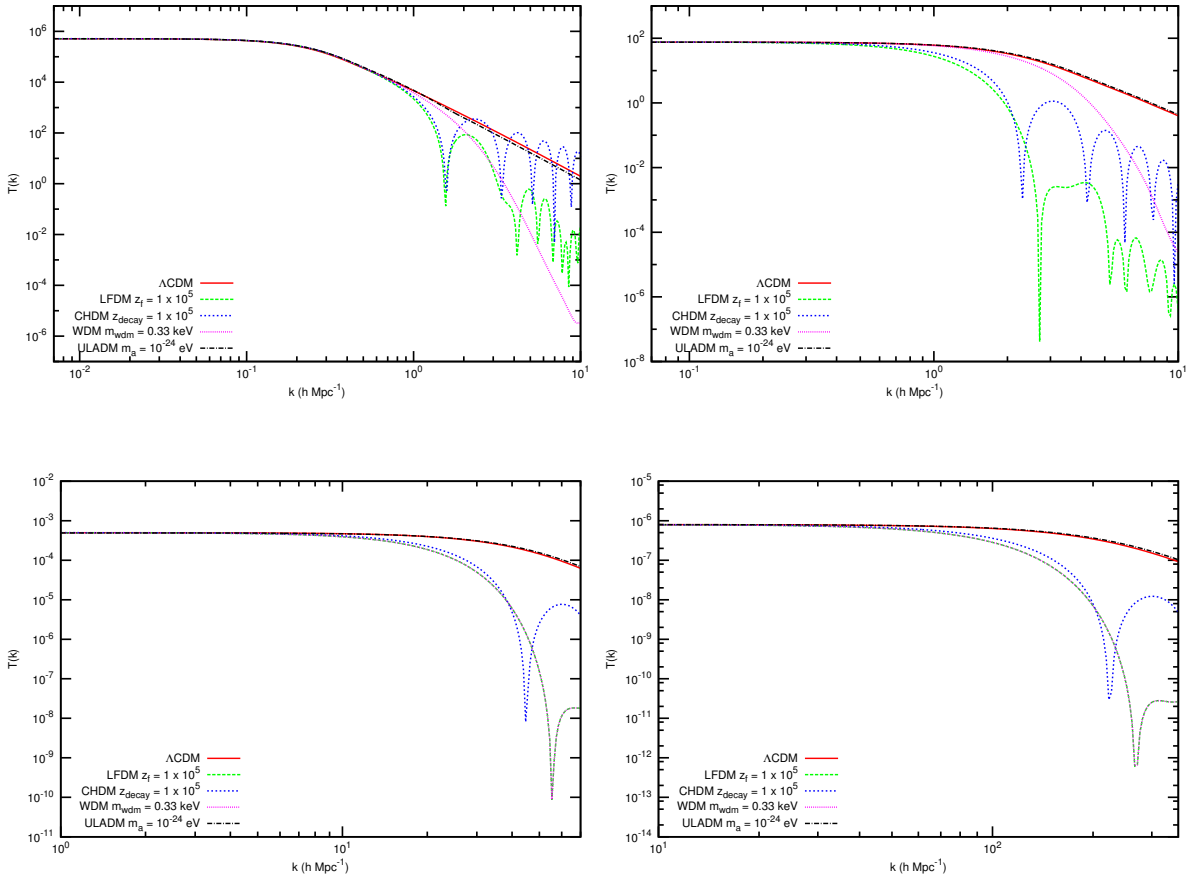

Figure 2.2: The evolution of transfer functions of four dark matter candidates considered in this work along with ΛCDM. Clockwise from top-left, transfer functions are plotted at $z = 10^4$, 10^5, 2×10^6 and 10^7. For each of the non-standard dark matter candidate, the parameters are chosen such that the power is cut at nearly the same scale $k \simeq 0.3h\text{Mpc}^{-1}$. The specifications of the models are mentioned in the legends.

Chapter 3

Scanning the Models: Power Spectrum Analysis of LFDM

In this chapter we provide a detailed power spectrum analysis of one of the alternative dark matter candidate discussed in the previous chapter, namely the LFDM. There are two model parameters of interest: the effective massless neutrino degrees of freedom $N_{\rm eff}$ and the redshift of formation z_f. We consider two different scenarios; entire dark matter of the universe consists of LFDM and and a fraction $f_{\rm lfdm}$ of total dark matter is LFDM. We have computed a series of power spectra varying these parameters with publicly available code `CAMB` and compared them with data by performing a χ^2 analysis. An interesting result found is that a small (30%) fraction of LFDM agrees better with data at small scales, than the standard ΛCDM model.

This chapter is based on the work presented in [4]. The Chapter layout is as follows. In Section 3.1 we describe how the `CAMB` code was modified to get the desired power spectra. In Section 3.2, we have described the datasets we used at different scales of the power spectrum. We discuss the data analysis procedure and showed the results in Section 3.3. We also briedfly describe how the code can be modified for WDM and CHDM models at the end of this section. Finally, we conclude in Section 3.4.

3.1 Modification in `CAMB`

We have discussed two different LFDM candidates in the last chapter; the scalar LFDM and the Fermionic LFDM. It is interesting to note that even though the physics of scalar and fermionic

LFDM production can be quite different, the initial condition of the LFDM at the formation epoch can be taken from the a neutrino-like component at the epoch corresponding to $z = z_f$. This is because in both the cases, the density perturbation of a neutrino or a dark radiation component provides the initial density fluctuation of LFDM at the production epoch z_f. The evolution of neutrino density perturbation is obtained by solving a series of coupled differential equations [44] involving Legendre Polynomials

$$\begin{aligned}
\dot{\delta} &= -\frac{4}{3}\theta - \frac{2}{3}\dot{h} \\
\dot{\theta} &= k^2\left(\frac{\delta}{4} - \sigma\right) \\
2\dot{\sigma} &= \frac{8}{15}\theta - \frac{3}{15}kF_3 + \frac{4}{15}\dot{h} + \frac{8}{5}\dot{\eta} \\
\dot{F}_l &= \frac{k}{2l+1}\left(lF_{l-1} - (l+1)F_{l+1}\right)
\end{aligned} \tag{3.1}$$

The solution for δ_ν is an exponentially damped oscillation at sub-horizon scales [44]. Physically, it represents the free-streaming effects of highly relativistic neutrinos. In Figure 3.1, we plot linear matter power spectra for standard model neutrino density fluctuation by solving the above equations using the publicly available code `CAMB` [43] for two different values of z_f. Our main modification in `CAMB` is to evolve it up to a redshift z_f without CDM and extract the transfer function for neutrino perturbation at $z = z_f$, $\delta_\nu(z_f)$, and use that for the LFDM initial condition for density fluctuation at the epoch of its formation. We then evolve LFDM perturbation just like CDM to get the power spectra at the present epoch. So the oscillations at small scales in the final power spectra at $z = 0$ is a signature of the fact that LFDM obtained its initial density fluctuation from neutrino perturbation at z_f which was damped and oscillatory at scales smaller than the horizon size of the Universe at $z = z_f$.

The main goal of our work is to find out how late the dark matter can form, i.e, to find out the minimum value of the formation redshift z_f. As discussed in the previous section, the formation of dark matter happens via the transition of the scalar field. We are therefore able to formulate the cosmological impact of LFDM in terms of three parameters: the initial relativistic neutrino degrees of freedom: $N_{\rm eff}$, the epoch of the formation of CDM: z_f, and the fraction of CDM that forms at $z = z_f$: $f_{\rm lfdm}$.

As Figure 3.1 shows, the new features introduced by LFDM are largely determined by the variation of z_f. The scale imprinted on the matter power spectrum is determined by the scale

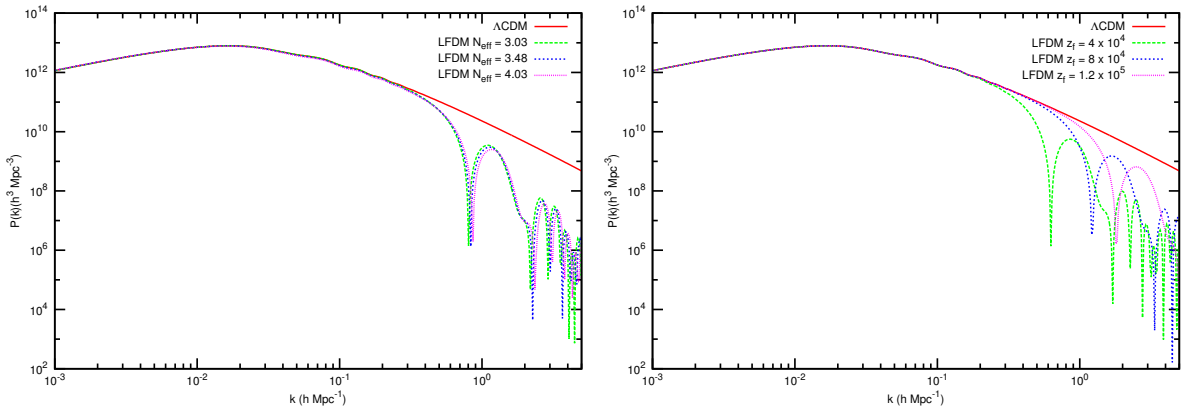

Figure 3.1: The LFDM power spectra (unnormalized) are shown for a range of formation redshift z_f and relativistic neutrino degrees of freedom. The left panel shows the impact of changing $N_{\rm eff}$ for a fixed $z_f = 52000$. In the right panel, LFDM power spectra are shown for different z_f for $N_{\rm eff} = 3.04$.

of horizon entry at $z = z_f$, k_e. For the horizon entry in the radiation dominated era:

$$k_e = \frac{H_0}{c}(1+z_f)\Omega_\gamma(1+0.227N_{\rm eff}) \tag{3.2}$$

Here Ω_γ is the radiation contribution from photons. The matter power spectrum is suppressed at scales below the corresponding scale for k_e. This suppression can be understood as follows: the LFDM obtains its initial conditions from massless neutrinos. On the super horizon scales, the massless neutrinos behave like other forms of matter such as the CDM (for details see e.g. [44, 150]). However, unlike CDM, the perturbations in this component are washed out owing to free-streaming on scales smaller than horizon size. As z_f is increased the feature shifts to larger k_e, or smaller scales. As z_f tends to infinity, the LFDM matter spectrum approaches the ΛCDM results. This also motivates our choice of the cosmological data for constraining the LFDM model.

3.2 The Data

As discussed above, we can theoretically analyze the impact of the LFDM in terms of three parameters: z_f, $f_{\rm lfdm}$ and $N_{\rm eff}$. For a given z_f and $f_{\rm lfdm}$, $\Delta N_{\rm eff}$ can be expressed in terms of

these parameters for a given $\Omega_{\rm dm}h^2$ (Eq. (2.5)), which we assume to be fixed and given by the best-fit Planck estimate for the six-parameter spatially-flat ΛCDM model [55].

The two parameters—z_f and $N_{\rm eff}$—affect the linear power spectrum at different scales. The main impact of changing $N_{\rm eff}$ is to alter the MRE epoch. This shifts the peak of the matter power spectrum. As the SDSS data on the galaxy power spectrum gives the power at such scales: k=0.02–0.1 h/Mpc, this data is sensitive to the variation of of $N_{\rm eff}$. We use the SDSS DR7 release data [5]. For $k > 0.1$, the SDSS data cannot be directly compared to the predictions of linear theory as non-linearities set in for such scales. We use the HALOFIT model embedded in `CAMB` to obtain the non-linear power spectrum for comparison with the SDSS galaxy power spectrum; this procedure allows us to use the data for $k \lesssim 0.2$. It is instructive to note that though the HALOFIT works mainly for ΛCDM and might not work for other dark energy models of constant equation of state differing from $w = -1$ [151], in LFDM cosmology, the background evolution is exactly same as the ΛCDM model after the phase transition has occurred deep in radiation dominated era. So we expect HALOFIT to be a good approximation for mildly non-linear power spectra for comparison with SDSS galaxy power spectrum.

As seen in Figure 3.1 above, the main effect of late formation redshifts z_f is to suppress the power at scales $k > 0.1\,$h/Mpc. Such scales are not directly accessible from the data on galaxy power spectrum at low redshifts. It is known that Lyman-α clouds observable at intermediate redshifts ($2 < z < 5$) probe mild over densities ($\delta \simeq 10$) of the density field. The data from Lyman-α clouds can be used to reconstruct the linear matter power spectrum for scales comparable to the Jeans' scale of the intergalactic medium in the relevant redshift range [6, 152]. Here we use the data in the range: $0.2 < k < 4.8\,$h/Mpc from [6, 7]. From Figure 3.1, it is clear that the scales probed by the Lyman-α data are far more sensitive to the variation in z_f. As z_f is increased the oscillations seen in the power spectra move to larger values of k (or smaller scales) with the power spectrum approaching the ΛCDM model as z_f tends to very large values.

Other data sets at scales overlapping with SDSS data are available, e.g. WiggleZ survey [153] with scale coverage $0.01 < k < 0.5\,{\rm h\,Mpc^{-1}}$. We could obtain supplementary information from WiggleZ data but it doesn't expand the range of scale we already consider. Or the two data sets we use allow us to obtain the tightest possible constraints on LFDM models within the

framework of linear (and mildly non-linear) theory. Cosmological weak lensing provides a powerful probe of the matter power spectrum (e.g. [154]). We do not use it here because the scales probed by the cosmological lensing are larger than the those probed by the Lyman-α data (e.g. [7]) so we cannot use it to get better constraints on the formation redshift z_f. Also in this chapter we only consider the available data on measured or reconstructed power spectra. The reconstructed power spectrum is not readily available in the literature (e.g. [154]). This means we have to compute the observables presented in the literature from LFDM power spectra. We shall undertake this task in future works.

Our choice of Lyman-α data is also governed by the availability of reconstructed linear power spectra. In all the available data on the linear matter power spectrum, the data we use provides a probe of the smallest scales. It is based on the high spectral resolution QSO spectra (total of 53 QSOs including 30 observed at high spectral resolution [6]). This one-dimensional data allows reconstruction of the linear 3-dimensional matter spectrum. However the low-resolution SDSS data, which is available for a much larger number of QSOs, doesn't allow this reconstruction (for details and discussion see e.g. [6, 155]). This means that a comparison with the ongoing survey SDSS-III/BOSS, which will finally obtain spectra of 160000 QSOs in the redshift range $2 < z < 7.5$ [156], will require us to simulate the Lyman-α spectra for our class of models. We consider it beyond the scope of this work and plan to undertake this study in the near future. We also note that even the low spectral resolution Lyman-α could be a powerful probe of the matter power spectrum at small scales because of two reasons: (a) the measured 1-dimensional flux power spectrum by the Lyman-α data receives contribution from a wide range of scales of the 3-dimensional power spectrum, (b) the relation between the density field and the observable is non-linear (e.g. [157]).

3.3 Data Analysis and Results

The two data sets—SDSS galaxy power spectrum and the linear power spectrum reconstructed from the Lyman-α data—allow us to investigate the range of scale: $k = 0.02$–$5h/Mpc$. However, these two data sets do not have the same bias with respect to the underlying density field, and therefore the overall normalization constant is different for the two cases. In other words, we can probe the shape of the power spectrum in the aforementioned range of scales and not its

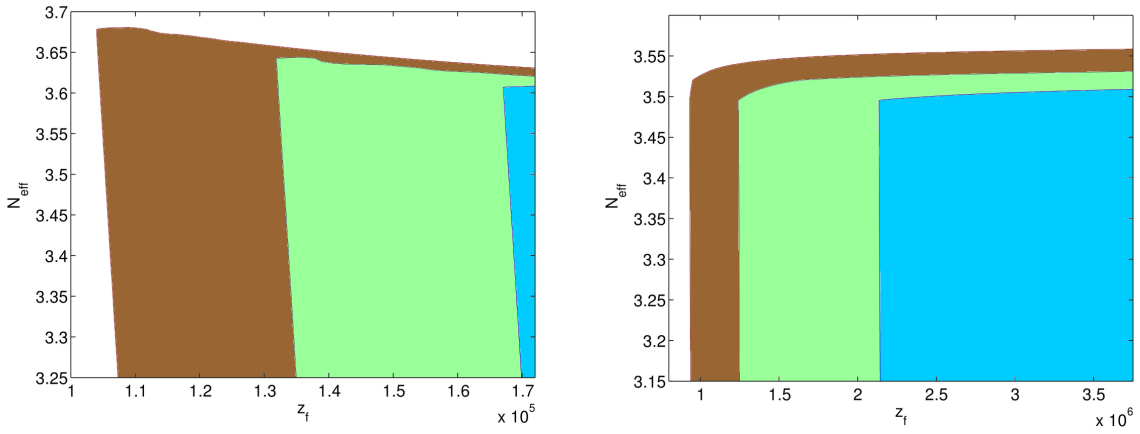

Figure 3.2: The allowed regions in the z_f–$N_{\rm eff}$ plane are shown from the power spectra of SDSS (Left Panel) and Lyman-α (Right Panel) data. In each Panel, the blue, green and the brown regions indicate the 68%, 95.4% and 99.73% confidence levels, respectively.

overall normalization. We consider four parameters for each data set: $N_{\rm eff}$, z_f, $f_{\rm lfdm}$, and C, where C corresponds to an overall normalization which is marginalized. For our analysis we search the best-fit in the range: $N_{\rm eff} = 3$–4, which encompasses the current range of constraints on $N_{\rm eff}$ [140, 141].

As noted above we compute a suite of models for different z_f and $N_{\rm eff}$ by modifying `CAMB`. We extract unnormalized power spectra and the normalization is fixed by comparison with data. Model predictions for a range of $f_{\rm lfdm}$ are obtained by assigning different weights to the initial conditions; for instance, for $f_{\rm lfdm} = 1$, the initial condition for the CDM component is drawn from massless neutrinos at $z = z_f$. For a smaller value of $f_{\rm lfdm}$, the initial conditions are a mix of the CDM component in the pre-transition phase and the massless neutrino. This also means that we need to vary only two parameters (z_f and $N_{\rm eff}$) in CAMB for obtaining the power spectra for all the four parameters. For likelihood analysis we have used the range of z_f to be 24000–180000 with an interval of $\Delta z_f = 4000$ while analyzing the SDSS data and $z_f = 62000$–4000000 with an interval of $\Delta z_f = 2000$ for the Lyman-α data. The range of the z_f is different for the two data-sets because the Lyman-α data covers much smaller scales as compared to the SDSS data. The smallest scale probed by the Lyman-α data, $k \simeq 4\,{\rm Mpc}^{-1}$ enters the horizon at $z \simeq 4000000$ which is the highest z_f we have considered. Similarly, $N_{\rm eff}$

is also finely sampled to ensure convergence of the likelihood procedure.

We use 45 band-powers from the SDSS galaxy data and 12 points from the reconstructed linear power spectrum from the Lyman-α data. The best-fit χ^2 for the two case is 65 and 10.5, respectively. The multi-parameter contours and posterior probabilities are computed by marginalization, i.e. the integration of the likelihood function $\exp(-\chi^2/2)$ over redundant parameters.

We first consider the case $f_{\rm lfdm} = 1$, or all the observed CDM at the present is formed at z_f. In Figure 3.2, we show the confidence limits for z_f and $N_{\rm eff}$ for the two data sets. Both the data sets result in a lower limit on the value of z_f. The Lyman-α data results in stronger constraints on z_f. This result follows from Eq. (2.5) and Figure 3.1 which show that an increase in z_f results in the feature in the power spectrum shifting to smaller scales. As Lyman-α data probe smaller scales, we expect a tighter constraint on z_f from these observations. We note that for both the data sets the floor on the value of χ^2 is set by the ΛCDM model. Or we do not find any evidence of an improvement over the ΛCDM model within the framework of a two-parameter LFDM model.

The marginalized posterior probabilities for z_f are shown in Figure 3.3. We note that the temperature of the universe corresponding to $z = z_f$ from the two data sets is in the range 30–500 eV. These lower limits on the transition temperature are far below the constraints on production redshifts in the WDM models; in such models a dark matter particle with mass $m > 1\,\mathrm{keV}$ is invoked [129] and the production redshift lies before the epoch of BBN at a temperature $T \simeq$ MeV.

We next consider the case $f_{\rm lfdm} < 1$. Or only a fraction of the CDM observed at the present originated at $z = z_f$. This expands the parameter space under consideration and yields more interesting results. In Figure 3.4, we show z_f–$f_{\rm lfdm}$ contour plots after marginalizing over $N_{\rm eff}$ and the overall normalization C. The SDSS data gives results similar to the previous case with slightly looser bound on z_f. The Lyman-α data, on the other hand, results in very different outcome, as compared to the earlier case. The z_f–$f_{\rm lfdm}$ plain splits into two separate regions in this case. The region corresponding to $z_f < 10^5$ is ruled out by the SDSS data but is unconstrained by the Lyman-α data. This underlines the importance of using two data sets at different scales for our analysis. Larger values of z_f is allowed by both the data sets. Further, the Lyman-α data results in a better fit as compared to the ΛCDM case, as seen in Figure 3.5,

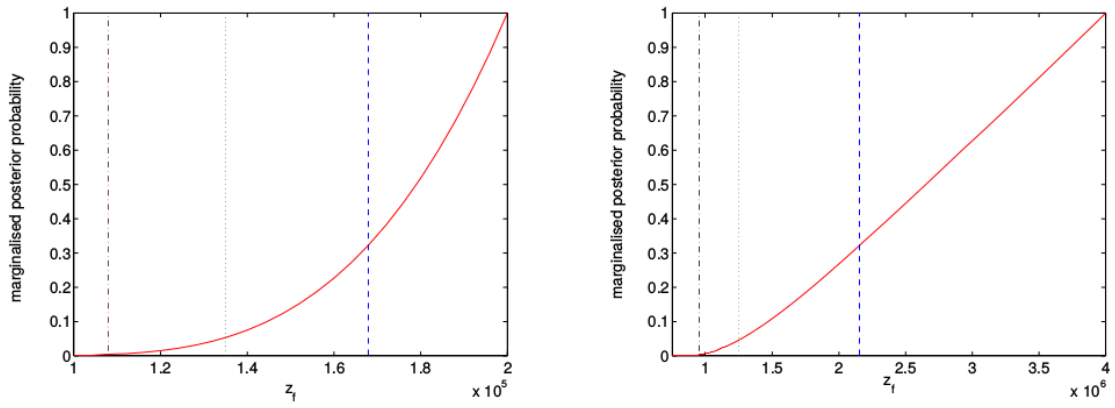

Figure 3.3: Marginalized posterior probability for z_f from SDSS data (Left Panel) and Lyman-α data (Right Panel) are shown. The dashed (blue), dotted (green) and dot-dashed (brown) lines indicate the 68%, 95.4% and 99.73% regions, respectively.

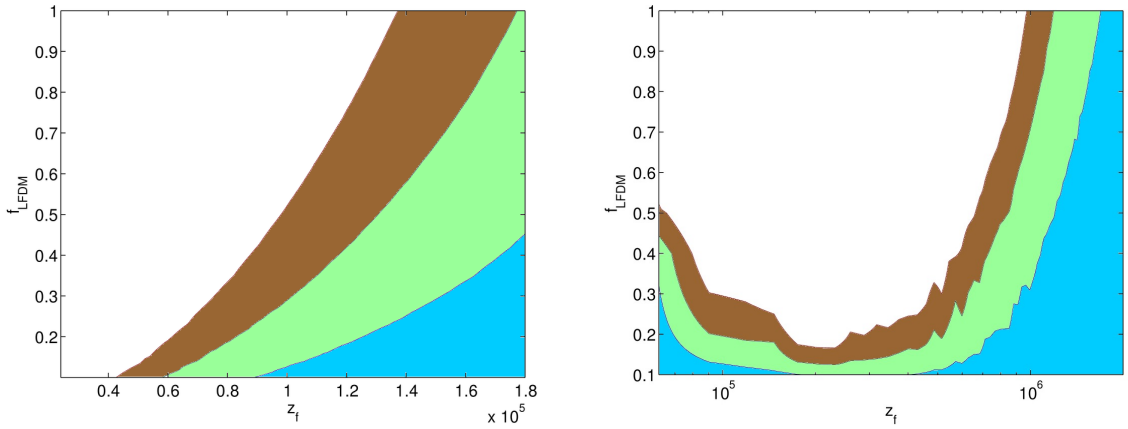

Figure 3.4: Contours of z_f and $f_{\rm lfdm}$ obtained using SDSS data (Left Panel) and the Lyman-α data (Right Panel).

for a large range of values of $f_{\rm lfdm}$ (this inference is nearly independent of $N_{\rm eff}$). In particular, $f_{\rm lfdm} = 0.1$ results in a better fit for the entire range of z_f. While $\chi^2 \simeq 11$ for the ΛCDM models, it reduces to 3.5 for many models for $f_{\rm lfdm} = 0.1$. This improvement is largely owing to the two data points for the largest k. This shows the importance of using the small scale data for unraveling the nature of LFDM models.

Our analysis clearly shows that LFDM models with a non-zero $f_{\rm lfdm}$ provide a better fit to the data. However, while significant, our results need further explanation. In our analysis we assume many cosmological parameters to be fixed to their Planck best-fit values. Within the framework of spatially-flat ΛCDM model, the relevant cosmological parameters—$\Omega_{\rm dm}h^2$, $\Omega_B h^2$, h, n_s—have been estimated at unprecedented precision [55]. For a given angular scale ℓ, the CMBR anisotropies receive dominant contribution from three-dimensional scales k such that $\ell \simeq k\eta_0$; $\eta_0 = 13670\,{\rm Mpc}$ for the best-fit Planck parameters. As Planck measures CMBR anisotropies for $\ell < 2000$, the smallest scale to make significant contribution to these observations is $k \simeq 0.15\,{\rm Mpc}^{-1}$, which lie in the range of scales probed by SDSS; Planck results are compatible with the SDSS DR7 data we use in this chapter (Figure 20 of [55]). However, these scales are larger than the scales involved in Lyman-α measurements and therefore the Lyman-α data gives us independent information of the matter power spectrum on scales not probed by Planck. This also means that we are justified in assuming priors on cosmological parameters from Planck, even though we still need to explore the whole range of parameters allowed by Planck to put our result on a firmer footing.

3.4 Conclusion

In this work we have investigated the epoch of dark matter formation in the universe for a class of non-WIMP dark matter scenarios. Especially we have studied how late the dark matter can form. Unlike the case of electroweak WIMP where dark matter formation happens through thermal freeze-out at a temp $T \simeq$ GeV, in our models the dark matter formation happens considerably after BBN but before the decoupling. Our study is mainly inspired by a few viable models of "LFDM" [1, 3]. In such models the matter power is suppressed at small scales which can be probed by cosmological observables at low redshifts using the available data on the linear power spectrum.

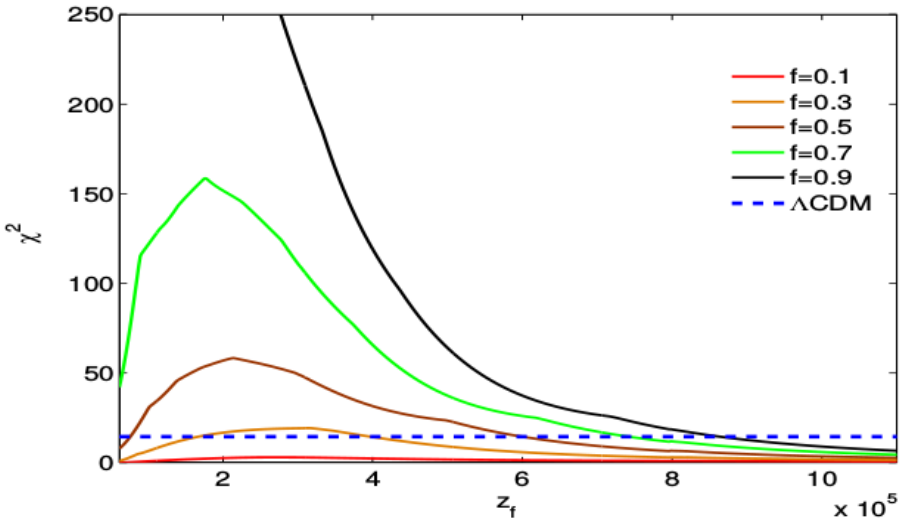

Figure 3.5: χ^2 is plotted as a function of z_f for many different values of $f_{\rm lfdm}$ for the Lyman-α data. The dotted horizontal line is the χ^2 for the ΛCDM model.

In the present study we confront models of LFDM with the existing SDSS data on galaxy power spectrum and the linear power spectrum extracted from Lyman-α data for $z > 2$. Our results can be summarized as follows: (a) if all the presently observed CDM is late forming then both the data sets result in upper limits on the redshift of formation of LFDM, with Lyman-α data resulting in tighter bounds: $z_f < 3 \times 10^6$ (99% confidence limit) (Figure 3.2), (b) if we allow only a fraction of the CDM to form at late times, then we improve the quality of fit as compared to the ΛCDM model for the Lyman-α data. This is suggestive that the present data allows for a fraction of the CDM to form at $z_f \simeq 10^5$ (Figure 3.4). In particular our result underlines the importance of the Lyman-α data for our study.

In the recent past, the quantity of Lyman-α data available has sharply increased with the ongoing survey SDSS-III/ [156]; and the results from this survey are expected to throw further light on the models of LFDM. We hope to return to this issue with as the new data becomes available. Another interesting study could be the effect of LFDM on the epoch of the formation of the first stars, which we will explore in the next chapter.

Chapter 4

Observational signatures I: EoR and the High Redshift Universe

In the previous chapter, the effects of one alternative dark matter candidate on the small-scale matter power spectrum have been discussed. It was found that along with decreasing power at small scales; it also induces damped oscillations at scales smaller than that. The next two chapters of this thesis are devoted to describing the consequences of modification of small-scale power on different milestones of the universe. In this part of the thesis, we consider the effects of alternative dark matter candidates on the Epoch of Reionization(EoR). This epoch is considered a milestone in the history of the universe as it marks the time when the universe goes back to its original ionized state, preceded by a temporary neutral state. The ionization process, described in detail in the following section takes place by the high energy photons coming out of the first stars and galaxies. Despite being such an important epoch, it is one of the least understood universal phenomena. Recently a lot of theoretical and experimental efforts are put to model and detect the EoR. The modification of small-scale power will change the population of dark matter halos that will host the sources of reionization, resulting in a different source distribution, which in turn can alter the topology of reionization and even the duration of it. At present, there are many models of reionization with different star formation efficiency, photon escape fraction, clumpiness of the IGM, etc. In our study, to avoid degeneracies of reionization parameters we consider one particular scenario where the fraction of neutral hydrogen, $\bar{x}_{\rm HI}$, is equal to 0.5 at $z = 8$.

Along with this, we also cover how the evolution of collapsed fraction of neutral hydrogen in the high-redshift universe is affected due to small-scale power modification. A significant portion of collapsed neutral hydrogen is located in clouds with high column density. These systems cause a large absorption dip in the spectrum of quasar that is located behind the cloud, thus making them easier to detect. These high column density clouds having $N_{\rm Hi} \geq 2 \times 10^{20}\, 10^{-20}$ are called Damped Lyman-α(DLA) systems. Due to the modification of small-scale power, the mass functions of host haloes will be changed at low mass, which can potentially change the neutral hydrogen gas density at all redshifts. With a lot of new quasars discovered recently with brand new Lyman-α spectra at high redshifts, the collapsed fraction of neutral hydrogen in DLAs has been measured with great accuracy. This provides an excellent opportunity to constrain the modification of small-scale power due to alternative dark matter candidates, and thus the properties of dark matter.

The chapter is organized as follows. In Section 4.1, a physical description of the EoR is provided. In Section 4.2, the simulation technique of the radiation field is discussed. The results are provided in Section 4.3. In Section 4.4 the effects of alternative dark matter candidates on the evolution of cosmological gas density are considered and Section 4.5 is reserved for discussion. This chapter is based on the work presented in [8].

4.1 Physics of The EoR

The EoR is fueled by the old low-metallicity population-III stars and black holes hosted by the first galaxies. These sources, with their high-energy photons, ionized the neutral medium surrounding as well as the IGM and that highly ionized state is maintained till today. Till the reionization started, the dark component played the dominating role in structure formation and evolution while during and after the re-ionization, baryonic matters also started being countable.

After the universe was almost 400 thousands years old, it was cold enough so that the electrons and protons can finally combine to form neutral hydrogen. This prolonged process is known as the recombination. After recombination, the baryons and photons decoupled from each other and the photons started free streaming. The following age till the beginning of reionization is known as the dark age. During this age, the universe was essentially neutral,

and it lasted for a long span of 400 million years.

After the first structures had formed, they started emitting radiation that initially ionized the medium immediately surrounding them. The ionized regions started expanding with time as the radiation started penetrating further into the IGM and got patched with each other to fill up the entire universe [158–161]. The binding energy of atomic hydrogen is 13.6 eV which means the ionising photons should lie in the ultraviolet regime or have higher energy. Hence, to make the ionization of the neutral IGM successful the sources should provide a sufficient number of high energy photons. The most obvious sources are the Population III stars. The Population III stars are much more massive than present day stars, therefore can be reservoirs of UV photons. The UV photons efficiently ionize the regions that encircle the stars. However, the lifespan of these old stars is also not very high either. Besides, their properties and number densities in the pre-reionization era are very poorly understood. In spite of these uncertainties, most of the studies of EoR revolves around the first stars (Please refer to [162] for a review). The mini-quasars hosted by black holes with mass $10^{3-6}M_{\odot}$ and AGNs also provide considerable amounts of UV photons. The contributions of mini-quasars [163–165] and AGNs [166–168] are well studied in literature , and it is found that the AGNs have little influence in ionising the universe [168], but it is still a matter of debate. On the other hand, the photon flux from the mini-quasars contain a lot of hard X-ray photons, as their spectral energy distribution follow a power law. These hard X-ray photons can also heat the IGM far beyond their ionization front. As the hard X-ray photons are not present in large abundance for the first stars, the can't heat the IGM to as broad extent as the mini-quasars [165].

In Figure 4.1, the time evolution of the fluctuation of the 21 cm brightness temperature, δT_b, is shown. In Section 4.2, we explain in detail that the distribution of δT_b is sensitive to the underlying neutral hydrogen density distribution. As seen clearly from Figure 4.1, as time proceeds δT_b becomes negligible in most of the regions implying that the universe is containing more ionized hydrogen.

The process of reionization is not instantaneous and estimated to lie between $z \simeq 6 - 12$. Different observational probes covering a broad range of length scales and epochs have confirmed the occurrence of EoR. The long list contains observations of the Lyman-α forest spectra of quasars up to $z \simeq 7$ [170–172], the optical depth of the Thomson scattering of the CMB photons [173–175] the temperature evolution of the IGM at $z \lesssim 6$ [176–178] etc. In recent

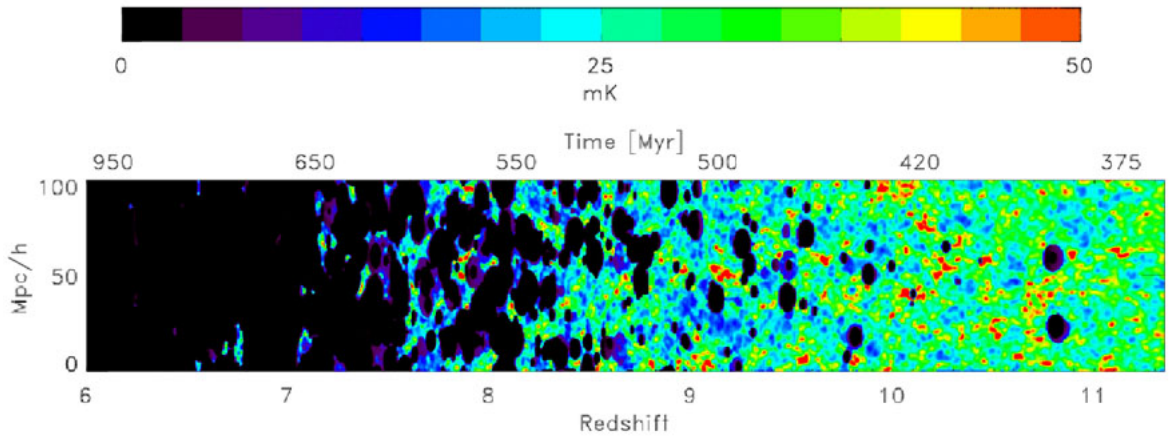

Figure 4.1: The evolution of 21 cm brightness temperature fluctuation. The picture is taken from [169].

time, the 21 cm line of atomic hydrogen has got more attention from the community as a probe of the IGM before and during reionization. This is a hyperfine transition line that arises due to the interaction of electron and photon spins. The 21 cm line corresponds to a forbidden transition between the triplet state of the hyperfine interaction to the singlet state with a very low transition rate. Despite having such a small transition rate, it is an essential astrophysical probe because of the huge amount of hydrogen [179, 180] in the universe and efficiency of collisions in establishing the population of the triplet state [181, 182]. Some major experiments among that will study the 21-cm line are The Low-Frequency Array (LOFAR), the Murchison Widefield Array (MWA), the Giant Meterwave Radio Telescope (GMRT) and the Square Kilometer Array (SKA).

Getting the complete picture of the reionization process is still a long way to go. There are quite a few obstacles in the way of understanding the physics of reionization, broadly divided into two classes: theoretical and observational. The efficiency of reionization depends crucially on the number density of the high energy photons coming from the first stars and the mini-quasars/AGNs. This brings the first two of the theoretical challenges; the first one is to correctly understand how the first stars form: what are the factors that controlled the formation of the first stars. As all the gas trapped into dark matter halo do not end up into star formation, it is difficult to correlate the population density of stars with the underlying dark matter density fluctuation map, even after assuming that the baryons mix up with dark matter homogeneously.

Therefore, it is also important to estimate how much of the gas trapped contributed in star formation, namely the star formation efficiency, correctly. Another essential unknown is the escape fraction of ionising photons, i.e., the fraction of high energy photons that can successfully escape the first galaxies to the IGM to ionize the medium. It is tough to constrain this quantity due to lack of observational data at such high redshift. Theoretical estimation of this parameter is also difficult though efforts have been made. Earlier studies used smooth galaxies, with isothermal and radially exponential disks at high redshift [183, 184] and later with more realistic disks [185] to calculate the escape fraction of the Lyman continuum photons. Despite using different analytical formalisms, all of these works yielded that a $\sim 10 - 30\%$ of Lyman continuum photons can escape the galaxies to ionize the medium [165]. Along with these two uncertainties the propagation of ionization front in the IGM and thus whether the high-density regions got ionized before the low-density regions, is also not clearly understood. All these challenges make this epoch a frontier in current research in cosmology.

The observational challenge is to model and clear the foregrounds that mask the true reionization signals and thus to extract and interpret the actual signal. The galactic and extragalactic foregrounds at different wavebands can be on the order of 10^3K while, as seen from Figure 4.1, the amplitude of reionization signal can be as small as mK. Along with the astrophysical foregrounds, the atmospheric and instrumental noises are also present in the observed spectrum, making it more difficult to measure this very faint but wealthy signal.

4.2 Simulating the Reionization Field

The redshift evolution of the mass averaged neutral fraction $\bar{x}_{\rm HI}$ during EoR is largely unknown. It is only constrained from the CMB anisotropy and polarization measurements [186] which allow us to infer the optical depth integrated through the reionization surface. Therefore, the CMB constraints can be satisfied for a wide range of ionization histories [187].

Our aim here is to study the HI signal from the reionization era for a class of LFDM and ULADM models and, if possible, discern generic features of such models from the HI power spectra. As mentioned earlier, given the uncertainty of reionization history, we do not assume a particular model for reionization history $\bar{x}_{\rm HI}(z)$. Instead we fix the redshift and the ionization fraction at which these models are compared. We take $z = 8$ and $\bar{x}_{\rm HI} = 0.5$ at this redshift for

our simulations.

Our method of constructing reionization fields consists of three steps: (i) generating the dark matter distribution at the desired redshift, (ii) identifying the location and mass of collapsed dark matter halos within the simulation box, (iii) generating the neutral hydrogen map using an excursion set formalism [188]. The assumption here is that the hydrogen exactly traces the dark matter field and the dark matter halos host the ionizing sources. The assumption that the dark matter follows the baryons is justified for simulating the HI signal from EoR for the following reasons. The issue of simulating and studying this signal is essentially a two-scale problem: the scale at which the structures collapse and the scale at which the HI signal is observable. These scales are generally separated by orders of magnitude. For instance, the objects that collapse around $z \simeq 10$ lie in the mass range $M \simeq 10^9$–$10^{10}\,\mathrm{M}_\odot$, which correspond to length scales $L \simeq 0.2$–$0.4\,\mathrm{Mpc}$ or equivalently $k \simeq 2\pi/L \simeq 30$–$15\,\mathrm{Mpc}^{-1}$. However, we study the HI signal in the range $0.1 < k < 4\,\mathrm{Mpc}^{-1}$. So even though the density field is highly non-linear at the scale of the collapse and therefore the assumption that baryons follow dark matter is not a good one, it generally is an excellent assumption at the scales at which the HI is probed, which lie in the range from mildly non-linear to highly linear at the redshifts of interest. We discuss our method in the following sections.

4.2.1 Generating the dark matter density field

We have used a particle-mesh N-body code [189] to simulate the $z = 8$ dark matter distribution. We use the linear power spectrum (Figure 2.1 in Chapter 3) to generate the initial Gaussian random density field at $z = 124$. For LFDM, the linear power spectra are generated using a modified version of `CAMB` [4] and `axionCAMB` is used for the ULA dark matter [145]. We have done simulations for the following models: ΛCDM, LFDM models with $z_f = \{2, 1, 0.7, 0.4\} \times 10^6$, and ULA models with $m_a = \{3.7, 2.5, 1.2, 0.26\} \times 10^{-22}$eV. Figures 4.2 shows the dimensionless matter power spectrum $\Delta^2(k) = k^3 P(k)/2\pi^2$ output from the N-body simulation at $z = 8$. Note the suppression of power on scales $k \gtrsim 1\,\mathrm{Mpc}^{-1}$ for both the LFDM (left panel) and ULA (right panel) models compared to the ΛCDM model. This suppression deepens as we decrease the value of z_f and m_a in the LFDM and ULA models respectively.

Our simulation volume is a $[150\,\mathrm{Mpc}]^3$ comoving box. We have run our simulation with a 2144^3 grid using 1072^3 dark matter particle. The spatial resolution is $0.07\,\mathrm{Mpc}$ which corre-

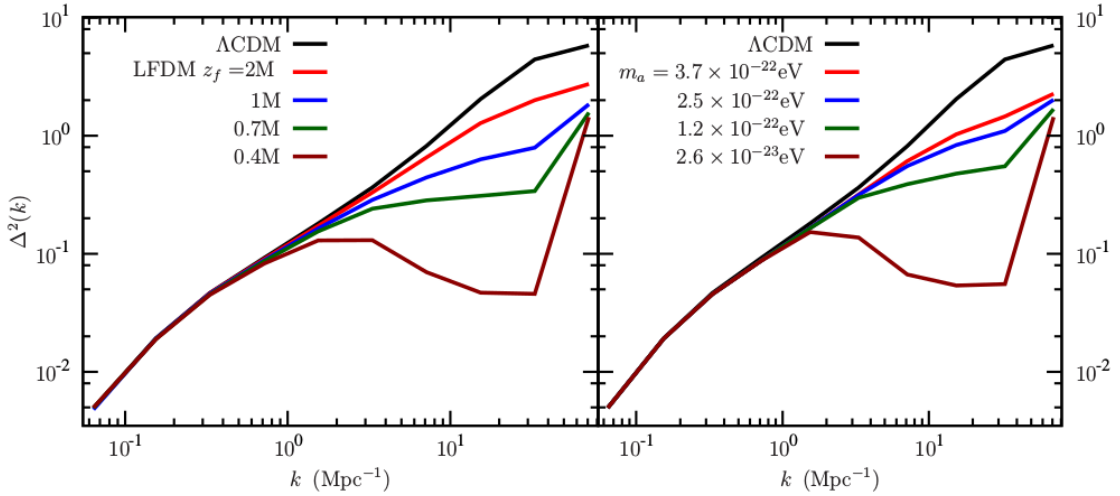

Figure 4.2: This shows the dimensionless matter power spectrum $\Delta^2(k)$ at $z = 8$ calculated from the N-body outputs using four different LFDM models (left panel) with $z_f = \{2, 1, 0.7, 0.4\} \times 10^6$ and four different axion dark matter models (right panel) with axion masses $m_a = \{3.7, 2.5, 1.2, 0.26\} \times 10^{-22}$eV. The black solid curves are the ΛCDM power spectrum.

sponds to a mass resolution of $1.09 \times 10^8\,\mathrm{M}_\odot$.

4.2.2 Identifying collapsed dark matter halos

We have used a friends-of-friends (FoF) halo finder code [190] to identify the location and mass of the collapsed dark matter halos from the outputs of the N-body simulation. We have used a fixed linking length 0.2 times the mean inter-particle separation and require a halo to have at least 10 dark matter particles which corresponds to a minimum halo mass of $1.09 \times 10^9\,\mathrm{M}_\odot$. Our choice of minimum halo mass is also fair because a halo mass of few times $10^8\,\mathrm{M}_\odot$ [191] (at $z = 8$) also corresponds to the virial temperature ($\sim 10^4$K) of hydrogen cooling threshold.

Figures 4.3 shows the simulated comoving number density of halos per unit logarithmic halo mass $\mathrm{d}n/\mathrm{d}(\ln M)$ as a function of the halo mass M at $z = 8$ for the range of LFDM (left panel) and ULA (right panel) models that we consider here. The solid curve is the theoretical ΛCDM mass function [192]. The simulated ΛCDM mass function, shown in black points, is in very good agreement with the theoretical mass function. Note that the low mass halo abundance is substantially reduced for both the LFDM and the ULA models as compared to the ΛCDM, and the suppression gets steeper with decreasing value of z_f and m_a in the LFDM and ULA

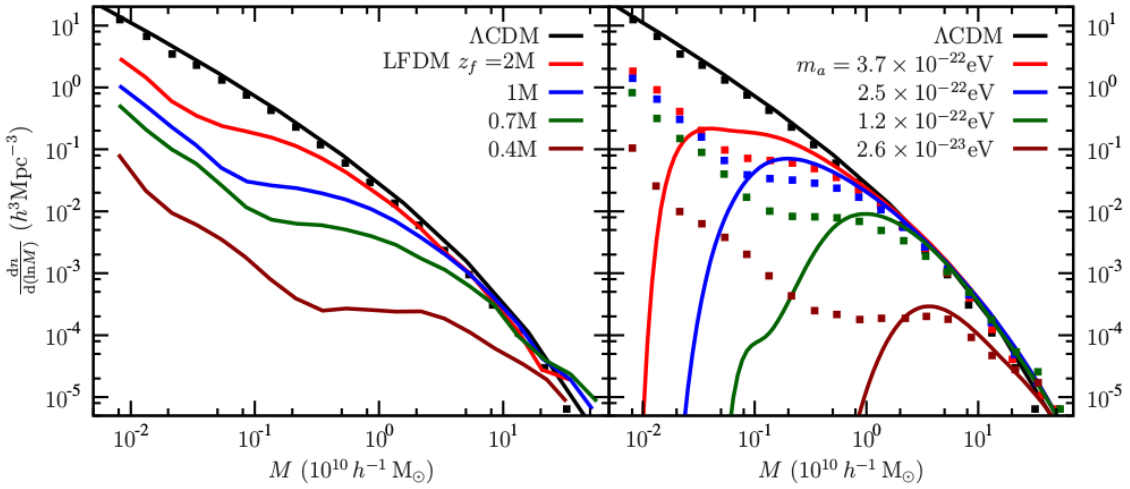

Figure 4.3: This shows the halo mass function from our simulations considering four different LFDM mode1ls (left panel) with $z_f = \{2, 1, 0.7, 0.4\} \times 10^6$ and four different axion dark matter models (right panel) with axion masses $m_a = \{3.7, 2.5, 1.2, 0.26\} \times 10^{-22}$ eV. The black solid curve is the theoretical ΛCDM mass function of Ref. [192]. In the right hand panel, the points represent the results of the simulation, while the solid curves are the theoretical prediction from [9].

models respectively.

In the right panel of Figure 4.3 , we also show the theoretical halo mass function for ULAs of Ref. [9]. The theoretical mass function displays a sharp cut-off at low halo masses caused by scale dependent growth and an increased barrier for collapse: consequences of the ULA Jeans scale. This cut-off is not present in the mass function found from our N-body simulations, but we should not expect it to be. N-body simulations treat ULAs as particles. However, this treatment is incomplete on small scales, where the coherent scalar field dynamics become important. The full scalar field dynamics have been computed by Ref. [193], and the validity of an N-body treatment on large scales was discussed in Ref. [194].The cut-off in the theoretical mass function for ULAs becomes relevant precisely where scale dependent growth and scalar field dynamics become important in linear theory. This suggests that the ULA mass functions we have derived should not be considered correct on these scales.

Both the LFDM and ULA mass functions produce low mass halos below the cut-off in the linear theory power spectrum. The same effect is observed in related simulations of WDM.

In the case of WDM, these low mass halos are believed, for a variety of reasons, to be "spurious" [195, 196]. We note that for ULAs the mass function slope from simulations increases below the cut-off in the theoretical mass function. An increase in the slope of the mass function is one method of identifying spurious halos, and it is interesting that these scales coincide. A complete simulation of ULAs (either as a scalar field [193], or an effective fluid [146]) should include a dynamical mechanism whereby the spurious halos never form, thanks to the so-called "quantum pressure" of the gradient energy. This further suggests, on theoretical grounds, that the low mass halos are spurious.

Spurious structure can be removed from simulated mass functions: for WDM in e.g. Ref. [197], for LFDM in Ref. [198], and for ULAs in Ref. [194]. In our results we do not remove the spurious structure. The constraints thus derived will be weaker than the true constraints, allowing for lighter ULAs and later formation of dark matter. Our constraints are therefore, in some sense, conservative.

4.2.3 Generating the neutral hydrogen maps

In the final step we generate the ionization map and the HI distribution using the homogeneous recombination scheme of Ref [199]. The basic assumption here is that the hydrogen exactly traces the matter density field and the halos host the sources of ionizing photons. It is also assumed that the number of ionizing photons emitted by a source N_γ is proportional to the mass of the host halo *i.e.* $N_\gamma = N_{\rm ion} M/m_p$ where m_p is the proton mass. The constant of proportionality $N_{\rm ion}$ here is the number of ionizing photons emitted per baryon in the collapsed halo times the ratio of the baryon density to the total matter density. The ionization map is generated by comparing the smoothed photon number density to the smoothed hydrogen number density at each grid point in the simulation volume. Any grid point where the photon number density exceeds the hydrogen number density is declared to be ionized. This comparison is carried out varying the smoothing radius from the cell size to a maximum smoothing length-scale which is half the box size. The ionized map and the HI distribution were generated using a grid spacing that is 8 times coarser than the N-body simulations. The simulated HI distribution was finally mapped to redshift space using the scheme outlined in Ref. [200]. We use the resulting HI distribution to calculate the brightness temperature fluctuation using [201]

$$\delta T_b = 4\text{mK}\ \frac{\rho_{\rm HI}}{\bar{\rho}_{\rm H}}(1+z)^2 \left(\frac{\Omega_b\, h^2}{0.02}\right)\left(\frac{0.7}{h}\right)\frac{H_0}{H(z)}\,, \tag{4.1}$$

where $\frac{\rho_{\rm HI}}{\bar{\rho}_{\rm H}}$ is the ratio of the neutral hydrogen to the mean hydrogen density. Throughout this chapter, we assume the spin temperature $T_s \gg T_{\rm CMB}$ or the HI is only observed in emission.

4.3 Results

Our method predicts an 'inside-out' ionization where the high density regions are ionized first and the low density region later. As the value of z_f in LFDM model decreases, the number of halos decreases. This means that the number of ionizing sources in the LFDM and ULA models is smaller as compared to ΛCDM model. To achieve the same ionization level at the same redshift ($\bar{x}_{\rm HI} = 0.5$), $N_{\rm ion}$ is higher in the LFDM models as compared to the ΛCDM model. We find that for $z_f < 0.4 \times 10^6$ the desired level of reionization doesn't occur as we couldn't form dark matter halos in our box. This allows us to put a rough limit of $z_f \sim 0.4 \times 10^6$ as a lower cut off. Similar considerations allows us to put a lower limit on the mass of ULA of $m_a > 2.6 \times 10^{-23}\,{\rm eV}$. It is instructive to note that this result is consistent with [145, 194] in connection to linear as well as non-linear observables of ULA dark matter. Table 4.1 lists lists the set of models we study in this chapter.

However, we could also get independent limit on z_f and m_a from constraints on plausible range of $N_{\rm ion}$. In our simulation $N_{\rm ion} = 24$ for the ΛCDM model. For the range of LFDM models we have studied (for decreasing z_f as shown in Figure 4.4): $N_{\rm ion} = \{47, 102, 212, 1230\}$. For ULA models, for decreasing m_a as shown in Figure 4.5, $N_{\rm ion} = \{61, 75, 134, 965\}$. Table 4.1 lists the values of $N_{\rm ion}$ for the models we consider.

How acceptable are these values if star-forming galaxies were responsible for the reionization process? For a metallicity $Z = 0.01$ and Scalo stellar mass function, the number of hydrogen ionizing photons is nearly 4000 per baryon which corresponds to $N_{\rm ion} \simeq 800$. Factoring in 10% star formation efficiency in a halo for star forming galaxies and 10% escape fraction from these haloes, this number drops by a factor of 100. [1]

It should be noted that all these factors— metallicity, initial mass function, star formation efficiency, and escape fraction—are highly uncertain. For zero metallicity (population III) stars

[1] We note that the effective number of hydrogen ionizing photons in the case of early QSOs where these photons are produced owing to the conversion of gravitational energy into energy are comparable to the case of early star-forming galaxies [158].

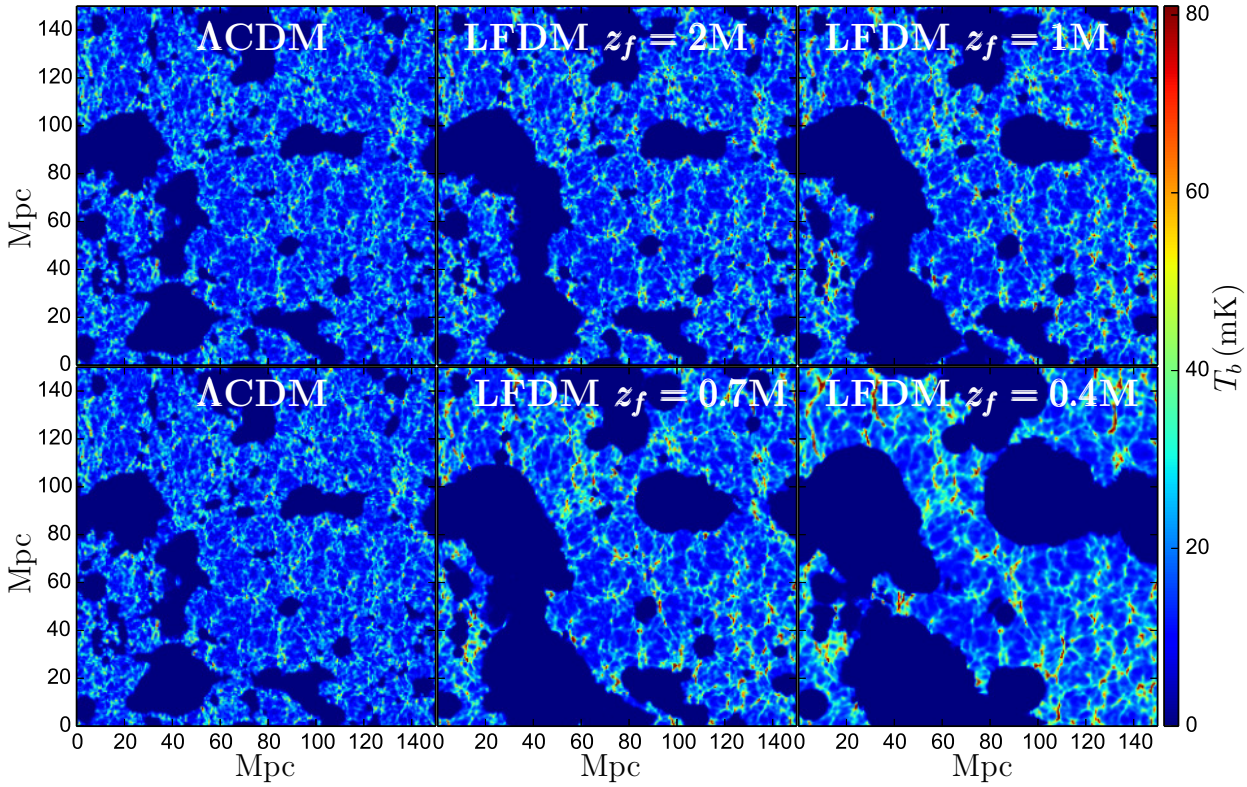

Figure 4.4: Two dimensional sections through the simulated brightness temperature maps of four LFDM models along the ΛCDM model for $\bar{x}_{\rm HI} = 0.5$. The ΛCDM (left) map has been shown twice. The direction of redshift space distortion is with respect to a distant observer located along the vertical axis.

the number of photons could be significantly higher and lie in the range 10^4–10^5 [2], but these stars last only a few million years which is considerably smaller than the age of the universe, $\simeq 5 \times 10^8$ yrs at $z \simeq 8$. These first metal-free, massive stars would have ended their life in supernova explosions thereby contaminating the interstellar medium with metals. This means the metal-free stars could only have dominated the reionization process for short periods. Also for initial stellar mass functions which have a larger fraction of massive O and B stars as compared to the Scalo mass function, the number of ionizing photons could be larger (for details of the physics of ionizing sources during the EoR see [158]).

[2] From current observations it is difficult to constrain the fraction of PopIII stars during the EoR but plausible bounds based on the observed Infra-red background and its fluctuations suggest PopIII stars might not have dominated the reionization process [202]

In light of these facts we could ask how plausible is $N_{\rm ion}$ corresponding to $z_f \simeq 0.4 \times 10^6$ or $m_a \simeq 2.6 \times 10^{-23}$ eV. In these cases, the required number of photons per baryon is larger than 5000. This is not possible to achieve for moderate metallicities and Scalo mass function even if the efficiency of star formation and the escape fraction are 100%. Therefore, we consider such models unrealistic.

Upcoming near-infrared telescope JWST will allow us to directly detect ionizing sources from the EoR (e.g. Figure 19 of [158]). For LFDM and ULA models, these sources are fewer in number and more luminous, which might allow a direct probe of the decrement of matter power spectra at small scales.

Figures 4.4 and 4.5 show two-dimensional sections through the simulated brightness temperature cubes for LFDM and ULA models for $\bar{x}_{\rm HI} = 0.5$. By visual comparison we see two main differences between ΛCDM and LFDM (ULA) models. The first difference is that the size of the ionized regions is larger in the LFDM (ULA) models. It is owing to two factors: first, as discussed above, it is a consequence of the fact that the sources require higher star formation efficiency to achieve the desired level of ionization. Second, the suppression of matter power at small scales results in a decrement of mass dispersion at these scales.

Therefore, the haloes that form are a higher σ fluctuations of the density field as compared to the ΛCDM model. It is known that higher σ fluctuations are more strongly clustered for a Gaussian field (see e.g. [203, 204]), or the ionizing sources are formed more preferentially in a cluster. Both these factors contribute to enlarging the size of the ionizing bubble and explain why the ionized bubble sizes get larger with decreasing value of z_f (m_a) in the LFDM (ULA) models. The second difference, also linked to the factors discussed above, is that the HI fields has stronger contrast in the LFDM models. Both these differences manifest themselves in the power spectra of the HI field which we discuss next.

Figures 4.6 shows the mean squared brightness temperature fluctuation $\Delta^2_{\rm b}(k) = k^3 P_{\rm b}(k)/2\pi^2$ of the HI field for LFDM (left panel) and ULA (right panel) models we consider here along with the ΛCDM model, for a fixed ionization fraction $\bar{x}_{\rm HI} = 0.5$. We find that the power for LFDM (ULA) models is greater than the ΛCDM model over a large range of scales $0.1 < k < 4\,{\rm Mpc}^{-1}$. This is owing to the factors discussed in the foregoing. The scale of the HI power spectra from ionization inhomogeneities, is governed by the size of ionized bubbles. These inhomogeneities normally dominate the contribution of density perturbations for scales considered here. There-

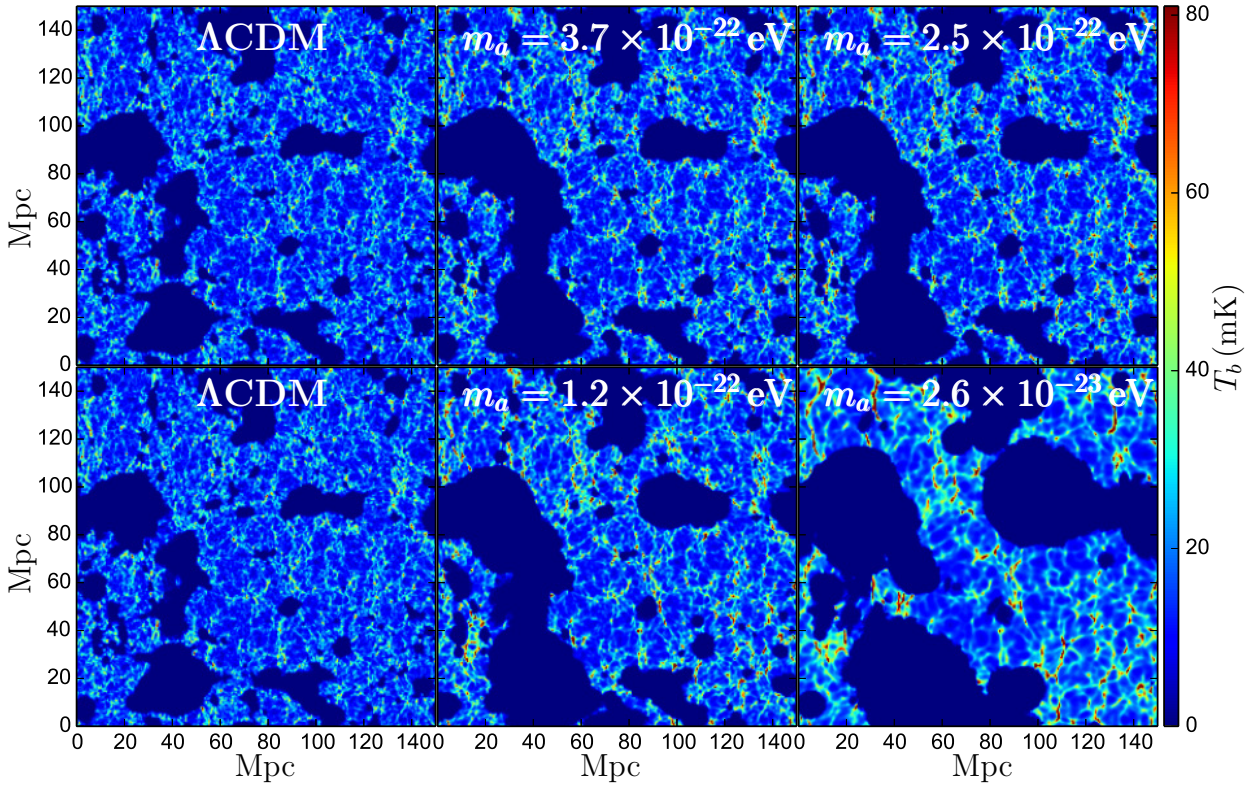

Figure 4.5: Two dimensional sections through the simulated brightness temperature maps of the four different axion dark matter models with axion masses $m_a = 3.7 \times 10^{-22}$ eV, 2.5×10^{-22}eV, 1.2×10^{-22}eV and 2.6×10^{-23}eV for $\bar{x}_{\rm HI} = 0.5$. The ΛCDM (left) map has been shown twice. The direction of redshift space distortion is with respect to a distant observer located along the vertical axis.

Model	Parameter	$N_{\rm ion}$	Reionization
CDM	[55]	24	$\surd$
LFDM	$z_f = 2.0$M	47	$\surd$
	$z_f = 1.0$M	102	$\surd$
	$z_f = 0.7$M	212	$\surd$
	$z_f = 0.4$M	1230	$\times$
	$z_f = 0.2$M	No Haloes	$\times$
ULADM	$m_a = 3.7 \times 10^{-22}$eV	61	$\surd$
	$m_a = 2.5 \times 10^{-22}$eV	75	$\surd$
	$m_a = 1.2 \times 10^{-22}$eV	134	$\surd$
	$m_a = 2.6 \times 10^{-23}$eV	965	$\times$
	$m_a = 2.0 \times 10^{-23}$eV	No Haloes	$\times$

Table 4.1: The Table lists the values of $N_{\rm ion}$ for the LFDM and ULA models we consider. In the last column the tick mark illustrates whether the models is able to achieve reionization based on an acceptable value of $N_{\rm ion}$ and the formation of haloes in the N-body simulation.

fore we expect, for the same ionized fraction, the power to increase if the ionized bubbles are larger. It has been shown analytically [188] and is consistent with the results of numerical simulations [205]. Conversely, when there is enhancement of matter power at small scales, e.g. owing to the presence of primordial magnetic fields, the HI signal in the range of scale discussed here, diminishes [206].

We only consider a fixed ionization fraction $\bar{x}_{\rm HI} = 0.5$ at $z = 8$ for our study. However, the discussion in the foregoing shows that the enhancement of the HI signal is generic and should be independent of the ionization fraction. It can be shown that the HI signal is dominated by ionization inhomogeneities and it peaks at close to $\bar{x}_{\rm HI} = 0.5$ [188], which also partly motivates our choice.

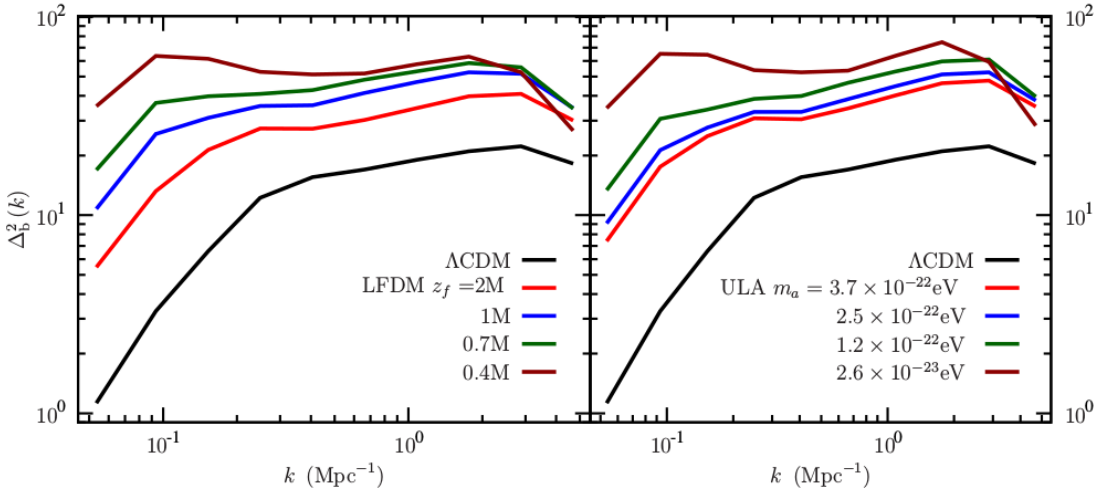

Figure 4.6: This shows the brightness temperature power spectrum $\Delta^2_{\rm b}(k)$ (mK^2) of the HI field for the four different LFDM models (left panel) with $z_f = \{2, 1, 0.7, 0.4\} \times 10^6$ and four different axion dark matter models (right panel) with axion masses $m_a = \{3.7, 2.5, 1.2, 0.26\} \times 10^{-22}$ eV. The black solid curves are for the ΛCDM model.

Current observational constraints from radio interferometer PAPER put an upper limit on the HI bright temperature power spectrum: $\Delta^2_b(k) < (22.4\text{mK})^2$ over the range of scales $0.15 < k < 0.5\text{kMpc}^{-1}$ at $z = 8.4$ [207]. These constraints are too weak, by roughly a factor of 10, to probe the enhancement of the HI signal seen in Figure 4.6 for LFDM and ULA models at the present. Ongoing radio interferometers focused on detecting the HI signal from EoR—LOFAR, MWA, and PAPER—might throw more light on this issue in the near future.

4.4 Evolution of the Cosmological Gas Density

The Damped Lyman-α systems

Before going into the discussion of our work, we provide a description of the DLA systems to establish its cosmological importance.

The neutral and molecular phases of the interstellar medium of galaxies, though make up a tiny fraction of the cosmological baryon density, contains the fuel for star formation at all redshift. Thus, to understand the formation of the evolution of galaxies, it is important to measure the cosmological gas density of neutral hydrogen at different redshifts. At present, the

universe is highly ionized with a tiny fraction of neutral hydrogen present in galaxies and the IGM. In the local universe, the neutral hydrogen is best traced by measurements of the 21-cm emission lines, which can put tight constraints on the density and frequency distribution of HI column density. However, as the sensitivities of current radio telescopes are limited, direct detection of HI through measurements of emission lines are limited to $z \sim 0.2$ [208].

At high redshifts, neutral hydrogen is traced by a series of absorption deeps in spectra of distant quasars, commonly known as the Lyman-α forest, as shown in the left panel of Figure 4.7. The line of sight connecting the quasar and the observer contains a collection of neutral hydrogen clouds. The photons from the quasar excite the electron of the hydrogen atoms present in the intervening medium. If the excitation happens from the ground state (n=1) to the first excited state (n=2), it leads to the Lyman-α absorption deep in the spectrum, with a rest frame wavelength of 1216 Å. As the line of sight contains a lot of such clouds, a series of absorption lines are seen, making it look like a forest. The Lyman-α forest is a useful tool to probe the IGM by determining the column densities and temperatures of the clouds. Depending on the column density, these clouds have different nomenclature. The DLA clouds are those which have neutral hydrogen column density N(HI) $\geq 2 \times 10^{20} cm^{-2}$ [209]. Because of this high column density, it induces a broad and deep absorption feature in the quasar spectrum which makes it easy to detect even if the spectrum has low resolution (Please refer to the right panel of Figure 4.7). The column density given above is also a critical surface density limit for star formation in galaxies. Because the DLAs can be detected easily and the neutral hydrogen column density can be estimated fairly accurately, they can be used to measure the evolution of cosmological HI density at high redshifts with a sufficient number of quasar absorption spectrum. Although, the bias in selecting the quasars and determination of redshift path length can affect the measurement of the column density.

In this work, the physical quantity of interest is the density of gas that is trapped inside the DLAs(Ω_g^{DLA}), which, in terms of the frequency distribution of the HI column density ($f(N,\, X)$) is given by [210]

$$\Omega_g^{DLA} = \frac{H_0}{c} \frac{\mu_{\rm mol} m_H}{\rho_c} \int_{N_{\rm min}}^{N_{\rm max}} dN\, N\, f(N, X) \tag{4.2}$$

Here X is the absorption length of the line of sight defined as $X(z) = \int_0^z (1+z')^2\, H_0/H(z')\, dz'$, $\mu_{\rm mol}$ is the mean molecular weight of gas including Helium and m_H is the mass of Hydrogen

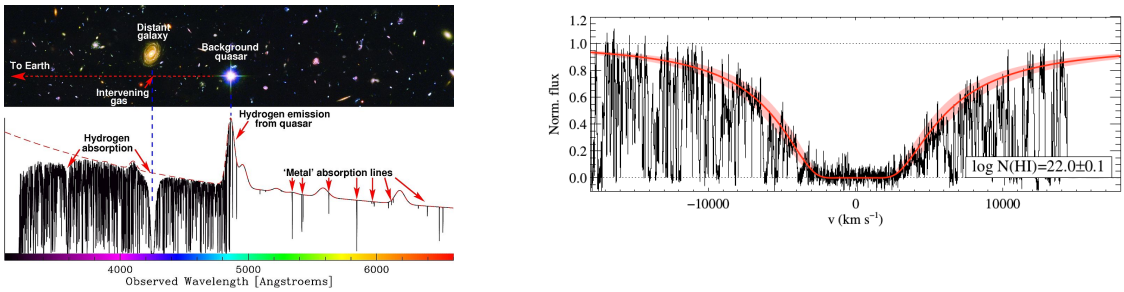

Figure 4.7: Left Panel: Formation of Lyman-α forest in a background quasar spectrum due to presence of neutral hydrogen gas clouds. Photo credit: European Southern Observatory. Right Panel: Spectral feature of a DLA cloud in the Lyman-α forest spectrum, with broader absorption deep that is distinct from other absorption lines. This spectrum is taken from [10].

atom. In this work, this gas density, taken from several survey release data sets, is converted to the collapsed fraction of gas at desired redshifts and compared to theoretical predictions. The results thus found for different dark matter models, including the formalism, are provided below.

Estimation of evolution of cosmological gas density

As discussed in the previous section, the main impact of LFDM and ULA models is to reduce the matter power at small scales. This results in smaller number of haloes at masses relevant for studying the reionization process. This also means the collapsed fraction of matter decreases for models with lower power. We study the implication of the evolution of the collapsed fraction for LFDM and Axion models in this section.

From absorption studies of DLA clouds, the evolution of average mass density of HI in the universe can be inferred [211, 212]. Assuming that the HI follows baryons and the collapsed fraction of baryons traces dark matter, this allows us to get an approximate measure of the minimum amount of collapsed fraction of the total matter in the redshift range $2 < z < 5$ for which the data are available [10,11,211]. From the HI data one obtains, $\Omega_{\rm HI}(z) = \rho_{\rm HI}^{\rm coll}(z)/\rho_c(z)$, which gives the fraction of the collapsed neutral hydrogen in terms of critical density of the universe ρ_c. The (minimum) collapsed fraction is given by: $f_{\rm coll}(z) = \rho_c(z)/\rho_b(z)\Omega_{\rm HI}(z)$, where ρ_b is the background energy density of Baryons.

As obtaining the mass function from N-body simulation is numerically expensive, for com-

puting the collapsed fraction, for LFDM models, we integrate the Sheth-Tormen mass function [192,213] above the density threshold of collapse at a given redshift. The collapsed fraction (the fraction of collapsed mass in haloes with masses larger than M) at a redshift z is given by:

$$f_{\rm coll}(M,z) = \int_{\nu_{\rm min}}^{\infty} \nu f(\nu) \frac{d\nu}{\nu} \tag{4.3}$$

Here $\nu_{\rm min} = (1.69/\sigma(M,z))^2$ and $f(\nu)$ is given by the Sheth-Tormen mass function [192, 213]. For computing the collapsed fraction for ULA models, we integrate the halo mass functions derived by [9].

In Figures 4.8 and 4.9 we show the mass dispersion $\sigma(M)$ for a range of LFDM and ULA models and collapsed fraction as a function of mass for a fixed redshift. It is seen that as the formation redshift z_f (m_a) decreases, $\sigma(M)$ decreases for masses which correspond to scales at which there is decrement in power. This also means that collapse fraction falls as z_f (m_a) decreases.

It is not straightforward to compare the theoretical collapsed fraction (Eq. (4.3) with the DLA data because there is a large uncertainty in the masses of these clouds. Simulations suggest that the mass of damped-α clouds could lie in the range 10^9–$10^{10}\,{\rm M}_\odot$ [214]. However, recent observations suggest that the mass could be as high as $10^{12}\,{\rm M}_\odot$ at $z \simeq 2.5$. [215]. For the present work, we assume two halo masses 10^{10} and $5\times10^{10}\,{\rm M}_\odot$ as the threshold masses for the formation of DLA clouds. We compute the collapsed fraction for comparison with the data by integrating the mass function with threshold mass as lower limits.

In Figures 4.10 and 4.11 we compare the prediction of LFDM and ULA models with the DLA data. As noted above, the DLA data provide a lower limit to the collapsed fraction. Therefore, all models that predict collapsed fraction smaller than the data can be ruled out. As expected, the constraints are tighter for the higher threshold halo mass. Figures 4.10 and 4.11 show that $z_f < 2\times10^5$ and $m_a < 10^{-23}\,{\rm eV}$ can be ruled out from the present data. It should be noted that the data at higher redshifts provide tighter bounds.

In the foregoing we discussed the impact modified dark matter models on the collapsed fraction of HI at high redshifts. It is possible to observe the collapsed fraction of matter at high redshifts in other wave-bands in the form of luminosity function of galaxies. Such observations have been considered to constrain the ULA models [216]. Here we briefly discuss the possible constraints on dark matter models from the currently existing observations of the luminosity

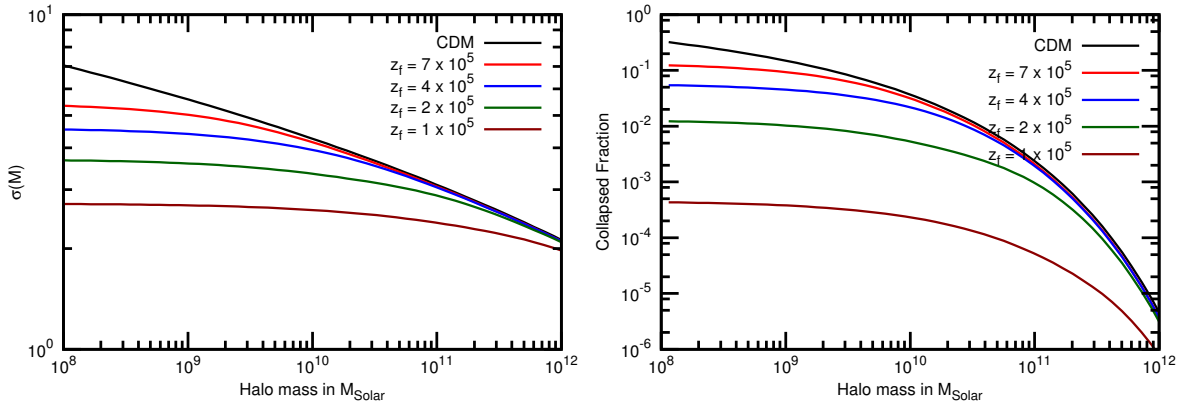

Figure 4.8: The mass dispersion σ_M is shown for a range of LFDM models (Left Panel). The right panel shows the collapse fraction as a function of halo mass. Both the panels are for $z = 6$.

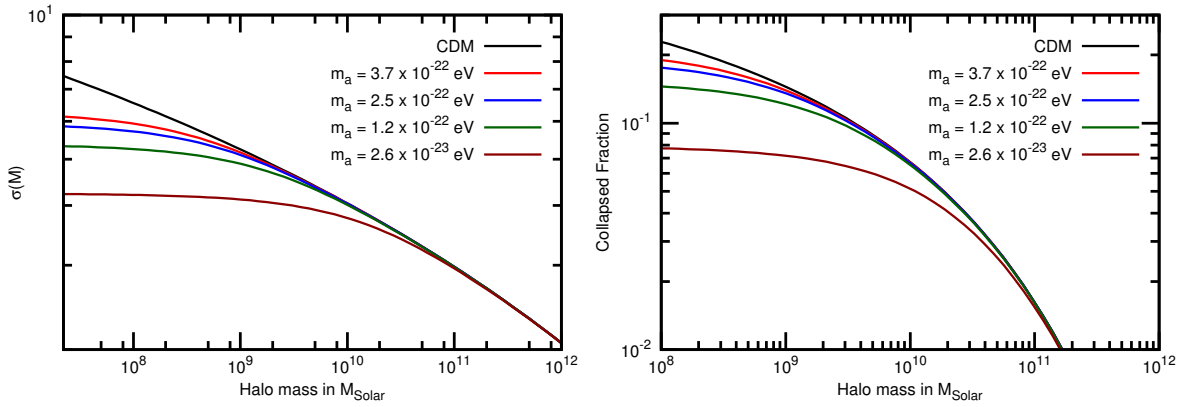

Figure 4.9: The same as Figure 4.8 for ULA models.

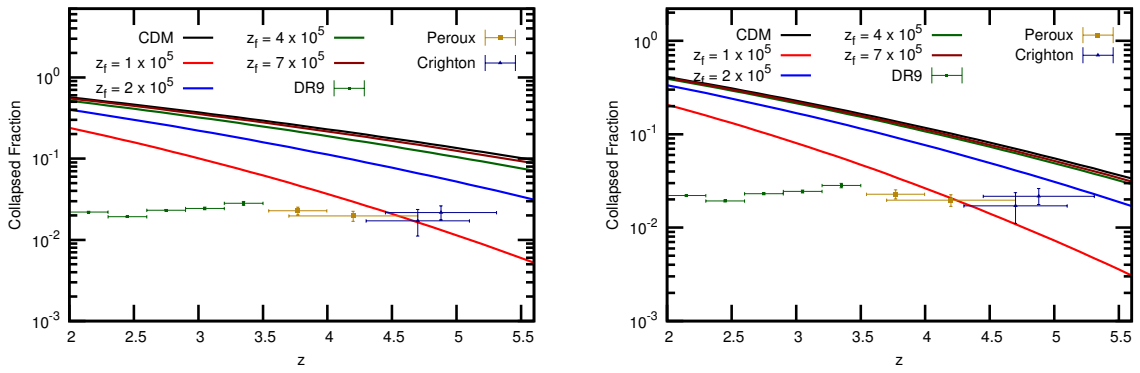

Figure 4.10: The redshift evolution of collapsed fraction for LFDM models is shown along with with the data from DLA absorption data [10, 11, 211, 219]. The left (right) panels correspond to threshold halo masses $M = 10^{10}\,\mathrm{M}_\odot$ ($M = 5 \times 10^{10}\,\mathrm{M}_\odot$), respectively.

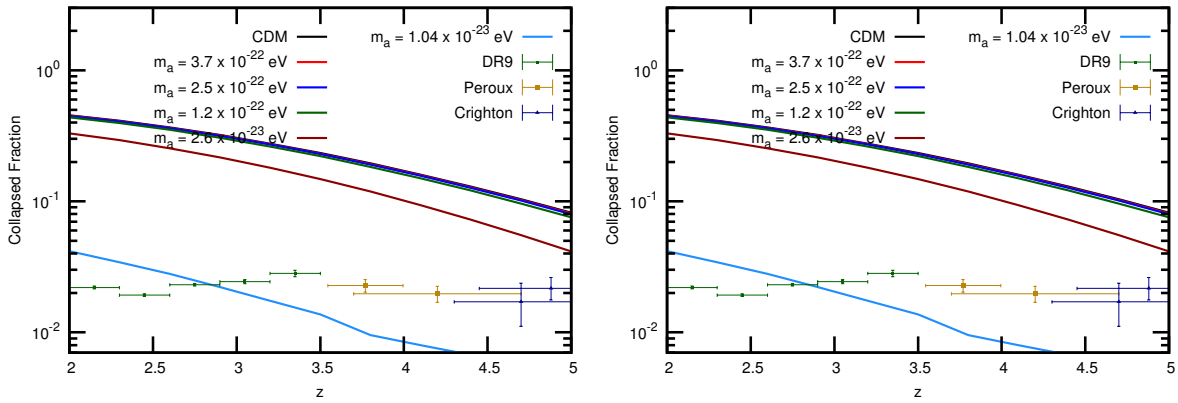

Figure 4.11: The same as Figure 4.10 for ULA models

function of high redshift galaxies.

Many groups have recently determined the luminosity function of bright galaxies, using colour-based Lyman-break selection criterion to determine the redshift, in the redshift range z = 7 – 8 [217, 218]. We focus on the paper of Bouwens et al. (2015) [218]for our discussion.

Their determination of luminosity functions of galaxies is based on 481 sources at $z \simeq 7$ and 217 sources at $z \simeq 8$. For $z \simeq 7$ they cover the absolute magnitude range $M_{AB} = -22.16$ – -16.91 and the range for $z \simeq 8$ is $M_{AB} = -21.87$ – -17.62. To constrain dark function of haloes predicted by these models. It should be underlined that the mass of haloes is not measured directly in such observations and therefore such a relation is based on empirical

fitting based on mass-luminosity relations at lower redshifts. In appendix I of Bouwens et al. (2015) paper, they propose a redshift-dependent kernel to relate the measured luminosity functions with mass functions. They propose a relation between mass and luminosity based on a log-normal kernel and claim an acceptable fit in the redshift range z = 4–8 and reasonable agreement with earlier results. Their eq. I2 gives a redshift-dependent relation that can be used to approximately determine mass given the luminosity (this relation is not unique but the fluctuation in this relation is small, eq. I1 of Bouwens et al. (2015)). For the range of absolute magnitudes for which the luminosity functions have been determined this gives the mass range: $M \simeq 2 \times 10^{10} - 10^{12} M_{\odot}$ at $z \simeq 7$ and $M = 3 \times 10^{10} - 10^{12} M_{\odot}$ at $z \simeq 8$.

We can compare this mass range with our results in figures 7 and 8. These figures show that for most of the models (both LFDM and ULA) we consider, the predictions for the mass range of interest are in reasonable agreement with the ΛCDM model, even though they differ significantly for smaller masses. For the mass range suggested by measured luminosity functions for $z \simeq 7 - 8$, there is substantial difference between the LCDM model and the modified dark matter for $m_a \simeq 2.6 \times 10^{-23}$ eV and $z_f < 2 \times 10^5$. This is suggestive that these models are ruled out by high-redshift luminosity function measurements. These constraints are in reasonable agreement with those obtained from other observables we consider in this chapter.

4.5 Conclusion

In this chapter, we consider the implications, and possible constraints on, of a class of LFDM and axion-inspired models by running a series of N-body and reionization field numerical simulations with the appropriate power spectra as initial conditions. Specifically, we study the reionization epoch and the evolution of the collapsed fraction of matter at high redshifts. Such models generically give a decrement in matter power at small scales. In particular, we study the HI signal from the EoR. We also consider the evolution of the collapsed fraction of the matter in the redshift range $2 < z < 5$, using the data of DLA on $\Omega_{\rm HI}(z)$.

We show that the power spectrum of the HI field could be higher for such models for a fixed ionization fraction as compared to the ΛCDM model. The enhancement is by factors of 2–10 for range of scales $0.1 < k < 4\,{\rm Mpc}^{-1}$. (Figure 4.6).

For studying the EoR with alternative dark matter models, we demand that these models

be able to provide a reionization fraction $x = 0.5$ at $z = 8$. For very low z_f and m_a, no halos are formed at $z = 8$ in the N-body box, which rules out of these models. In models with larger z_f and m_a, the desired amount of reionization is achieved by increasing the number of ionizing photons, $N_{\rm ion}$ as compared to the ΛCDM model. The models that require unrealistically large value of the number of ionizing photons are also excluded. These considerations are listed in Table 4.1 and lead to generic bounds on the epoch of the formation of dark matter $z_f > 4 \times 10^5$ and the axion mass $m_a > 2.6 \times 10^{-23}\,\mathrm{eV}$. We also obtain weaker constraints from the DLA data on the evolution of collapsed gas fraction: $z_f > 2 \times 10^5$ and $m_a > 10^{-23}\,\mathrm{eV}$.

The models we consider in this chapter have been studied in the context of other cosmological observables. The LFDM models have been compared against the SDSS galaxy clustering and the Lyman-α data (Chapter 3); the SDSS data gives $z_f > 10^5$ while the Lyman-α data results in stronger bounds $z_f > 9 \times 10^5$ (all 3σ). While the Lyman-α data give more stringent constraints than we obtain here, the models consistent with this data still result in an enhancement of up to a factor of 4 in the HI power spectra (Figure 4.6). The ULA models considered here have been confronted with Lyman-α and galaxy luminosity data; the resulting bounds are $m_a > 10^{-22}\,\mathrm{eV}$ which are comparable to the constraints we obtain this chapter [144, 194]. It is interesting to note that the current constraints on ULAs, including our own, are consistent with the mass necessary for a successful solution of the cusp-core problem in dSph [146, 193, 220].

Building a physical model of the nature of dark matter consistent with all the astrophysical and cosmological observables has not been achieved yet. Cosmological observables affected by small scale matter power remain crucial elements in this quest. In this chapter we studied the impact of two such observables for two classes of non-WIMP dark matter models and were able to constrain their underlying parameters. In the next chapter we will explore the effects of small-scale power suppression on the spectral distortion in the CMB, a probe which allows us to reach scales as small as $k \sim 10^4\,\mathrm{hMpc}^{-1}$.

Chapter 5

Observational signatures II: Spectral Distortion in the CMB

In the last chapter, we discussed the effects of small-scale power suppression on two distinct and appealing epochs of the universe. Here, we consider one unique probe of the thermal history of the early universe: "The Spectral Distortion in the CMB". The spectrum of the CMB is the best blackbody spectrum that has ever been measured till date, with a temperature of 2.725K at present. But, as discovered by the COBE-FIRAS experiment [53], it contains fluctuation from the blackbody nature with amplitude as tiny as 1 in 10^5 or smaller. The magnitudes and spectral forms of these distortions are goldmines of that information of the early universe, which are difficult to extract otherwise. Any energy injection or extraction process, continuous or instantaneous, that occur after a particular time($z \lesssim 2 \times 10^6$) can potentially distort the CMB spectrum from its blackbody nature. Depending on the time and duration of the energy release process, the distortion can different shapes with different distortion amplitudes. As the distortions are minuscule, they can be directly added weighted by their corresponding amplitudes to give the final spectrum.

The damping of acoustic waves in the early universe due to the diffusion of photons, well known as the Silk Damping(SD), is the energy injection process of interest in this work. The energy released due to this process keeps distorting the CMB spectrum since the universe was a few years old till decoupling and gives rise to three different kinds of distortion. Scales ranging from $k \simeq 0.3{-}10^4\,\mathrm{hMpc}^{-1}$ can be probed using this observable, where the nature of the power

spectrum is not known with good precision or not even known at all using structure formation surveys. The suppression of power due to alternative dark matter candidates occur at scales in this range. The heating due to SD depends on the time evolution of fluctuation of the gravitational potential and the CMB dipole transfer function, both of which depends on the transfer function of the dark matter. Thus, it's expected that the amount of distortion will be altered due to the presence of new dark matter candidates. Thus, the spectral distortion can be considered as a promising observable that can be used to probe the nature of power spectrum at small scales.

This chapter is planned as follows. In Section 5.1 a physical description of the formation and evolution of the spectral distortion in the CMB is provided. The next section describes how the spectral distortion is related to the nature of dark matter through gravitational potential and the CMB dipole. The results of this work are presented in Section 5.3and Section 5.4 is reserved for the conclusion and observational challenges. This chapter is based on the work presented in [12].

5.1 Physics of the Spectral Distortion in the CMB

In this section, the physics of spectral distortion in the CMB will be discussed in more detail. In Figure 5.1 different epochs related to the evolution of CMB distortion are shown. There are four phases in this regard, and we provide a brief physical picture of each of these.

In the early universe, there are two classes of physical processes that can cause energy exchange between electrons and photons and therefore act to equilibrate photon distribution function to a black body. One is photon conserving process, dominated by inverse Compton scattering and photon producing processes which are mediated by double Compton scattering and free-free emission with double Compton scattering dominating the rate of production of photons in the early universe. If both these processes act on time scales shorter than the expansion time scale of the universe, any injection of energy in the universe is rapidly shared between the photons and charged particles, and the CMB spectrum relaxes to a black body (see e.g. [221–224]).

This condition is obtained in the first era $z \gtrsim 2 \times 10^6$. Any injection of energy during this era, e.g. e^+/e^- annihilation and BBN, leaves no trace on the CMB spectrum.

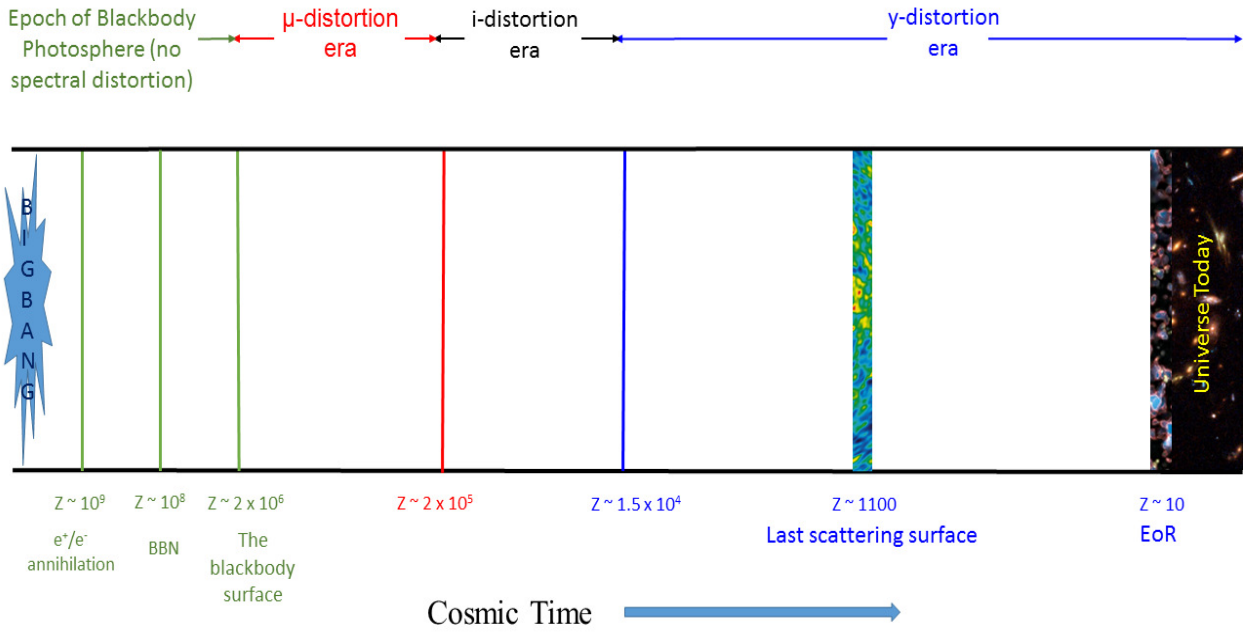

Figure 5.1: Important epochs of the evolution of spectral distortion in the Cosmic Microwave Background.

For $z \lesssim 2 \times 10^6$ the rate of photon production is not large enough to equilibriate the photon distribution function to a black body except at low photon frequencies. This redshift thus approximately marks the time after which the signature of energy injection can no longer be erased. As Compton scattering remains an efficient process for energy exchange between photons and electrons, the resultant distribution function relaxes to a Bose-Einstein distribution with $T_\gamma = T_e$ but with a non-zero chemical potential, μ. This arises because Compton scattering is a photon conserving process that cannot cause a transition between two Black bodies at two different temperatures. During this phase, the evolution of the photon distribution function, $n(\nu, t)$ with Compton scattering being the only energy-exchange process, is given by the well-known Kompaneets equation:

$$\frac{\partial n}{\partial t} = \frac{n_e \sigma_T k_B T_e}{m_e c} \frac{1}{x_e^2} \frac{\partial}{\partial x_e} x_e^4 \left[\frac{\partial n}{\partial x_e} + (n + n^2) \right] \tag{5.1}$$

Here T_e is the electron temperature, n_e is the number density of electrons, m_e is the mass of the electron and $x_e = h\nu/k_B T_e$, ν being the frequency of the photon, is the dimensionless frequency. The general equilibrium solution of this equation is given by [225, 226]

$$n(\nu) = \frac{1}{e^{x_e + \mu} - 1} \tag{5.2}$$

The chemical potential μ can be related to the fractional energy absorbed by the photon gas: $\mu = 1.4 \Delta\rho_\gamma / \rho_\gamma$ (e.g. [221, 226]).

For $z \lesssim 2 \times 10^5$, the Comptonization process is not efficient enough to bring the photon distribution function into equilibrium, and the equilibrium solution of Kompaneets equation (Eq. 5.2) is not valid anymore. This redshift marks the end of μ-distortion era. This era is followed by "i-distortion" and "y-distortion" eras. We first discuss the physics of y-distortion.

The distribution function in Eq. 5.2 satisfies the following identity : $\frac{\partial n}{\partial x} = -(n + n^2)$ where $x = h\nu/kT$. Assuming small departure from equilibrium, Eq. 5.1 can be written as follows:

$$\frac{\partial n}{\partial t} = \frac{n_e \sigma_T k_B (T_e - T)}{m_e c} \frac{1}{x^2} \frac{\partial}{\partial x} x^4 \left[\frac{\partial n}{\partial x} \right] \tag{5.3}$$

The time variable of Eq. 5.3 can be modified as a new parameter which denotes the temperature difference between electrons and photons:

$$dy = \frac{n_e \sigma_T k_B (T_e - T)}{m_e c} dt \tag{5.4}$$

Eq. 5.3 can be solved to give [225, 227]:

$$n(x,y) = n(x,0) + \frac{xye^x}{(e^x-1)^2}\left[\frac{x}{\tanh(x/2)} - 4\right] \tag{5.5}$$

In this case the fractional change in photon energy can be related to the y-parameter as: $y = 1/4\Delta\rho_\gamma/\rho_\gamma$ [227].

Between μ- and y-distortion era there exists another era called the "intermediate (i-type) distortion era". In this time, the Comptonization time scale is not short enough to relax the spectrum to equilibrium. Instead, the system settles into a state where the distortion is given by the sum of μ-,y- and some residual distortion [228, 229]. The thermalization in this era is approximated as a weighted combination of pure μ- and y-distortion [229]. The residual distortion (r-type) is between 10-30% of the total distortion. This r-type distortion depends sensitively on the time of energy injection, which is not the case for pure μ- or y-distortion. A different approach was taken in [230] to quantitatively describe the i-distortion. The i-distortion can be characterised by a modified y-parameter defined as:

$$y_\gamma(z_{inj}, z_{max}) = -\int_{z_{max}}^{z_{inj}} \frac{n_e\sigma_T k_B T}{m_e c H(1+z)} dz \tag{5.6}$$

The Kompaneets equation is written in terms of this new time parameter and then expanded about y_γ. The solution shows that the distorted spectrum and thus the distortion is dependent on y_γ. According to Eq. 5.6, y_γ is sensitive to the time when the energy was injected into the system through z_{inj}. This makes the i-distortion able to estimate not only the amount of energy injected but also the time of injection, something that can't be estimated by observing the μ or y-type distortion.

After $z \sim 1.5 \times 10^4$, y_γ becomes very small and y-distortion epoch commences and lasts up to present time. Late time phenomena of the universe like reionization [230, 231], heating of photons by warm-hot intergalactic medium [232, 233] and SZ effects from groups and clusters of galaxies ([234, 235] and references therein) also contribute to the y-distortion. As long as the amount of distortion is small, the three different distortions (μ+y+r) can be linearly added to give the final spectrum.

Various processes like decay of massive particles [228, 236, 237], annihilation of particles [238, 239], dissipation of acoustic wave [238, 240–243], adiabatic cooling of electrons [238] and cosmological recombination radiation [244–246] can contribute energy into or extract energy from the photon-baryon plasma leading to spectral distortion in the early universe. In this

work, we study the spectral distortion caused by dissipation of acoustic wave for different dark matter models. A detailed description of that process is given in next section.

Energy released due to Silk Damping

At $z \gtrsim 1100$, the photon and baryons are tightly coupled to each other via Compton scattering and behave like a single fluid. Adiabatic perturbations in this fluid behave like standing waves inside the sound horizon $r_s = c_s\eta$, where $c_s = c/\sqrt{3(1+R)}$ is the speed of sound in the plasma and $R = 3\rho_b/4\rho_\gamma$. At scales much smaller than the sound horizon, photon diffusion causes damping of density perturbation and bulk motion of this fluid [45]. This process can be modelled by expanding the evolution of perturbations in the coupled photon-baryon fluid to second order in the mean free path of photons [173,247] or as the dissipation of energy of sounds waves owing to radiative viscosity and thermal conduction [248]. SD causes the injection of entropy into the thermal plasma.

As this is a continuous energy injection process, it can lead to μ-type, i-type or y-type distortion depending on the era when the energy was injected. In the redshift range, $10^6 \gtrsim z \gtrsim 10^3$, the structures corresponding to scales $k \simeq 0.3$–$10^4\,\mathrm{Mpc}^{-1}$ are completely wiped out due to this damping and, conversely, one possible way to study and constrain the initial power spectrum at these scales is by observing the spectral distortion that is imprinted in the CMB spectrum due to this process. It should be noted that this is the only known probe of linear structures for such a wide range of small scales. In comparison, the observed CMB temperature anisotropies from Planck probe scales $k \lesssim 0.1\,\mathrm{Mpc}^{-1}$ [55] and the smallest scales probed by galaxy clustering data correspond to nearly linear scales at the present: $k \lesssim 0.1\,\mathrm{Mpc}^{-1}$.

The damping of adiabatic perturbations at small scales has been well studied in the literature. Recently a precise calculation of μ- and y-type distortion due to SD has been performed using the second order perturbation theory [242]. It has been shown that tight-coupling approximation provides a good approximation for modeling the SD in the pre-recombination era.

In this approximation, the source function for heating due to SD is given by [242][1]:

$$S_{SD}(k,\eta) \simeq \frac{k^2}{\dot{\tau}_c^2}\left[\frac{R^2}{1+R}+\frac{16}{15}\right]|\Theta_1(k,\eta)|^2 Y_{SZ} \tag{5.7}$$

Where $\Theta_1(k,\eta)$ is the CMB dipole anisotropy, $\dot{\tau}_c = cn_e\sigma_T a$ is the derivative of Compton scattering optical depth with respect to the conformal time and Y_{SZ} is the frequency dependent function representing the y-distortion defined in Eq. 5.5. The first term in the square bracket comes from heat conduction and the second one is due to radiative viscosity. At high redshift, the radiative viscosity dominates as $R \to 0$. As any time, the average source function can be obtained by integrating over all wavenumbers:

$$\langle S_{SD}\rangle(\eta) = \int \frac{d^3k}{(2\pi)^3} S_{SD}(k,\eta) \tag{5.8}$$

To obtain effective heating rate $\langle S_{SD}\rangle$ needs to be multiplied by $\dot{\tau}_c$ and integrated over all frequencies. The integration over frequencies, $\int x^3 Y_{SZ} dx$, yields $4\rho_\gamma$. This result provides the heating rate as a function of conformal time which is converted to a function of redshift by dividing it by $H(1+z)$. Thus, the final expression of heating rate is given by

$$\frac{1}{a^4\rho_\gamma}\frac{da^4Q}{dz} \approx \frac{4\dot{\tau}_c\langle S_{SD}\rangle}{H(1+z)} \tag{5.9}$$

The μ and y-parameters are related to heating rates as follows [242, 250]

$$\mu = 1.4\int_{z_\mu}^{\infty} \exp(-[z/z_\mu]^{5/2})\frac{dz}{a^4\rho_\gamma}\frac{da^4Q}{dz} \tag{5.10}$$

and

$$y = \frac{1}{4}\int_{z_{\rm dec}}^{z_i} \frac{dz}{a^4\rho_\gamma}\frac{da^4Q}{dz} \tag{5.11}$$

$z_{\rm dec} \simeq 1100$ and $z_i \simeq 1.5\times 10^4$ are the redshift of decoupling and the redshift denoting the end of i-distortion era, respectively.

[1] the source function given in Eq. (5.7) can be understood as arising from radiative viscosity. In this case the energy pumped into the thermal plasma is proportion to the square of the product of the photon mean free path with the velocity shear field (e.g. [249]) which is proportional to $k^2\Theta_1^2/\dot{\tau}_c^2$. Alternatively, the dissipation of the energy can be modelled in terms of photon monopole [241]. Both these approaches give results within a factor of 3/4 of each other [242]. While numerically computing CMB spectral distortion, we use both the methods and find reasonable agreement

5.2 Spectral Distortion and Dark Matter Models

In this section, we discuss how altering the dark matter model impacts the generation of entropy owing to SD in the pre-recombination era. As noted in the previous section, the dynamics of this energy pumping can be captured by the time evolution of the photon dipole, $\Theta_1(k,\eta)$.

We discuss here how the photon dipole is altered when the dark matter model is changed. We use Newtonian conformal gauge for motivating our discussion as the underlying physics is more transparent in this gauge. In the tight-coupling approximation, the photon dipole can be expressed as (e.g. [251]):

$$\Theta_1(k,\eta) = \left[\frac{1}{\sqrt{3}}\left(\Theta_0(k,0)+\Phi(k,0)\right)\sin(kc_s\eta) - \frac{k}{3}\int_0^\eta d\eta' \left(\Phi(k,\eta')-\Psi(k,\eta')\right)\cos(kc_s\eta - kc_s\eta')\right]\exp(-k^2/k_d^2) \tag{5.12}$$

Here $\Theta_0(k,\eta)$ is the photon monopole and $\Phi(k,\eta)$ and $\Psi(k,\eta)$ are the two gravitational potentials in the Newtonian gauge. If the small contribution from neutrinos is neglected, $\Psi = -\Phi$. [2] $\Theta_0(k,0) = 0.5\Phi(k,0)$ and $c_s = 1/\sqrt{3(1+R)}$. In Eq (5.12) we have neglected $R = 3\rho_B/4\rho_\gamma$ and its evolution in the pre-factors of the equation. [3] $k_d(\eta)$ corresponds to the scale that undergoes SD at any time:

$$k_d^{-2}(\eta) \simeq \int_0^\eta d\eta \frac{1}{\dot{\tau}}\left(\frac{R^2}{6(1+R)^2} + \frac{4}{27(1+R)}\right) \tag{5.13}$$

Here $\dot{\tau} = n_e\sigma_T a$. Under these approximations, the evolution of $\Theta_1(k,\eta)$ can be completely determined by the Newtonian potential $\Phi(k,\eta)$ and the SD scale $k_d(\eta)$. As discussed in the next section, the dissipation of energy at a given scale k occurs predominantly at a time η_d such

[2] $\Psi = -(1+2/5R_\nu)\Phi$ with $R_\nu = \rho_\nu/(\rho_\nu+\rho_\gamma)$; $R_\nu = 0.41$ for three massless neutrino degrees of freedom. Two of the models we consider here can alter R_ν. This means that the first term in Eq. (5.12), which corresponds to initial conditions, can also be used to distinguish between different dark matter models [242]. In WDM models, the dark matter particle is initially relativistic and therefore would increase R_ν. However, even during this phase the contribution of this particle to neutrino relativistic degrees of freedom is negligible as compared to the standard model neutrino; for $m_{\rm wdm} = 1\,$keV, the particle contributes less than 1% of the energy density of a standard model neutrino. In LFDM models, a tiny fraction of neutrino energy density is used to create the dark matter particle during a phase transition (e.g. [4]). For both these models, the effect of initial conditions is generally negligible. We take into account these effects in our detailed modelling using `CMBFAST` but drop it in this sub-section to uncover the main determinants of the impact of dark matter models on the photon dipole.

[3] For the charged decay model, $R = 3(\rho_B+\rho_{\rm dm})/(4\rho_\gamma)$ at early times as the dark matter particle is charged and tightly coupled to the baryon-photon fluid. For this model, this is an additional effect that determines the evolution of $\Theta_1(k,\eta)$. In the results presented in this section, we take into account this effect using `CMBFAST`.

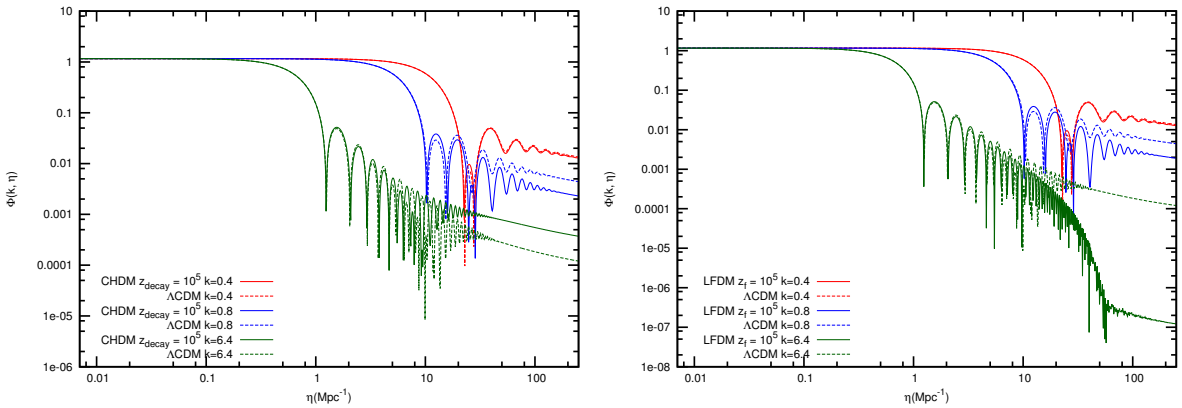

Figure 5.2: The evolution of $\Phi(k,\eta)$, for $k = 0.4, 0.8, 6.4\text{Mpc}^{-1}$, for CHDM (Left panel) and LFDM(Right panel) models are compared to the ΛCDM model. In each subfigure the solid lines stand for the non-standard model and the dotted lines for ΛCDM model.

that $k = k_d(\eta_d)$. As we argue below, the main effect we seek depends on the time evolution of $\Phi(k,\eta)$ in the time range, $1/k < \eta < 1/k_d(\eta_d)$, i.e. from the horizon entry of a scale to the time at which the mechanical energy at this scale dissipates.

All the models we consider in this paper are based on altering the nature of CDM with an aim to suppress power at small scales. While these models impact the radiation content of the universe in the early universe (e.g. WDM model is based on a particle of mass $m_{\text{wdm}} \simeq 1\,\text{kev}$ which is relativistic in the early universe) they all leave unchanged the MRE epoch. This implies that their impact is proportional to the ratio of dark matter to the radiation energy density, ρ_{dm}/ρ_r, which is much smaller than unity at early times. This means that the impact of changing the dark matter change is essentially captured by the second term of Eq. (5.12), which depends on the evolution of the Newtonian potential $\Phi(k,\eta)$.

In Figure 5.2 we show the evolution of $\Phi(k,\eta)$ for two of the models we consider here for a range of wavenumbers k. The Newtonian potential $\Phi(k,\eta)$ is computed from `CMBFAST` code, which is written in Synchronous gauge, using the following transformation:

$$\Phi(k,\eta) = \beta(k,\eta) - \frac{\dot{a}}{ak^2}\left(\dot{h}(k,\eta) + 6\dot{\beta}(k,\eta)\right) \tag{5.14}$$

Here h and β are the potentials in Synchronous Gauge (Eq. 18 of [44]). Some notable features of the comparison between the models we consider and the ΛCDM models are: (a) the difference

between the potentials is negligible of for large scales (small k). This is expected as the models we consider agree with the ΛCDM model on large scales, (b) As the scale gets smaller, the difference between alternative dark matter models and the ΛCDM model becomes more significant at larger η. We discuss the nature of this deviation below.

LFDM model: In this model, the CDM forms at a redshift $z = z_f$ from a tiny fraction of relativistic neutrinos due to a phase transition. It inherits the density and velocity perturbations of the neutrino component, resulting in a sharp reduction in matter power for scales $k > k_{\rm lfdm}$, where $k_{\rm lfdm}$ is the scale that enters the horizon at $z = z_f$.

To understand Figure 5.2 we consider scales smaller and larger than $k_{\rm lfdm}$: (a) $k < k_{\rm lfdm}$: these scales are outside the horizon when the dark matter forms. These scales evolve outside the horizon in a purely radiation dominated universe. The perturbations at these scales are not affected by LFDM physics except in determining the initial conditions which are not necessary for the following reasons: the photon perturbations outside the horizon are constant and are set by the potential. For scales outside the horizon, the potential changes by a factor 9/10 in making a transition from radiation to the matter-dominated era (e.g. [251] and references therein). If the era of LFDM lies deep inside RD era, the change is negligible. This explains the large scale behaviour of potential in Figure 5.2.

(b) $k > k_{\rm lfdm}$: these scales enter the horizon before the formation of the cold dark matter. As $z_{\rm lfdm} \gg z_{\rm eq}$ these scales evolve sub-horizon in the radiation dominated era. In radiation dominated era, the potential $\Phi(k, \eta)$ decays as $(k\eta)^{-2}$ for $k\eta \gg 1$ if perturbations in radiation determine the evolution of the potential (e.g. [251]). At sub-horizon scales, neutrino perturbation decay exponentially while photon density perturbations equal baryon perturbations which oscillate with nearly constant amplitude for $\eta < \eta_d$. The CDM perturbations, on the other hand, grow logarithmically during this phase. This means matter perturbations can determine the evolution of the potential $\Phi(k, \eta)$ even in deep radiation dominated era. This behaviour is seen the evolution of the potential for $k = 0.8$ in Figure 5.2 as flattening of the potential for larger η. For LFDM models, the potential decay is sharper because of the CDM forms late. This behaviour along with other features for $k\eta > 1$ seen in Figure 5.2 explains how the evolution of Φ in LFDM models differs from the ΛCDM model. It is important to note that this difference is most pronounced for scales that enter the horizon at $z \simeq z_f$. For even smaller scales, the effect of matter perturbations is less important as these scales enter the

horizon when $\rho_{\rm dm}/\rho_r$ is lower and therefore matter perturbations have a smaller impact on their evolution. Equivalently, it is seen from Eq. (5.12) that the photon dipole depends on the integral of the potential and as the potential decays inside the horizon, most of the contribution comes from epochs close to the horizon entry. It is also seen in the evolution of the potential for $k = 6.4\,{\rm Mpc}^{-1}$. The potential deviates insignificantly from the ΛCDM model for $k\eta \gtrsim 1$ but shows sharp deviation at later times. The evolution of perturbations at these scales (from $\eta \ll 1$ to $\eta = \eta_d$) correspond roughly to the case of no dark matter at all time. The potential for this case falls exponentially for large η which occurs because the only source of potential in the LFDM model is photon and neutrino perturbations which both decay exponentially for $\eta > \eta_d$. It is of interest to note that the potential at $k = k_d$ is dominated by matter perturbations for $z \lesssim 10^5$.

For the LFDM model shown in Figure 5.2, the scales of interest for measuring the deviation from the ΛCDM model lie in the range 0.6–4 ${\rm Mpc}^{-1}$. These scales enter the horizon before, but not significantly before, the era of matter formation and the perturbations at these scales suffer SD after $z \simeq 10^4$.

For models such as WDM and ULA, the preceding discussion is directly applicable. We briefly discuss the charged decaying particle case below.

Charged Decaying particle: For charged decay model, the variation in the dynamics of $\Phi(k, \eta)$ closely follows the previous discussion for LFDM model: $\Phi(k, \eta)$ nearly follows the potential for ΛCDM model at large scales. At very small scales the effect is suppressed because the matter density is small when they enter the horizon (Figure 5.2). The main impact is captured by intermediate scales that enter the horizon around but before the time of decay.

Some of the salient differences between the two cases can be seen in Figure 5.2. For the Charged decaying particle model, the potential can exceed the ΛCDM values for a range of wavenumbers, e.g. $k = 6.4\,{\rm Mpc}^{-1}$ in the figure.

It follows from our discussion that the impact of alternative dark matter models on $\Phi(k, \eta)$ declines if the transition (decay) redshift moves deeper into the radiation dominated era. We note that the tight-coupling approximation while capturing the essential physics, tends to break down close to the recombination era; this is relevant for the computation of y-distortion [242, 252]. However, this approximation allows us to compare our results in two different gauges and identify the main determinants of altering CMB distortion for alternative dark

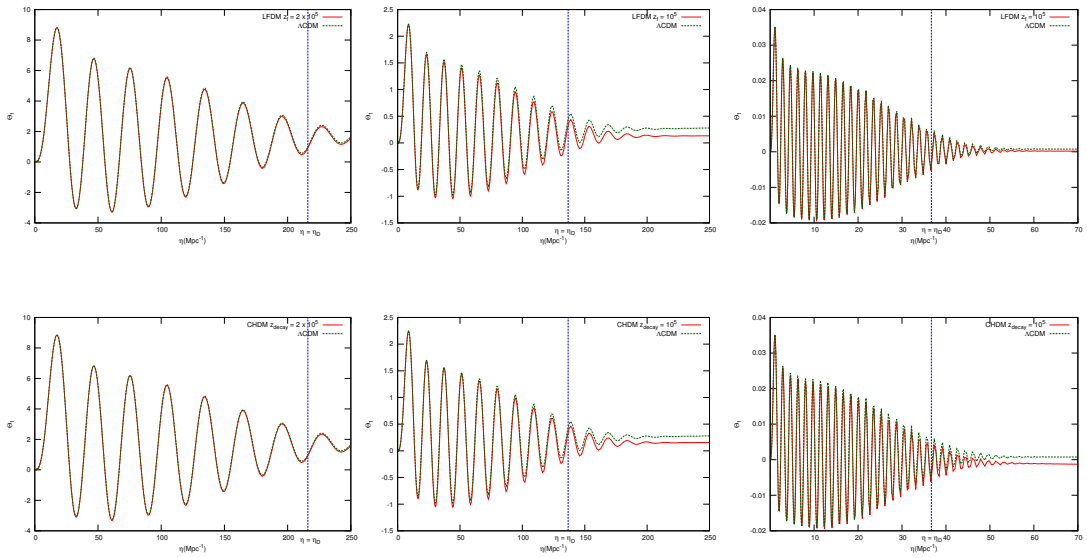

Figure 5.3: The evolution of $\Theta_1(k,\eta)$ for $k = 0.4, 0.8, 6.4\text{Mpc}^{-1}$ for CHDM (lower panel) and LFDM (upper panel) for $z_f = z_{\text{decay}} = 10^5$. In each plot we also show the evolution of the corresponding scale for ΛCDM model. In each plot the vertical dotted line marks the time when $k = k_d$ (Eq. (5.13)) or that particular scale enters the SD regime.

matter models.

In Figure 5.3 we show the dynamics of $\Theta_1(k,\eta)$ for a range of alternative dark matter models. We compute $\Theta_1(k,\eta)$ directly from `CMBFAST` code but also verify that Eq. (5.12), which shows that $\Theta_1(k,\eta)$ depends on the history of the variation of $\Phi(k,\eta)$, explains the main difference expectedfor alternative dark matter models. We establish it by running a smaller set of equations for density and velocity perturbations in photon-baryon fluid and dark matter along with the evolution of $\Phi(k,\eta)$ in conformal Newtonian gauge [44].

In Figure 5.4, we show the values of $\Theta_1(k,\eta)$ at $z = 1000$ of different models at the same redshift. All the models shown correspond roughly to cases where the decrement in the power spectrum occurs at $k \simeq 0.3h\,\text{Mpc}^{-1}$.

The preceding discussion allows us to establish that the main impact of alternative dark matter models is to alter y-distortion and not μ- or i-distortion. The μ-distortion era occurs in the redshift range $2 \times 10^5 \lesssim z \lesssim 2 \times 10^6$. In this era the scales that dissipate their energy and therefore cause the CMB distortion lie in the range $500\,\text{Mpc}^{-1} \lesssim k \lesssim 14000\,\text{Mpc}^{-1}$. In

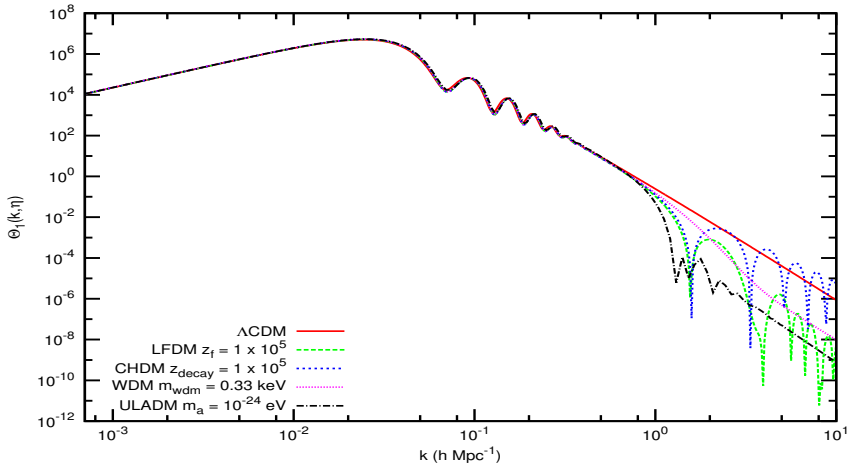

Figure 5.4: CMB dipole transfer function of the four dark matter candidates considered in this work along with ΛCDM. The specifications of the models are same as that of Figure-5.1.

the range of redshifts of interest, the matter power for alternative models at these scales is highly suppressed as compared to the ΛCDM model, as seen in Figure 5.1. However, as argued above, this does not have a significant impact on Θ_1 because it depends on the history of the evolution of the potential $\Phi(k,\eta)$ (Eq. (5.12)). As the potential decays after horizon entry (Figure 5.2), the photon dipole is governed by the initial condition of the potential and its evolution closer to the time of horizon entry of the scale ($\eta = \eta_e$) rather than its value at $\eta = \eta_d$. The scale $k \simeq 500\,\mathrm{Mpc}^{-1}$ (which decays at the end of the μ-distortion era) enters the horizon at $z \simeq 2 \times 10^8$. As the ratio of radiation to matter energy density at this redshift $\rho_{\rm dm}/\rho_r \simeq 10^{-5}$, the potential is insensitive to even a substantial change in the matter power at this scale at early times. The initial conditions for different models are not the same as the ΛCDM model. However, as discussed above, requiring these models to agree with large scale observations forces the impact of the change in initial conditions on the potential to be negligible.

This also implies that the dynamics of scales that determine μ-distortion of CMB are minimally affected by a change in the dark matter model. As we showed above, the main effect in the photon dipole is caused by scales in the range 0.6–4 Mpc^{-1}, this also means the impact of alternative dark matter on the i-distortion era is also negligible. We test this in our study by computing the photon dipole for scales in the range $k < 500\,\mathrm{Mpc}^{-1}$ for alternative models numerically and using an analytic approximation for even smaller scales to discern the impact

of initial conditions (the first term of Eq. (5.12)). For all the models we consider, the μ- and i-distortion is less than 0.1%.

5.3 Results

Using Eqs. (5.12) and (5.7) one can analytically show that the dissipation at any given time is dominated by scales such that $k \simeq k_d$. Such an estimate is based on approximating $\Theta_1(k,\eta)$ by the first term of Eq. (5.12) (e.g. [242]). This gives:

$$S_{SD}(k,\eta) \propto \frac{k^2}{\dot{\tau}_c^{\,2}} P_\phi(k,0) \sin^2(kc_s\eta) \exp(-k^2/k_d^2) Y_{SZ} \tag{5.15}$$

Here $P_\Phi(k,0)$ is the power spectrum of the potential at the initial time. Using $P_\Phi(k,0) \propto k^{-4+n_s}$ (e.g. [242, 251]) where $n_s \simeq 1$ is the scalar spectral index and integrating over k gives:

$$\langle S_{SD} \rangle \propto \int dk k^{n_s} \sin^2(c_s k\eta) \exp(-k^2/k_d^2) \tag{5.16}$$

This k integral in the equation is dominated by $k \simeq k_d$ which means the energy dissipation at any given time is governed by this condition. This result holds even when both the terms in Eq. (5.12) are retained.[4]

This means that the dissipation is dominated by photon dipole at $k \simeq k_d$ at any time η, $\Theta_{1\mathrm{D}} \equiv \Theta_1(k_d,\eta)$. In Figure 5.5 we show the redshift evolution of $\Delta\Theta_{1\mathrm{D}}$, the difference between $\Theta_{1\mathrm{D}}$ for different dark matter models and that of ΛCDM. The set of model parameters we have chosen is provided in Table 5.1. The difference decreases as the redshift of formation z_f for LFDM, and the decay redshift z_{decay} for CHDM and masses of WDM and Axion are increased. One further point to note is that the difference $\Delta\Theta_{1\mathrm{D}}$ for alternative models increases as the redshift decreases. These results are in agreement with our discussion in the previous section which suggested that the alternative dark matter models yield substantial difference only during the y-distortion era.

Using Eqs. (5.7), (5.8) and (5.11), we calculate y-parameter for different models; $\Theta_1(k,\eta)$ is normalized using the condition on mass dispersion at scale $R = 8\,\mathrm{h}^{-1}\mathrm{Mpc}$ at the present epoch:

[4] While the first term of Eq. (5.12) gives a reasonable analytic estimate, the second term generally dominates the first term even for the ΛCDM model. The factor proportional to $\sin(c_s k\eta)$ in the second term dominates over the first term and cancels it but the remainder has the form of the first term and has a similar order of magnitude. The factor proportional to $\cos(c_s k\eta)$ in the second term is generally sub-dominant. These two factors contain information of the evolution of potential which is germane to our work.

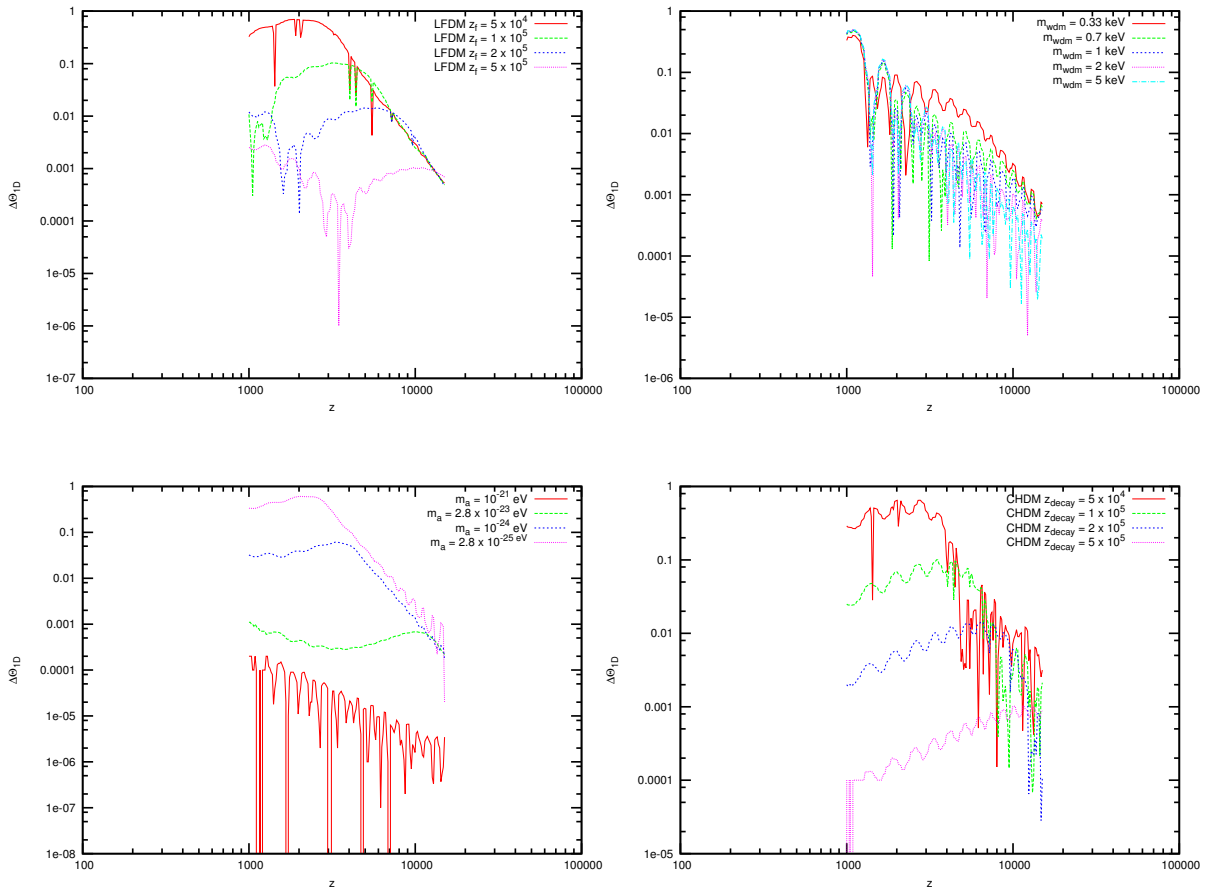

Figure 5.5: The difference between Θ_{1D} for four different dark matter models considered in this work and ΛCDM model: $\Delta\Theta_{1D}$. Clockwise from top-left $\Delta\Theta_{1D}$ for LFDM, WDM, charged particle decay dark matter and ULADM are plotted, respectively.

$\sigma_8(\eta_0) = 0.8225$ [55]. The list of y-parameters for different models is provided in Table 5.1. We note that the y-parameter can vary by up to 10% for a range of models. This behaviour is in line with the variation of $\Delta\Theta_{1D}$. The y-parameter approaches its value for ΛCDM model as z_f for LFDM and $z_{\rm decay}$ for CHDM models are increased, and also when the mass of WDM and axion is increased as expected from our discussion above. Furthermore, we can use Eq. (5.5) to determine the shape of distorted CMB spectrum.

Can the y-distortion be used to distinguish between different dark matter models? We address this question by comparing models where the power is cut at nearly the same scale. In Figure 5.6, we show the evolution of $\Delta\Theta_{1D}$ and the spectral shape of the distorted spectrum for

models for which the power has been cut at $k \simeq 0.3h\,\mathrm{Mpc}^{-1}$. Figure 5.6 also shows the distorted spectrum from y-distortion for these cases; the spectra have the same shape (Eq. (5.5)) but differ owing to slightly different values of the y-parameter. A more detailed analysis based on understanding degeneracies between parameters of different models would be needed to quantify the results shown in Figure 5.6. We also note that this effect can be masked by several late-time phenomena like the EoR, thermal Sunyaev-Zel'dovich(tSZ) effects in the galaxy groups and clusters that give rise to the spectral shape that arises from y-type distortion with orders of magnitude higher y-parameters.

Many of the models we consider are already tightly constrained by cosmological observations. From galaxy clustering and CMB anisotropy data and observed neutral hydrogen (HI) abundance at high redshifts, the LFDM models require $z_f \gtrsim 10^5$ [4, 8]. Lyman-α data puts even stronger constraints on such models [4]. Recent studies of ULA models suggest that $m_a \gtrsim 10^{-22}$ eV is consistent with current observational data [253]. Other studies based on the abundance of HI at high redshift constrain the axion mass $m_a \gtrsim 10^{-23}\,\mathrm{eV}$ [8]. These constraints suggest that some of the models shown in Table 5.1 are ruled out and in particular the ones that show largest deviations from the ΛCDM model. However, there is significant variation in the predictions of different models, and we might expect to see up to 5% deviation (e.g. $z_f \simeq 10^5$) within the framework of constraints that arise from galaxy clustering [254] and CMB anisotropies [255].

The charged decaying particle model offers a more complicated scenario of spectral distortion of the CMB. As noted in section 2.3 in Chapter 2, the relativistic electron released as the decay product rapidly thermalizes its energy with the thermal plasma. Eq. 2.10 gives the fractional increase in the photon energy density due to this process. This constrains the mass difference between the two heavy particles ΔM to be tiny. This scenario therefore presents two different ways of distinguishing this model from the ΛCDM model. For instance, for $z_{\mathrm{decay}} \simeq 10^5$, the decay will cause i-type spectral distortion in the CMB (whose amplitude will depend on ΔM) while Silk damping causes a difference in y-distortion. In principle, given their distinct spectral signatures, these two phases of distortions are distinguishable from each other [236, 237].

The upcoming experiment Primordial Inflation Explorer (PIXIE) [256] is likely to improve the FIRAS bounds on CMB spectral distortion by many orders of magnitude. Its projected

Model	Parameter	$y \times 10^9$	% difference of y from ΛCDM
ΛCDM	[55]	4.4180	0.0
LFDM	$z_f = 5 \times 10^4$	3.8561	14.57
	$z_f = 1 \times 10^5$	4.1001	7.75
	$z_f = 2 \times 10^5$	4.3037	2.65
	$z_f = 5 \times 10^5$	4.3959	0.50
WDM	$m_{\rm wdm} = 0.33$ keV	4.2178	4.74
	$m_{\rm wdm} = 0.70$ keV	4.3105	2.49
	$m_{\rm wdm} = 1.00$ keV	4.3398	1.80
	$m_{\rm wdm} = 2.00$ keV	4.3680	1.14
	$m_{\rm wdm} = 5.00$ keV	4.3798	0.87
CHDM	$z_{\rm decay} = 5 \times 10^4$	3.8913	13.53
	$z_{\rm decay} = 1 \times 10^5$	4.1884	5.48
	$z_{\rm decay} = 2 \times 10^5$	4.2945	2.87
	$z_{\rm decay} = 5 \times 10^5$	4.4002	0.4
ULADM	$m_a = 2.8 \times 10^{-25}$ eV	3.8840	13.74
	$m_a = 1.0 \times 10^{-24}$ eV	4.2812	3.19
	$m_a = 2.8 \times 10^{-23}$ eV	4.3990	0.43
	$m_a = 1.0 \times 10^{-21}$ eV	4.4177	6.8×10^{-3}

Table 5.1: This table lists the values of y-parameter for alternative dark matter models and compared with ΛCDM model.

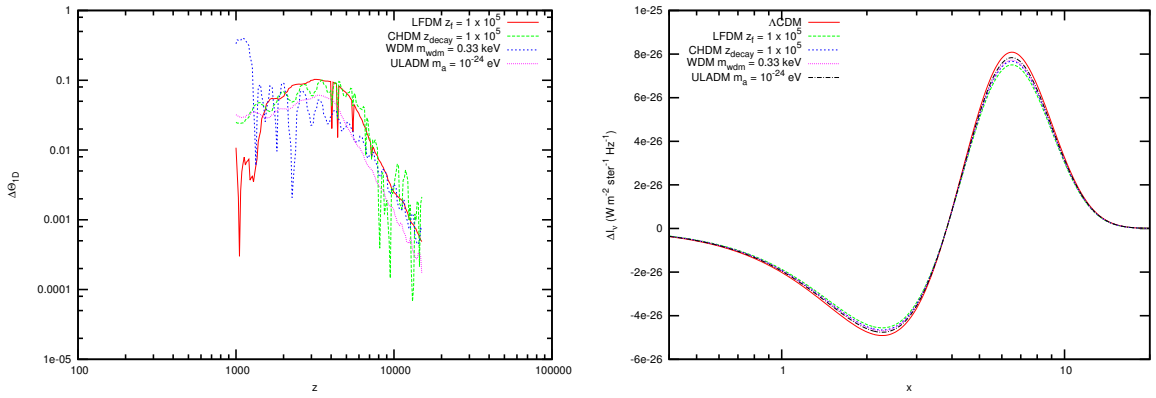

Figure 5.6: Comparison of $\Delta\Theta_{1\mathrm{D}}$(Left) and y-parameter(Right) for four different dark matter candidates having small scale power suppressed at same value of $k \sim 0.3\mathrm{hMpc}^{-1}$.

sensitivity corresponds to: $y \simeq 2\times10^{-9}$ and $\mu \simeq 10^{-8}$. However, unlike the μ- and i-distortion, the y-distortion created during the pre-recombination era can be masked by CMB distortion in the post-recombination era. For instance, the EoR is likely to produce global CMB distortion corresponding to $y \simeq$ a few $\times\, 10^{-7}$, though the most dominating source of post-recombination y-distortion is the tSZ effect in galaxy groups and clusters corresponding to $y \simeq 2\times10^{-6}$ [234]. These sources would constitute a strong foreground to the pre-recombination y-distortion [256]. In principle, it might be possible to distinguish the pre-recombination y-distortion from reionization signal using spatial information (e.g. [242, 243]) but it would be a challenge.

5.4 Conclusion

The large-scale behaviour of dark matter has been well established by a range of cosmological observables such as CMB anisotropies and clustering of galaxies. However, there remain issues with this model at small scales, and the nature of the dominant fraction of dark matter in the universe remains a mystery.

The evolution of spectral distortion in the pre-recombination era allows us to study scales in the range $10^4\,\mathrm{Mpc}^{-1} < k < 0.3\,\mathrm{Mpc}^{-1}$ as density perturbations at these scale decay and leave observable signatures on CMB spectrum. These perturbations are in the linear regime of their growth in the pre-recombination and therefore can be theoretically modelled very accurately.

We consider four alternative dark matter models which give significant deviations of small-scale power as compared to the ΛCDM model and study the spectral distortion of CMB owing

to SD for these models. These models are motivated by different aspects of physics in the early universe: phase transition (LFDM), free-streaming of massive particles (WDM), the decay of massive charged particles(CHDM), and dynamics of a scalar field with nonzero effective mass (ULA).

We show that main impact of the models we consider is to alter the late time spectral distortion history by lowering the y-parameter by a few percent for an acceptable range of parameters for these models (Table 5.1).

In this work, we only consider models that leave invariant the MRE. This excludes models such as decaying dark matter particles that create relativistic decay products thereby delaying the MRE epoch (e.g. [257, 258]). We also excluded models that are based on extra relativistic degrees of freedom (for details see [55] and references therein) or are based on a change in initial conditions (e.g. [259, 260]).

Our analysis suggests that all class of models that give suppression of power as compared to the ΛCDM model should result in late time spectral distortion. In section 5.2 we present general arguments which show that the change in spectral distortion is dominated by the evolution of potential after the scale enters the horizon. This effect scales as the ratio of energy densities of dark matter and radiation $\rho_{\rm dm}/\rho_r$ and is negligible at early times. This might also allow one to distinguish the impact of modifying the initial matter power spectrum on CMB spectral distortion from a change in the dark matter model that affects the matter power at small scales, as the former would cause all the three forms of CMB distortions while the latter would not.

Future experiments such as PIXIE and CMB-S4 have the potential to establish the nature of dark matter (e.g. [255]) by unprecedented improvement in mapping the CMB spectral and spatial structures. Our work is one step in that direction and points out the challenges involved in such an endeavour.

Chapter 6

Conclusions and Outlooks

In this thesis, by motivating the need for finding out an alternative candidate for WIMP that can reduce the small-scale power, we have presented how the small-scale power suppression can affect some of the important observables of the universe. In this chapter, we provide a comprehensive overview of the results that were presented in the last three chapters. We also briefly discuss the detectability of these effects by future experiments. We end this chapter by providing some future directions of research that can be followed to have a better understanding of the fundamental nature of dark matter and the way it affects the observable universe.

6.1 Conclusions

The precise particle nature of dark matter is still buried in mystery even after decades of research and experiments. However, at present it is well established that not only it does exist, it is the most dominating matter candidate and the key controlling factor in the structure formation of the universe. The standard WIMP CDM can explain the large-scale behaviors of the structures of the universe accurately, though it fails to explain the observed phenomena at small scale, i.e., scales corresponding galaxies and groups of galaxies. Suppressing the power at small scale is one of the many ways to address the small-scale issues, as explained in Chapter 1. The lighter version of CDM, the WDM is considered by many pioneering works as two potential remedies of the small-scale problems, producing conflicting results. Thus, a whole new candidate should come into play, which simultaneously solves the small-scale problems and reproduces the large-scale feature of structures in the CDM paradigm.

In Chapter 3, we have considered the LFDM model and studied its effects on matter power spectrum at both large scales i.e., $k \simeq 0.01 - 0.2\,\mathrm{hMpc}^{-1}$ and small scales i.e., $k \simeq 0.2 - 4.8\,\mathrm{hMpc}^{-1}$. The two major model parameters of LFDM are the effective neutrino DOF $N_{\rm eff}$ and the redshift of formation of dark matter z_f with z_f having a more profound effect on the matter power spectrum. We have found that dark matter should form at $z_f \gtrsim 1.38 \times 10^5$ from the SDSS data, while the Lyman-α data provide tighter constraint on z_f to be $\gtrsim 1.25 \times 10^6$, both at 95% CL and after marginalizing over the normalization and $N_{\rm eff}$. We have also considered a scenario where a part of the total dark matter density is LFDM instead of the entire dark matter. Interestingly, from the Lyman-α data we have found that a scenario where LFDM contains $\sim 30\%$ of the total dark matter provides a better fit to data than ΛCDM and the formation can be allowed to happen as late as $z_f \simeq 10^5$.

In Chapter 4, we have explored the influence of small-scale power suppression on the EoR. Along with LFDM, we have included ULADM in this work. For both of the candidates, the HI power spectrum is enhanced by a factor of $2-10$ due to small-scale power suppression, for a fixed ionization fraction. The main effects of small-scale power suppression for any of the dark matter candidate are to increase the sizes of the ionized regions but simultaneously making them fewer in number, compared to ΛCDM. The density contrast of the neutral regions is also higher than the ΛCDM model. To constrain the dark matter parameters, we have discarded those models where either no halo is formed in the simulation box to host ionizing sources, or an absurdly high number of ionizing photons is necessary to make $x_{\rm HI} = 0.5$at $z = 8$. We have found that to meet the above criteria, the generic bounds on the dark matter parameters are: $z_f > 4 \times 10^5$ and $m_a > 2.6 \times 10^{-23}$ eV. These constraints are in agreement with previous works.

We have also explored how the new dark matter candidates influence the evolution of collapsed fraction of baryon in the DLAs, in the redshift range of $2 < z < 5$. From observational data of the collapsed gas density Ω_g at several redshifts, we have derived the corresponding collapsed fraction of gas and used them to compare our theoretical predictions. We have discarded the models which cannot produce the reconstructed collapsed fraction at high redshift ($z \geq 3.5$), concluding that the formation redshift of LFDM and the mass of ULADM must follow the constraints(albeit weaker than the previous one): $z_f > 2 \times 10^5$ and $m_a > 10^{-23}$ eV. It should be noted that the observed luminosity functions of high redshift galaxies in the redshift range $z \sim 7 - 8$ are also expected to yield similar constraints.

In Chapter 5, we have investigated whether the small-scale power suppression can influence the spectral distortion in the CMB. In this chapter, we have included all the alternative dark matter candidates described in the Chapter 2, along with thermally produced WDM. We have worked out the amount of heating due to Silk Damping, the distortion parameter and the distorted CMB spectrum for all dark matter candidates including CDM and found that the y-parameter is on the order of 10^{-9}. Our study revealed that unless the structure formation constraints on the dark matter found earlier in this work are broken, the change in the y-distortion parameter is as small as 14 %, with same spectral nature that is produced by the standard ΛCDM model. Moreover, due to radiation domination in the early universe, the μ- and the i-distortions which have different spectral nature than the y-distortion, are not affected by the change in dark matter physics. To make things even worse, the small-scale parameters of the power spectrum, i.e., the amplitude and the spectral index, are themselves are not well constrained. Hence, the change in y-parameter due to the properties of dark matter can easily be degenerate with the inflationary properties of the power spectrum itself. The late-time radiative phenomena can also give rise to y-distortion with same spectral nature but with orders of magnitude higher y-parameter(For example, for tSZ effect in clusters $y \simeq 2 \times 10^{-6}$) than SD. Thus, the changes due to small-scale power suppression will be completely masked by the late-time phenomena, making them hard to identify and determine.

Finally, we conclude that the small-scale suppression of dark matter, being promising to solve the small-scale issues of ΛCDM, can have visible signatures on other universal phenomena. However, it is also worth conveying that most of the phenomena themselves are not very well understood and current knowledge about them is highly model dependent. Thus the changes brought by dark matter properties can have a high amount of degeneracy with other parameters and in some case(Spectral Distortion) the effects will be so small that they will be masked by other astrophysical and cosmological foregrounds. Hence, better theoretical understanding of the evolution of the universe and more sophisticated instruments are mandatory to say something definitive about the nature of dark matter.

6.2 Future Directions

In the previous section, we have described some possible astrophysical probes of the nature of dark matter. Further studies can be performed the enrich the knowledge about dark matter and put better constraints on its properties.

As described in Chapter 1 the strong and weak gravitational lensing are useful probes of dark matter distribution in galaxy clusters. Recently, direct gravitational imaging of mass substructures [261, 262] has opened a new avenue to study the small-scale distribution of the dark matter. The abundance and distribution of dark matter in galaxy clusters are crucially dependent on the underlying mass function and hence the power spectrum. Therefore, modification of power spectrum will be reflected in the map of dark matter extracted using lensing. Simulating the dark matter distribution in galaxy clusters with different dark matter candidates and comparing them with observational data will be another messenger about the nature of dark matter. Furthermore, with high-resolution simulation, it will also be possible to break the degeneracy between the inflationary parameters and dark matter parameters up to a certain scale.

In a recent work [263], it is shown that using a detector that includes a semiconductor material, a dark matter candidate with a mass above order of the bandgap energy of the semiconductor can be detected. The average bandgap energy of a semiconductor can be O(1 eV). Dark matter particles with mass O(10 eV) interact with the semiconductor material via inelastic scattering and also produces athermal photon emission. It will thus be interesting to verify whether a dark matter with mass O(10 eV) can be cosmologically accommodated or not. A different non-thermal production is a must to produce such a light mass dark matter which can meet structure formation and CMB constraints. An MCMC analysis with this new dark matter candidate with other cosmological parameters will be necessary to establish it as a likely candidate and also to put constraints on its properties.

Another interesting probe of this light dark matter candidate is the CMB spectral distortion. In Section 2.1 of Chapter 2, we have discussed the Fermionic LFDM candidate, where massless neutrinos get trapped into nuggets to form dark matter. The formation of nuggets happen by a fifth force, and it is assumed to happen instantaneously. This instantaneous formation can produce some entropy and depending on the epoch of dark matter formation; it can lead to different type of spectral distortion. A study of the distortion parameter and the distorted

spectrum can put an independent constraint on the mass and redshift of formation of the light dark matter candidate.

Bibliography

[1] S. Das and N. Weiner, *Late Forming Dark Matter in Theories of Neutrino Dark Energy*, *Phys. Rev.* **D84** (2011) 123511, [astro-ph/0611353].

[2] D. J. E. Marsh and P. G. Ferreira, *Ultra-Light Scalar Fields and the Growth of Structure in the Universe*, *Phys. Rev.D.* **D82** (2010) 103528, [arXiv:1009.3501].

[3] K. Sigurdson and M. Kamionkowski, *Charged - particle decay and suppression of small - scale power*, *Phys. Rev. Lett.* **92** (2004) 171302, [astro-ph/0311486].

[4] A. Sarkar, S. Das, and S. K. Sethi, *How Late can the Dark Matter form in our universe?*, *JCAP* **1503** (2015), no. 03 004, [arXiv:1410.7129].

[5] B. A. Reid, W. J. Percival, D. J. Eisenstein, L. Verde, D. N. Spergel, et al., *Cosmological Constraints from the Clustering of the Sloan Digital Sky Survey DR7 Luminous Red Galaxies*, *Mon.Not.Roy.Astron.Soc.* **404** (2010) 60–85, [arXiv:0907.1659].

[6] R. A. Croft, D. H. Weinberg, M. Bolte, S. Burles, L. Hernquist, et al., *Towards a precise measurement of matter clustering: Lyman alpha forest data at redshifts 2-4*, *Astrophys.J.* **581** (2002) 20–52, [astro-ph/0012324].

[7] M. Tegmark and M. Zaldarriaga, *Separating the early universe from the late universe: Cosmological parameter estimation beyond the black box*, *Phys.Rev.* **D66** (2002) 103508, [astro-ph/0207047].

[8] A. Sarkar, R. Mondal, S. Das, S. Sethi, S. Bharadwaj, and D. J. E. Marsh, *The effects of the small-scale DM power on the cosmological neutral hydrogen (HI) distribution at high redshifts*, *JCAP* **1604** (2016), no. 04 012, [arXiv:1512.03325].

[9] D. J. E. Marsh and J. Silk, *A Model For Halo Formation With Axion Mixed Dark Matter*, *Mon. Not. Roy. Astron. Soc.* **437** (2014), no. 3 2652–2663, [arXiv:1307.1705].

[10] P. Noterdaeme et al., *Column density distribution and cosmological mass density of neutral gas: Sloan Digital Sky Survey-III Data Release 9*, *Astron. Astrophys.* **547** (2012) L1, [arXiv:1210.1213].

[11] T. Zafar, C. Peroux, A. Popping, B. Milliard, J.-M. Deharveng, and S. Frank, *The ESO UVES Advanced Data Products Quasar Sample - II. Cosmological Evolution of the Neutral Gas Mass Density*, *Astron. Astrophys.* **556** (2013) A141, [arXiv:1307.0602].

[12] A. Sarkar, S. K. Sethi, and S. Das, *The effects of the small-scale behaviour of dark matter power spectrum on CMB spectral distortion*, arXiv:1701.07273.

[13] J. C. Kapteyn, *First Attempt at a Theory of the Arrangement and Motion of the Sidereal System*, *Astrophys. J.* **55** (May, 1922) 302.

[14] J. H. Oort, *The force exerted by the stellar system in the direction perpendicular to the galactic plane and some related problems*, *Bull. Astron. Inst. Netherlands* **6** (Aug., 1932) 249.

[15] F. Zwicky, *Die Rotverschiebung von extragalaktischen Nebeln*, *Helvetica Physica Acta* **6** (1933) 110–127.

[16] H. W. Babcock, *The rotation of the Andromeda Nebula*, *Lick Observatory Bulletin* **19** (1939) 41–51.

[17] F. D. Kahn and L. Woltjer, *Intergalactic Matter and the Galaxy.*, *Astrophys. J.* **130** (Nov., 1959) 705.

[18] V. C. Rubin and W. K. Ford, Jr., *Rotation of the Andromeda Nebula from a Spectroscopic Survey of Emission Regions*, *Astrophys. J.* **159** (Feb., 1970) 379.

[19] M. S. Roberts and R. N. Whitehurst, *The rotation curve and geometry of M31 at large galactocentric distances.*, *Astrophys. J.* **201** (Oct., 1975) 327–346.

[20] V. C. Rubin, N. Thonnard, and W. K. Ford, Jr., *Extended rotation curves of high-luminosity spiral galaxies. IV - Systematic dynamical properties, SA through SC*, *Astrophys. J.l* **225** (Nov., 1978) L107–L111.

[21] J. Einasto, A. Kaasik, and E. Saar, *Dynamic evidence on massive coronas of galaxies*, *Nature* **250** (July, 1974) 309–310.

[22] J. P. Ostriker, P. J. E. Peebles, and A. Yahil, *The size and mass of galaxies, and the mass of the universe*, *Astrophys. J.l* **193** (Oct., 1974) L1–L4.

[23] J. P. Ostriker and P. J. E. Peebles, *A Numerical Study of the Stability of Flattened Galaxies: or, can Cold Galaxies Survive?*, *Astrophys. J.* **186** (Dec., 1973) 467–480.

[24] S. M. Faber and D. N. C. Lin, *Is there nonluminous matter in dwarf spheroidal galaxies*, *Astrophys. J.l* **266** (Mar., 1983) L17–L20.

[25] M. Aaronson and J. Mould, *A distance scale from the infrared magnitude/H I velocity-width relation. IV - The morphological type dependence and scatter in the relation; the distances to nearby groups*, *Astrophys. J.* **265** (Feb., 1983) 1–17.

[26] K. M. Ashman, *Dark matter in galaxies*, *PASP* **104** (Dec., 1992) 1109–1138.

[27] G. C. Stewart, A. C. Fabian, P. E. J. Nulsen, and C. R. Canizares, *The mass profile and gas content of M87*, *Astrophys. J.* **278** (Mar., 1984) 536–543.

[28] A. C. Fabian, P. A. Thomas, R. E. White, III, and S. M. Fall, *A lower limit to the binding mass of early-type galaxies*, *Mon. Not. R. Astron. Soc* **221** (Aug., 1986) 1049–1056.

[29] D. Mihalas and J. Binney, *Galactic astronomy: Structure and kinematics /2nd edition/.* "Princeton University Press", 1981.

[30] C. M. Carollo, P. T. de Zeeuw, R. P. van der Marel, I. J. Danziger, and E. E. Qian, *Dark matter in elliptical galaxies*, *Astrophys. J.l* **441** (Mar., 1995) L25–L28, [astro-ph/9501046].

[31] O. E. Gerhard, *Line-of-sight velocity profiles in spherical galaxies: breaking the degeneracy between anisotropy and mass.*, *Mon. Not. R. Astron. Soc* **265** (Nov., 1993) 213.

[32] T. Treu, *Strong Lensing by Galaxies*, *ARA&A* **48** (Sept., 2010) 87–125, [arXiv:1003.5567].

[33] N. Kaiser and G. Squires, *Mapping the dark matter with weak gravitational lensing*, *Astrophys. J.* **404** (Feb., 1993) 441–450.

[34] R. D. Blandford and R. Narayan, *Cosmological applications of gravitational lensing*, *ARA&A* **30** (1992) 311–358.

[35] S. Smith, *The Mass of the Virgo Cluster*, *Astrophys. J.* **83** (Jan., 1936) 23.

[36] F. Zwicky, *On the Masses of Nebulae and of Clusters of Nebulae*, *Astrophys. J.* **86** (Oct., 1937) 217.

[37] D. Walsh, R. F. Carswell, and R. J. Weymann, *0957 + 561 A, B - Twin quasistellar objects or gravitational lens*, *Nature* **279** (May, 1979) 381–384.

[38] G. Soucail, B. Fort, Y. Mellier, and J. P. Picat, *A blue ring-like structure, in the center of the A 370 cluster of galaxies*, *Astron. & Astrophys.* **172** (Jan., 1987) L14–L16.

[39] J. A. Tyson, F. Valdes, and R. A. Wenk, *Detection of systematic gravitational lens galaxy image alignments - Mapping dark matter in galaxy clusters*, *Astrophys. J.l* **349** (Jan., 1990) L1–L4.

[40] D. Clowe, M. Bradač, A. H. Gonzalez, M. Markevitch, S. W. Randall, C. Jones, and D. Zaritsky, *A Direct Empirical Proof of the Existence of Dark Matter*, *Astrophys. J.l* **648** (Sept., 2006) L109–L113, [astro-ph/0608407].

[41] M. Bartelmann and P. Schneider, *Weak gravitational lensing*, *Phys. Rep.* **340** (Jan., 2001) 291–472, [astro-ph/9912508].

[42] H. Hoekstra, M. Bartelmann, H. Dahle, H. Israel, M. Limousin, and M. Meneghetti, *Masses of galaxy clusters from gravitational lensing*, *Space Sci. Rev.* **177** (2013) 75–118, [arXiv:1303.3274].

[43] A. Lewis, A. Challinor, and A. Lasenby, *Efficient computation of CMB anisotropies in closed FRW models*, *Astrophys. J.* **538** (2000) 473–476, [astro-ph/9911177].

[44] C.-P. Ma and E. Bertschinger, *Cosmological perturbation theory in the synchronous and conformal Newtonian gauges*, *Astrophys.J.* **455** (1995) 7–25, [astro-ph/9506072].

[45] J. Silk, *Cosmic Black-Body Radiation and Galaxy Formation*, *Astrophys. J.* **151** (Feb., 1968) 459.

[46] **BOSS** Collaboration, F. Beutler et al., *The clustering of galaxies in the SDSS-III Baryon Oscillation Spectroscopic Survey: Testing gravity with redshift-space distortions using the power spectrum multipoles*, *Mon. Not. Roy. Astron. Soc.* **443** (2014), no. 2 1065–1089, [arXiv:1312.4611].

[47] S. S. Gershtein and Y. B. Zel'dovich, *Rest Mass of Muonic Neutrino and Cosmology*, *Soviet Journal of Experimental and Theoretical Physics Letters* **4** (Sept., 1966) 120–122.

[48] R. Cowsik and J. McClelland, *An upper limit on the neutrino rest mass*, *Phys. Rev. Lett.* **29** (Sep, 1972) 669–670.

[49] A. S. Szalay and G. Marx, *Neutrino rest mass from cosmology*, *"Astron. Astrophys."* **49** (June, 1976) 437–441.

[50] J. E. Gunn, B. W. Lee, I. Lerche, D. N. Schramm, and G. Steigman, *Some astrophysical consequences of the existence of a heavy stable neutral lepton*, *"Astrophys. J"* **223** (Aug., 1978) 1015–1031.

[51] J. R. Primack and G. R. Blumenthal, *What is the dark matter? - Implications for galaxy formation and particle physics*, in *NATO Advanced Science Institutes (ASI) Series C* (J. Audouze and J. Tran Thanh Van, eds.), vol. 117 of *NATO Advanced Science Institutes (ASI) Series C*, pp. 163–183, 1984.

[52] S. D. M. White, C. S. Frenk, and M. Davis, *Clustering in a neutrino-dominated universe*, *"ApJL"* **274** (Nov., 1983) L1–L5.

[53] D. J. Fixsen, E. S. Cheng, J. M. Gales, J. C. Mather, R. A. Shafer, and E. L. Wright, *The Cosmic Microwave Background spectrum from the full COBE FIRAS data set*, *Astrophys. J.* **473** (1996) 576, [astro-ph/9605054].

[54] D. J. Fixsen, E. S. Cheng, J. M. Gales, J. C. Mather, R. A. Shafer, and E. L. Wright, *The Cosmic Microwave Background Spectrum from the Full COBE FIRAS Data Set*, *Astrophys. J.* **473** (Dec., 1996) 576, [astro-ph/9605054].

[55] **Planck** Collaboration, P. A. R. Ade et al., *Planck 2015 results. XIII. Cosmological parameters*, *Astron. Astrophys.* **594** (2016) A13, [arXiv:1502.01589].

[56] M. Milgrom, *A modification of the Newtonian dynamics - Implications for galaxies*, *Astrophys. J.* **270** (July, 1983) 371–389.

[57] M. Milgrom, *A modification of the Newtonian dynamics as a possible alternative to the hidden mass hypothesis*, *Astrophys. J.* **270** (July, 1983) 365–370.

[58] K. Freese, *Death of baryonic dark matter*, *Phys. Rep.* **333** (Aug., 2000) 183–201.

[59] D. Pfenniger, F. Combes, and L. Martinet, *Is dark matter in spiral galaxies cold gas? I. Observational constraints and dynamical clues about galaxy evolution*, *Astron. & Astrophys.* **285** (May, 1994) 79–93, [astro-ph/9311043].

[60] D. Pfenniger and F. Combes, *Is dark matter in spiral galaxies cold gas? II. Fractal models and star non-formation*, *Astron. & Astrophys.* **285** (May, 1994) 94–118, [astro-ph/9311044].

[61] C. Alcock, R. A. Allsman, D. R. Alves, T. S. Axelrod, A. C. Becker, D. P. Bennett, K. H. Cook, A. J. Drake, K. C. Freeman, M. Geha, K. Griest, M. J. Lehner, S. L. Marshall, D. Minniti, C. A. Nelson, B. A. Peterson, P. Popowski, M. R. Pratt, P. J. Quinn, C. W. Stubbs, W. Sutherland, A. B. Tomaney, T. Vandehei, D. L. Welch, and MACHO Collaboration, *The MACHO Project: Microlensing Optical Depth toward the Galactic Bulge from Difference Image Analysis*, *Astrophys. J.* **541** (Oct., 2000) 734–766, [astro-ph/0002510].

[62] C. Alcock, R. A. Allsman, D. R. Alves, T. S. Axelrod, A. C. Becker, D. P. Bennett, K. H. Cook, N. Dalal, A. J. Drake, K. C. Freeman, M. Geha, K. Griest, M. J. Lehner, S. L. Marshall, D. Minniti, C. A. Nelson, B. A. Peterson, P. Popowski, M. R. Pratt, P. J. Quinn, C. W. Stubbs, W. Sutherland, A. B. Tomaney, T. Vandehei, and D. Welch,

The MACHO Project: Microlensing Results from 5.7 Years of Large Magellanic Cloud Observations, *Astrophys. J.* **542** (Oct., 2000) 281–307, [astro-ph/0001272].

[63] P. Tisserand, L. Le Guillou, C. Afonso, J. N. Albert, J. Andersen, R. Ansari, É. Aubourg, P. Bareyre, J. P. Beaulieu, X. Charlot, C. Coutures, R. Ferlet, P. Fouqué, J. F. Glicenstein, B. Goldman, A. Gould, D. Graff, M. Gros, J. Haissinski, C. Hamadache, J. de Kat, T. Lasserre, É. Lesquoy, C. Loup, C. Magneville, J. B. Marquette, É. Maurice, A. Maury, A. Milsztajn, M. Moniez, N. Palanque-Delabrouille, O. Perdereau, Y. R. Rahal, J. Rich, M. Spiro, A. Vidal-Madjar, L. Vigroux, S. Zylberajch, and EROS-2 Collaboration, *Limits on the Macho content of the Galactic Halo from the EROS-2 Survey of the Magellanic Clouds*, *Astron. & Astrophys.* **469** (July, 2007) 387–404, [astro-ph/0607207].

[64] G. Jungman, M. Kamionkowski, and K. Griest, *Supersymmetric dark matter*, *Phys. Rep.* **267** (Mar., 1996) 195–373, [hep-ph/9506380].

[65] M. Klasen, M. Pohl, and G. Sigl, *Indirect and direct search for dark matter*, *Progress in Particle and Nuclear Physics* **85** (Nov., 2015) 1–32, [arXiv:1507.03800].

[66] R. Foot, *Mirror matter-type dark matter*, *Int. J. Mod. Phys.* **D13** (2004) 2161–2192, [astro-ph/0407623].

[67] E. Witten, *Cosmic separation of phases*, *Phys. Rev. D* **30** (July, 1984) 272–285.

[68] H. Ziaeepour, *Quest for fats: Roles for a fat dark matter (WIMPZILLA)*, astro-ph/0406079.

[69] M. C. Bento, O. Bertolami, and A. A. Sen, *The Revival of the unified dark energy - dark matter model?*, *Phys. Rev.* **D70** (2004) 083519, [astro-ph/0407239].

[70] **SuperCDMS** Collaboration, R. Agnese et al., *Search for Low-Mass Weakly Interacting Massive Particles with SuperCDMS*, *Phys. Rev. Lett.* **112** (2014), no. 24 241302, [arXiv:1402.7137].

[71] **CoGeNT** Collaboration, C. E. Aalseth et al., *CoGeNT: A Search for Low-Mass Dark Matter using p-type Point Contact Germanium Detectors*, *Phys. Rev.* **D88** (2013) 012002, [arXiv:1208.5737].

[72] M. Bossa, *DarkSide-50, a background free experiment for dark matter searches*, *Journal of Instrumentation* **9** (Jan., 2014) C01034.

[73] **LUX** Collaboration, D. S. Akerib et al., *First results from the LUX dark matter experiment at the Sanford Underground Research Facility*, *Phys. Rev. Lett.* **112** (2014) 091303, [arXiv:1310.8214].

[74] R. Bernabei et al., *Final model independent result of DAMA/LIBRA-phase1*, *Eur. Phys. J.* **C73** (2013) 2648, [arXiv:1308.5109].

[75] **CRESST-II** Collaboration, G. Angloher et al., *Results on low mass WIMPs using an upgraded CRESST-II detector*, *Eur. Phys. J.* **C74** (2014), no. 12 3184, [arXiv:1407.3146].

[76] PandaX Collaboration, M. Xiao, X. Xiao, L. Zhao, X. Cao, X. Chen, Y. Chen, X. Cui, D. Fang, C. Fu, K. L. Giboni, H. Gong, G. Guo, J. Hu, X. Huang, X. Ji, Y. Ju, S. Lei, S. Li, Q. Lin, H. Liu, J. Liu, X. Liu, W. Lorenzon, Y. Ma, Y. Mao, K. Ni, K. Pushkin, X. Ren, M. Schubnell, M. Shen, S. Stephenson, A. Tan, G. Tarle, H. Wang, J. Wang, M. Wang, X. Wang, Z. Wang, Y. Wei, S. Wu, P. Xie, Y. You, X. Zeng, H. Zhang, T. Zhang, and Z. Zhu, *First dark matter search results from the PandaX-I experiment*, *ArXiv e-prints* (Aug., 2014) [arXiv:1408.5114].

[77] J. Menendez, D. Gazit, and A. Schwenk, *Spin-dependent WIMP scattering off nuclei*, *Phys. Rev.* **D86** (2012) 103511, [arXiv:1208.1094].

[78] P. Cushman et al., *Working Group Report: WIMP Dark Matter Direct Detection*, in *Proceedings, 2013 Community Summer Study on the Future of U.S. Particle Physics: Snowmass on the Mississippi (CSS2013): Minneapolis, MN, USA, July 29-August 6, 2013*, 2013. arXiv:1310.8327.

[79] **XENON100** Collaboration, E. Aprile et al., *Limits on spin-dependent WIMP-nucleon cross sections from 225 live days of XENON100 data*, *Phys. Rev. Lett.* **111** (2013), no. 2 021301, [arXiv:1301.6620].

[80] **PAMELA** Collaboration, O. Adriani et al., *An anomalous positron abundance in cosmic rays with energies 1.5-100 GeV*, *Nature* **458** (2009) 607–609, [arXiv:0810.4995].

[81] **H.E.S.S.** Collaboration, F. Aharonian et al., *H.E.S.S. observations of the Galactic Center region and their possible dark matter interpretation*, *Phys. Rev. Lett.* **97** (2006) 221102, [astro-ph/0610509]. [Erratum: Phys. Rev. Lett.97,249901(2006)].

[82] P. Jean et al., *Early SPI / INTEGRAL measurements of 511 keV line emission from the 4th quadrant of the Galaxy*, *Astron. Astrophys.* **407** (2003) L55, [astro-ph/0309484].

[83] W. J. G. de Blok, *The Core-Cusp Problem*, *Adv. Astron.* **2010** (2010) 789293, [arXiv:0910.3538].

[84] J. F. Navarro, C. S. Frenk, and S. D. M. White, *The Structure of cold dark matter halos*, *Astrophys. J.* **462** (1996) 563–575, [astro-ph/9508025].

[85] A. A. Klypin, A. V. Kravtsov, O. Valenzuela, and F. Prada, *Where are the missing Galactic satellites?*, *Astrophys. J.* **522** (1999) 82–92, [astro-ph/9901240].

[86] B. Moore, S. Ghigna, F. Governato, G. Lake, T. R. Quinn, J. Stadel, and P. Tozzi, *Dark matter substructure within galactic halos*, *Astrophys. J.* **524** (1999) L19–L22, [astro-ph/9907411].

[87] S. Garrison-Kimmel, M. Boylan-Kolchin, J. S. Bullock, and E. N. Kirby, *Too Big to Fail in the Local Group*, *Mon. Not. Roy. Astron. Soc.* **444** (2014), no. 1 222–236, [arXiv:1404.5313].

[88] M. Boylan-Kolchin, J. S. Bullock, and M. Kaplinghat, *Too big to fail? The puzzling darkness of massive Milky Way subhaloes*, *Mon. Not. Roy. Astron. Soc.* **415** (2011) L40, [arXiv:1103.0007].

[89] J. Dubinski and R. G. Carlberg, *The Structure of cold dark matter halos*, *Astrophys. J.* **378** (1991) 496.

[90] J. S. Bullock, T. S. Kolatt, Y. Sigad, R. S. Somerville, A. V. Kravtsov, A. A. Klypin, J. R. Primack, and A. Dekel, *Profiles of dark haloes: evolution, scatter and environment*, *Mon. Not. R. Astron. Soc* **321** (Mar., 2001) 559–575, [astro-ph/9908159].

[91] B. Moore, T. R. Quinn, F. Governato, J. Stadel, and G. Lake, *Cold collapse and the core catastrophe*, *Mon. Not. Roy. Astron. Soc.* **310** (1999) 1147–1152, [astro-ph/9903164].

[92] J. E. Taylor and J. F. Navarro, *The Phase - space density profiles of cold dark matter halos*, *Astrophys. J.* **563** (2001) 483–488, [astro-ph/0104002].

[93] J. Diemand, M. Zemp, B. Moore, J. Stadel, and C. M. Carollo, *Cusps in cold dark matter haloes*, *Mon. Not. R. Astron. Soc* **364** (Dec., 2005) 665–673, [astro-ph/0504215].

[94] J. Stadel, D. Potter, B. Moore, J. Diemand, P. Madau, M. Zemp, M. Kuhlen, and V. Quilis, *Quantifying the heart of darkness with GHALO - a multi-billion particle simulation of our galactic halo*, *Mon. Not. Roy. Astron. Soc.* **398** (2009) L21–L25, [arXiv:0808.2981].

[95] B. Moore, *Evidence against dissipationless dark matter from observations of galaxy haloes*, *Nature* **370** (1994) 629.

[96] R. A. Flores and J. R. Primack, *Observational and theoretical constraints on singular dark matter halos*, *Astrophys. J.* **427** (1994) L1–4, [astro-ph/9402004].

[97] M. A. Zwaan, J. M. van der Hulst, W. J. G. de Blok, and S. S. McGaugh, *The Tully-Fisher relation for low surface brightness galaxies - Implications for galaxy evolution*, *Mon. Not. Roy. Astron. Soc.* **273** (1995) L35, [astro-ph/9501102].

[98] W. J. G. de Blok, S. S. McGaugh, and J. M. van der Hulst, *HI observations of low surface brightness galaxies: probing low-density galaxies*, *Mon. Not. R. Astron. Soc* **283** (Nov., 1996) 18–54, [astro-ph/9605069].

[99] S. S. McGaugh and W. J. G. de Blok, *Testing the Dark Matter Hypothesis with Low Surface Brightness Galaxies and Other Evidence*, *Astrophys. J.* **499** (May, 1998) 41–65, [astro-ph/9801123].

[100] W. J. G. de Blok and S. S. McGaugh, *The dark and visible matter content of low surface brightness disc galaxies*, *Mon. Not. R. Astron. Soc* **290** (Sept., 1997) 533–552, [astro-ph/9704274].

[101] F. C. van den Bosch and R. A. Swaters, *Dwarf galaxy rotation curves and the core problem of dark matter haloes*, *Mon. Not. R. Astron. Soc* **325** (Aug., 2001) 1017–1038, [astro-ph/0006048].

[102] F. C. van den Bosch, B. E. Robertson, J. J. Dalcanton, and W. J. G. de Blok, *Constraints on the Structure of Dark Matter Halos from the Rotation Curves of Low Surface Brightness Galaxies*, *Astron. J.* **119** (Apr., 2000) 1579–1591, [astro-ph/9911372].

[103] R. A. Swaters, B. F. Madore, and M. Trewhella, *High-Resolution Rotation Curves of Low Surface Brightness Galaxies*, *Astrophys. J.l* **531** (Mar., 2000) L107–L110, [astro-ph/0001277].

[104] W. J. G. de Blok and A. Bosma, *High-resolution rotation curves of low surface brightness galaxies*, *Astron. & Astrophys.* **385** (Apr., 2002) 816–846, [astro-ph/0201276].

[105] W. J. G. de Blok, S. S. McGaugh, A. Bosma, and V. C. Rubin, *Mass Density Profiles of Low Surface Brightness Galaxies*, *Astrophys. J.l* **552** (May, 2001) L23–L26, [astro-ph/0103102].

[106] G. Kauffmann, S. D. M. White, and B. Guiderdoni, *The Formation and Evolution of Galaxies Within Merging Dark Matter Haloes*, *Mon. Not. Roy. Astron. Soc.* **264** (1993) 201.

[107] A. Vale and J. P. Ostriker, *Linking halo mass to galaxy luminosity*, *Mon. Not. Roy. Astron. Soc.* **353** (2004) 189, [astro-ph/0402500].

[108] M. S. Pawlowski, B. Famaey, D. Merritt, and P. Kroupa, *On the persistence of two small-scale problems in ΛCDM*, *Astrophys. J.* **815** (2015), no. 1 19, [arXiv:1510.08060].

[109] J. F. Navarro, V. R. Eke, and C. S. Frenk, *The cores of dwarf galaxy haloes*, *Mon. Not. R. Astron. Soc* **283** (Dec., 1996) L72–L78, [astro-ph/9610187].

[110] G. Ogiya and M. Mori, *The Core-Cusp Problem in Cold Dark Matter Halos and Supernova Feedback: Effects of Oscillation*, *Astrophys. J.* **793** (Sept., 2014) 46, [arXiv:1206.5412].

[111] A. Pontzen and F. Governato, *How supernova feedback turns dark matter cusps into cores*, *Mon. Not. R. Astron. Soc* **421** (Apr., 2012) 3464–3471, [arXiv:1106.0499].

[112] S. Mashchenko, J. Wadsley, and H. M. P. Couchman, *Stellar Feedback in Dwarf Galaxy Formation*, *Science* **319** (Jan., 2008) 174, [arXiv:0711.4803].

[113] T. Quinn, N. Katz, and G. Efstathiou, *Photoionization and the formation of dwarf galaxies*, *Mon. Not. R. Astron. Soc* **278** (Feb., 1996) L49–L54, [astro-ph/9509128].

[114] R. Barkana and A. Loeb, *The Photoevaporation of Dwarf Galaxies during Reionization*, *Astrophys. J.* **523** (Sept., 1999) 54–65, [astro-ph/9901114].

[115] J. S. Bullock, A. V. Kravtsov, and D. H. Weinberg, *Reionization and the Abundance of Galactic Satellites*, *Astrophys. J.* **539** (Aug., 2000) 517–521, [astro-ph/0002214].

[116] L. Mayer, S. Kazantzidis, C. Mastropietro, and J. Wadsley, *Early gas stripping as the origin of the darkest galaxies in the Universe*, *Nature* **445** (Feb., 2007) 738–740, [astro-ph/0702495].

[117] W. H. Press and P. Schechter, *Formation of Galaxies and Clusters of Galaxies by Self-Similar Gravitational Condensation*, *Astrophys. J.* **187** (Feb., 1974) 425–438.

[118] M. Tomozeiu, L. Mayer, and T. Quinn, *Tidal Stirring of Satellites with Shallow Density Profiles Prevents Them from Being Too Big to Fail*, *Astrophys. J.l* **827** (Aug., 2016) L15, [arXiv:1605.00004].

[119] R. Verbeke, E. Papastergis, A. A. Ponomareva, S. Rathi, and S. De Rijcke, *A new astrophysical solution to the Too Big To Fail problem - Insights from the MoRIA simulations*, arXiv:1703.03810.

[120] J. I. Read, M. I. Wilkinson, N. W. Evans, G. Gilmore, and J. T. Kleyna, *The importance of tides for the local group dwarf spheroidals*, *Mon. Not. Roy. Astron. Soc.* **367** (2006) 387–399, [astro-ph/0511759].

[121] C. S. Frenk and S. D. M. White, *Dark matter and cosmic structure*, *Annalen Phys.* **524** (2012) 507–534, [arXiv:1210.0544].

[122] A. Boyarsky, O. Ruchayskiy, D. Iakubovskyi, and J. Franse, *Unidentified Line in X-Ray Spectra of the Andromeda Galaxy and Perseus Galaxy Cluster*, *Phys. Rev. Lett.* **113** (2014) 251301, [arXiv:1402.4119].

[123] S. Dodelson and L. M. Widrow, *Sterile-neutrinos as dark matter*, *Phys. Rev. Lett.* **72** (1994) 17–20, [hep-ph/9303287].

[124] S. Colombi, S. Dodelson, and L. M. Widrow, *Large scale structure tests of warm dark matter*, *Astrophys. J.* **458** (1996) 1, [astro-ph/9505029].

[125] X.-D. Shi and G. M. Fuller, *A New dark matter candidate: Nonthermal sterile neutrinos*, *Phys. Rev. Lett.* **82** (1999) 2832–2835, [astro-ph/9810076].

[126] P. Bode, J. P. Ostriker, and N. Turok, *Halo formation in warm dark matter models*, *Astrophys. J.* **556** (2001) 93–107, [astro-ph/0010389].

[127] M. Viel, J. Lesgourgues, M. G. Haehnelt, S. Matarrese, and A. Riotto, *Constraining warm dark matter candidates including sterile neutrinos and light gravitinos with WMAP and the Lyman-alpha forest*, *Phys.Rev.* **D71** (2005) 063534, [astro-ph/0501562].

[128] P. Colin, V. Avila-Reese, and O. Valenzuela, *Substructure and halo density profiles in a warm dark matter cosmology*, *Astrophys. J.* **542** (2000) 622–630, [astro-ph/0004115].

[129] M. Viel, G. D. Becker, J. S. Bolton, and M. G. Haehnelt, *Warm dark matter as a solution to the small scale crisis: New constraints from high redshift Lyman-α forest data*, *Phys.Rev.* **D88** (2013) 043502, [arXiv:1306.2314].

[130] J. Baur, N. Palanque-Delabrouille, C. Yèche, C. Magneville, and M. Viel, *Lyman-alpha Forests cool Warm Dark Matter*, *JCAP* **1608** (2016), no. 08 012, [arXiv:1512.01981].

[131] A. V. Maccio, S. Paduroiu, D. Anderhalden, A. Schneider, and B. Moore, *Cores in warm dark matter haloes: a Catch 22 problem*, *Mon. Not. Roy. Astron. Soc.* **424** (2012) 1105–1112, [arXiv:1202.1282].

[132] E. Polisensky and M. Ricotti, *Constraints on the Dark Matter Particle Mass from the Number of Milky Way Satellites*, *Phys. Rev.* **D83** (2011) 043506, [arXiv:1004.1459].

[133] M. R. Lovell, V. Eke, C. S. Frenk, L. Gao, A. Jenkins, T. Theuns, J. Wang, D. M. White, A. Boyarsky, and O. Ruchayskiy, *The Haloes of Bright Satellite Galaxies in a Warm Dark Matter Universe*, *Mon. Not. Roy. Astron. Soc.* **420** (2012) 2318–2324, [arXiv:1104.2929].

[134] D. J. E. Marsh, *Axion Cosmology*, *Phys. Rept.* **643** (2016) 1–79, [arXiv:1510.07633].

[135] A. D. Linde, *Hybrid inflation*, *Phys. Rev.* **D49** (1994) 748–754, [astro-ph/9307002].

[136] R. Fardon, A. E. Nelson, and N. Weiner, *Supersymmetric theories of neutrino dark energy*, *JHEP* **03** (2006) 042, [hep-ph/0507235].

[137] N. Afshordi, M. Zaldarriaga, and K. Kohri, *On the stability of dark energy with mass-varying neutrinos*, *Phys. Rev.* **D72** (2005) 065024, [astro-ph/0506663].

[138] S. Das, *Sterile neutrino, hidden dark matter and their cosmological signatures*, *J. Phys. Conf. Ser.* **405** (2012) 012011.

[139] N. Brouzakis and N. Tetradis, *Static configurations of dark energy and dark matter*, *JCAP* **0601** (2006) 004, [astro-ph/0509755].

[140] G. Mangano and P. D. Serpico, *A robust upper limit on $N_{\rm eff}$ from BBN, circa 2011*, *Phys.Lett.* **B701** (2011) 296–299, [arXiv:1103.1261].

[141] J. Lesgourgues, G. Mangano, G. Miele, and S. Pastor, *Neutrino Cosmology*. Cambridge University Press, Cambridge U.K., 2013.

[142] A. Arvanitaki, S. Dimopoulos, S. Dubovsky, N. Kaloper, and J. March-Russell, *String Axiverse*, *Phys. Rev.* **D81** (2010) 123530, [arXiv:0905.4720].

[143] W. Hu, R. Barkana, and A. Gruzinov, *Cold and fuzzy dark matter*, *Phys. Rev. Lett.* **85** (2000) 1158–1161, [astro-ph/0003365].

[144] L. Amendola and R. Barbieri, *Dark matter from an ultra-light pseudo-Goldsone-boson*, *Phys. Lett.* **B642** (2006) 192–196, [hep-ph/0509257].

[145] R. Hlozek, D. Grin, D. J. E. Marsh, and P. G. Ferreira, *A search for ultralight axions using precision cosmological data*, *Phys. Rev.* **D91** (2015), no. 10 103512, [arXiv:1410.2896].

[146] D. J. E. Marsh and A.-R. Pop, *Axion dark matter, solitons and the cusp-core problem*, *Mon. Not. Roy. Astron. Soc.* **451** (2015), no. 3 2479–2492, [arXiv:1502.03456].

[147] S. Profumo, K. Sigurdson, P. Ullio, and M. Kamionkowski, *A Running spectral index in supersymmetric dark-matter models with quasi-stable charged particles*, *Phys. Rev.* **D71** (2005) 023518, [astro-ph/0410714].

[148] K. Kohri and T. Takahashi, *Cosmology with Long-Lived Charged Massive Particles*, *Phys. Lett.* **B682** (2010) 337–341, [arXiv:0909.4610].

[149] A. Kamada, K. Kohri, T. Takahashi, and N. Yoshida, *Effects of electrically charged dark matter on cosmic microwave background anisotropies*, arXiv:1604.07926.

[150] P. Peebles and J. Yu, *Primeval adiabatic perturbation in an expanding universe*, *Astrophys.J.* **162** (1970) 815–836.

[151] **VIRGO Consortium** Collaboration, R. E. Smith, J. A. Peacock, A. Jenkins, S. D. M. White, C. S. Frenk, F. R. Pearce, P. A. Thomas, G. Efstathiou, and H. M. P. Couchmann, *Stable clustering, the halo model and nonlinear cosmological power spectra*, *Mon. Not. Roy. Astron. Soc.* **341** (2003) 1311, [astro-ph/0207664].

[152] N. Y. Gnedin and A. J. Hamilton, *Matter power spectrum from the Lyman-alpha forest: Myth or reality?*, *Mon.Not.Roy.Astron.Soc.* **334** (2002) 107–116, [astro-ph/0111194].

[153] D. Parkinson et al., *The WiggleZ Dark Energy Survey: Final data release and cosmological results*, *Phys. Rev.* **D86** (2012) 103518, [arXiv:1210.2130].

[154] C. Heymans et al., *CFHTLenS tomographic weak lensing cosmological parameter constraints: Mitigating the impact of intrinsic galaxy alignments*, *Mon. Not. Roy. Astron. Soc.* **432** (2013) 2433, [arXiv:1303.1808].

[155] **SDSS Collaboration** Collaboration, P. McDonald et al., *The Linear theory power spectrum from the Lyman-alpha forest in the Sloan Digital Sky Survey*, *Astrophys.J.* **635** (2005) 761–783, [astro-ph/0407377].

[156] N. Palanque-Delabrouille, C. Yèche, A. Borde, J.-M. L. Goff, G. Rossi, et al., *The one-dimensional Ly-alpha forest power spectrum from BOSS*, *Astron.Astrophys. 559,* **A85** (2013) [arXiv:1306.5896].

[157] K. L. Pandey and S. K. Sethi, *Probing Primordial Magnetic Fields Using Ly-alpha Clouds*, *Astrophys. J.* **762** (2013) 15, [arXiv:1210.3298].

[158] R. Barkana and A. Loeb, *In the beginning: The First sources of light and the reionization of the Universe*, *Phys. Rept.* **349** (2001) 125–238, [astro-ph/0010468].

[159] A. Loeb and R. Barkana, *The Reionization of the Universe by the first stars and quasars*, *Ann. Rev. Astron. Astrophys.* **39** (2001) 19–66, [astro-ph/0010467].

[160] V. Bromm and R. B. Larson, *The First stars*, *Ann. Rev. Astron. Astrophys.* **42** (2004) 79–118, [astro-ph/0311019].

[161] S. Furlanetto, S. P. Oh, and F. Briggs, *Cosmology at Low Frequencies: The 21 cm Transition and the High-Redshift Universe*, *Phys. Rept.* **433** (2006) 181–301, [astro-ph/0608032].

[162] R. Barkana, *The First Stars in the Universe and Cosmic Reionization*, *Science* **313** (2006) 931=934, [astro-ph/0608450].

[163] P. Madau, A. Meiksin, and M. J. Rees, *21 Centimeter Tomography of the Intergalactic Medium at High Redshift*, *"Astrophys. J"* **475** (Feb., 1997) 429–444, [astro-ph/9608010].

[164] R. M. Thomas and S. Zaroubi, *Time-evolution of ionization and heating around first stars and miniquasars*, *Mon. Not. Roy. Astron. Soc.* **384** (2008) 1080, [arXiv:0709.1657].

[165] R. M. Thomas et al., *Fast Large-Scale Reionization Simulations*, *Mon. Not. Roy. Astron. Soc.* **393** (2009) 32, [arXiv:0809.1326].

[166] F. Fontanot, S. Cristiani, and E. Vanzella, *On the relative contribution of high-redshift galaxies and active galactic nuclei to reionization*, *"Mon. Not. Roy. Astron. Soc."* **425** (Sept., 2012) 1413–1420, [arXiv:1206.5810].

[167] M. McQuinn, *Constraints on X-ray emissions from the reionization era*, *"Mon. Not. Roy. Astron. Soc."* **426** (Oct., 2012) 1349–1360, [arXiv:1206.1335].

[168] S. Parsa, J. S. Dunlop, and R. J. McLure, *No evidence for a significant AGN contribution to cosmic hydrogen reionization*, arXiv:1704.07750.

[169] S. Zaroubi, *The Epoch of Reionization*, in *The First Galaxies* (T. Wiklind, B. Mobasher, and V. Bromm, eds.), vol. 396 of *Astrophysics and Space Science Library*, p. 45, 2013. arXiv:1206.0267.

[170] J. Oñorbe, J. F. Hennawi, Z. Lukić, and M. Walther, *Constraining Reionization with the $z \sim 5-6$ Lyman-α Forest Power Spectrum: the Outlook after Planck*, arXiv:1703.08633.

[171] J. S. Bolton, M. G. Haehnelt, S. J. Warren, P. C. Hewett, D. J. Mortlock, B. P. Venemans, R. G. McMahon, and C. Simpson, *How neutral is the intergalactic medium surrounding the redshift z=7.085 quasar ULAS J1120+0641?*, *Mon. Not. Roy. Astron. Soc.* **416** (2011) L70, [arXiv:1106.6089].

[172] D. J. Mortlock, S. J. Warren, B. P. Venemans, M. Patel, P. C. Hewett, R. G. McMahon, C. Simpson, T. Theuns, E. A. Gonzáles-Solares, A. Adamson, S. Dye, N. C. Hambly, P. Hirst, M. J. Irwin, E. Kuiper, A. Lawrence, and H. J. A. Röttgering, *A luminous quasar at a redshift of z = 7.085*, *"Nature"* **474** (June, 2011) 616–619, [arXiv:1106.6088].

[173] P. J. E. Peebles and J. T. Yu, *Primeval Adiabatic Perturbation in an Expanding Universe*, *Astron. Astrophys.* **162** (Dec., 1970) 815.

[174] **WMAP** Collaboration, D. N. Spergel et al., *Wilkinson Microwave Anisotropy Probe (WMAP) three year results: implications for cosmology*, *Astrophys. J. Suppl.* **170** (2007) 377, [astro-ph/0603449].

[175] **Planck** Collaboration, R. Adam et al., *Planck intermediate results. XLVII. Planck constraints on reionization history*, *Astron. Astrophys.* **596** (2016) A108, [arXiv:1605.03507].

[176] T. Theuns, J. Schaye, S. Zaroubi, T.-S. Kim, P. Tzanavaris, and B. Carswell, *Constraints on reionization from the thermal history of the intergalactic medium*, *Astrophys. J.* **567** (2002) L103, [astro-ph/0201514].

[177] R. J. Bouwens, G. D. Illingworth, I. Labbe, P. A. Oesch, M. Trenti, C. M. Carollo, P. G. van Dokkum, M. Franx, M. Stiavelli, V. González, D. Magee, and L. Bradley, *A*

candidate redshift z˜10 galaxy and rapid changes in that population at an age of 500Myr, *"Nature"* **469** (Jan., 2011) 504–507, [arXiv:0912.4263].

[178] J. S. Bolton and M. G. Haehnelt, *The observed ionization rate of the intergalactic medium and the ionizing emissivity at z¿=5: Evidence for a photon starved and extended epoch of reionization*, *Mon. Not. Roy. Astron. Soc.* **382** (2007) 325, [astro-ph/0703306].

[179] C. A. Muller and J. H. Oort, *Observation of a Line in the Galactic Radio Spectrum: The Interstellar Hydrogen Line at 1,420 Mc./sec., and an Estimate of Galactic Rotation*, *"Nature"* **168** (Sept., 1951) 357–358.

[180] H. I. Ewen and E. M. Purcell, *Observation of a Line in the Galactic Radio Spectrum: Radiation from Galactic Hydrogen at 1,420 Mc./sec.*, *"Nature"* **168** (Sept., 1951) 356.

[181] S. A. Wouthuysen, *On the excitation mechanism of the 21-cm (radio-frequency) interstellar hydrogen emission line.*, *"Astronom. J"* **57** (1952) 31–32.

[182] G. B. Field, *Excitation of the Hydrogen 21-CM Line*, *Proceedings of the IRE* **46** (Jan., 1958) 240–250.

[183] K. Wood and A. Loeb, *Escape of Ionizing Radiation from High-Redshift Galaxies*, *"Astrophys. J"* **545** (Dec., 2000) 86–99, [astro-ph/9911316].

[184] M. Ricotti and J. M. Shull, *Feedback from Galaxy Formation: Escaping Ionizing Radiation from Galaxies at High Redshift*, *"Astrophys. J"* **542** (Oct., 2000) 548–558, [astro-ph/9912006].

[185] B. Ciardi, S. Bianchi, and A. Ferrara, *Lyman continuum escape from inhomogeneous ism*, *Mon. Not. Roy. Astron. Soc.* **331** (2002) 463, [astro-ph/0111532].

[186] **Planck** Collaboration, R. Adam et al., *Planck 2015 results. I. Overview of products and scientific results*, arXiv:1502.01582.

[187] M. Kuhlen and C. A. Faucher-Giguere, *Concordance models of reionization: implications for faint galaxies and escape fraction evolution*, *Mon. Not. Roy. Astron. Soc.* **423** (2012) 862–876, [arXiv:1201.0757].

[188] S. Furlanetto, M. Zaldarriaga, and L. Hernquist, *The Growth of HII regions during reionization*, *Astrophys. J.* **613** (2004) 1–15, [astro-ph/0403697].

[189] S. Bharadwaj and P. S. Srikant, *HI fluctuations at large redshifts. 3. Simulating the signal expected at GMRT*, *J. Astrophys. Astron.* **25** (2004) 67, [astro-ph/0402262].

[190] R. Mondal, S. Bharadwaj, S. Majumdar, A. Bera, and A. Acharyya, *The effect of non-Gaussianity on error predictions for the Epoch of Reionization (EoR) 21-cm power spectrum*, *Mon. Not. Roy. Astron. Soc.* **449** (2015), no. 1 L41–L45, [arXiv:1409.4420].

[191] A. Mesinger and S. Furlanetto, *Efficient Simulations of Early Structure Formation and Reionization*, *Astrophys. J.* **669** (2007) 663, [arXiv:0704.0946].

[192] R. K. Sheth and G. Tormen, *An Excursion set model of hierarchical clustering : Ellipsoidal collapse and the moving barrier*, *Mon. Not. Roy. Astron. Soc.* **329** (2002) 61, [astro-ph/0105113].

[193] H.-Y. Schive, T. Chiueh, and T. Broadhurst, *Cosmic Structure as the Quantum Interference of a Coherent Dark Wave*, *Nature Phys.* **10** (2014) 496–499, [arXiv:1406.6586].

[194] H.-Y. Schive, T. Chiueh, T. Broadhurst, and K.-W. Huang, *Contrasting Galaxy Formation from Quantum Wave Dark Matter, ψDM, with ΛCDM, using Planck and Hubble Data*, arXiv:1508.04621.

[195] J. Wang and S. D. M. White, *Discreteness effects in simulations of Hot/Warm dark matter*, *Mon. Not. Roy. Astron. Soc.* **380** (2007) 93–103, [astro-ph/0702575].

[196] M. R. Lovell, C. S. Frenk, V. R. Eke, A. Jenkins, L. Gao, and T. Theuns, *The properties of warm dark matter haloes*, *Mon. Not. Roy. Astron. Soc.* **439** (2014) 300–317, [arXiv:1308.1399].

[197] A. Schneider, R. E. Smith, and D. Reed, *Halo Mass Function and the Free Streaming Scale*, *Mon. Not. Roy. Astron. Soc.* **433** (2013) 1573, [arXiv:1303.0839].

[198] S. Agarwal and P. S. Corasaniti, *Structural properties of artificial halos in nonstandard dark matter simulations*, *Phys. Rev.* **D91** (2015), no. 12 123509, [arXiv:1503.03503].

[199] T. R. Choudhury, M. G. Haehnelt, and J. Regan, *Inside-out or Outside-in: The topology of reionization in the photon-starved regime suggested by Lyman-alpha forest data*, *Mon. Not. Roy. Astron. Soc.* **394** (2009) 960, [arXiv:0806.1524].

[200] S. Majumdar, S. Bharadwaj, and T. R. Choudhury, *The effect of peculiar velocities on the epoch of reionization (EoR) 21-cm signal*, *Mon. Not. Roy. Astron. Soc.* **434** (2012), no. 3 1978–1988, [arXiv:1209.4762].

[201] S. Bharadwaj and S. S. Ali, *On using visibility correlations to probe the HI distribution from the dark ages to the present epoch. 1. Formalism and the expected signal*, *Mon. Not. Roy. Astron. Soc.* **356** (2005) 1519, [astro-ph/0406676].

[202] R. Salvaterra and A. Ferrara, *Where are the sources of the near infrared background?*, *Mon. Not. Roy. Astron. Soc.* **367** (2006) L11–L15, [astro-ph/0509338].

[203] N. Kaiser, *On the Spatial correlations of Abell clusters*, *Astrophys. J.* **284** (1984) L9–L12.

[204] P. J. E. Peebles, *Principles of Physical Cosmology*. Princeton University Press, 1993.

[205] A. Lidz, O. Zahn, M. McQuinn, M. Zaldarriaga, and L. Hernquist, *Detecting the Rise and Fall of 21 cm Fluctuations with the Murchison Widefield Array*, *Astrophys. J.* **680** (2008) 962–974, [arXiv:0711.4373].

[206] S. K. Sethi and K. Subramanian, *Primordial magnetic fields and the HI signal from the epoch of reionization*, *JCAP* **0911** (2009) 021, [arXiv:0911.0244].

[207] J. C. Pober et al., *PAPER-64 Constraints on Reionization II: The Temperature of the $z = 8.4$ Intergalactic Medium*, *Astrophys. J.* **809** (2015), no. 1 62, [arXiv:1503.00045].

[208] B. Catinella, M. P. Haynes, R. Giovanelli, J. P. Gardner, and A. J. Connolly, *A Pilot Survey of HI in Field Galaxies at Redshift z 0.2*, *Astrophys. J.* **685** (2008) L13, [arXiv:0808.1180].

[209] A. M. Wolfe, D. A. Turnshek, H. E. Smith, and R. D. Cohen, *Damped Lyman-alpha absorption by disk galaxies with large redshifts. I - The Lick survey*, *ApJS* **61** (June, 1986) 249–304.

[210] A. M. Wolfe, E. Gawiser, and J. X. Prochaska, *Damped lyman alpha systems*, *Ann. Rev. Astron. Astrophys.* **43** (2005) 861–918, [astro-ph/0509481].

[211] P. Noterdaeme, P. Petitjean, C. Ledoux, and R. Srianand, *Evolution of the cosmological mass density of neutral gas from Sloan Digital Sky Survey II - Data Release 7*, *Astron. Astrophys.* **505** (2009) 1087, [arXiv:0908.1574].

[212] C. Peroux, R. G. McMahon, L. J. Storrie-Lombardi, and M. J. Irwin, *The evolution of omega(hi) and the epoch of formation of damped lyman-alpha absorbers*, *Mon. Not. Roy. Astron. Soc.* **346** (2003) 1103, [astro-ph/0107045].

[213] R. K. Sheth and G. Tormen, *Large scale bias and the peak background split*, *Mon. Not. Roy. Astron. Soc.* **308** (1999) 119, [astro-ph/9901122].

[214] A. Pontzen, F. Governato, M. Pettini, C. M. Booth, G. Stinson, J. Wadsley, A. Brooks, T. R. Quinn, and M. Haehnelt, *Damped Lyman Alpha Systems in Galaxy Formation Simulations*, *Mon. Not. Roy. Astron. Soc.* **390** (2008) 1349, [arXiv:0804.4474].

[215] A. Font-Ribera et al., *The large-scale cross-correlation of Damped Lyman Alpha Systems with the Lyman Alpha Forest: First Measurements from BOSS*, *JCAP* **1211** (2012) 059, [arXiv:1209.4596].

[216] B. Bozek, D. J. E. Marsh, J. Silk, and R. F. G. Wyse, *Galaxy UV-luminosity function and reionization constraints on axion dark matter*, *Mon. Not. Roy. Astron. Soc.* **450** (2015), no. 1 209–222, [arXiv:1409.3544].

[217] R. J. Bouwens et al., *UV Luminosity Functions from 113 z 7 and z 8 Lyman-Break Galaxies in the ultra-deep HUDF09 and wide-area ERS WFC3/IR Observations*, *Astrophys. J.* **737** (2011) 90, [arXiv:1006.4360].

[218] R. J. Bouwens et al., *UV Luminosity Functions at redshifts z ∼4 to z ∼10: 10000 Galaxies from HST Legacy Fields*, *Astrophys. J.* **803** (2015), no. 1 34, [arXiv:1403.4295].

[219] N. H. M. Crighton et al., *The neutral hydrogen cosmological mass density at z = 5*, *Mon. Not. Roy. Astron. Soc.* **452** (2015), no. 1 217–234, [arXiv:1506.02037].

[220] H.-Y. Schive, M.-H. Liao, T.-P. Woo, S.-K. Wong, T. Chiueh, T. Broadhurst, and W. Y. P. Hwang, *Understanding the Core-Halo Relation of Quantum Wave Dark Matter from 3D Simulations*, *Phys. Rev. Lett.* **113** (2014), no. 26 261302, [arXiv:1407.7762].

[221] A. F. Illarionov and R. A. Siuniaev, *Comptonization, the background-radiation spectrum, and the thermal history of the universe*, *Exp. Theor. Phys.* **18** (June, 1975) 691–699.

[222] G. Rybicki and A. Lightman, *Radiative processes in astrophysics*. WILEY-VCH Verlag GmbH & Co. KGaA, 1979.

[223] A. P. Lightman, *Double Compton emission in radiation dominated thermal plasmas*, *Astrophys. J.* **244** (Mar., 1981) 392–405.

[224] W. Hu and J. Silk, *Thermalization and spectral distortions of the cosmic background radiation*, *Phys. Rev.* **D48** (1993) 485–502.

[225] J. Bernstein and S. Dodelson, *Aspects of the Zel'dovich-Sunyaev mechanism*, *Phys. Rev.D.* **41** (Jan., 1990) 354–373.

[226] R. A. Sunyaev and Y. B. Zeldovich, *The interaction of matter and radiation in the hot model of the Universe, II*, *Astrophys. Space Sci.* **7** (Apr., 1970) 20–30.

[227] Y. Zeldovich and R. Sunyaev, *The Interaction of Matter and Radiation in a Hot-Model Universe*, *Astrophys. Space Sci.* **4** (July, 1969) 301–316.

[228] J. Chluba and R. A. Sunyaev, *The evolution of CMB spectral distortions in the early Universe*, *Mon. Not. Roy. Astron. Soc.* **419** (2012) 1294–1314, [arXiv:1109.6552].

[229] J. Chluba, *Green's function of the cosmological thermalization problem*, *Mon. Not. Roy. Astron. Soc.* **434** (2013) 352, [arXiv:1304.6120].

[230] R. Khatri and R. A. Sunyaev, *Beyond y and μ: the shape of the CMB spectral distortions in the intermediate epoch,* $1.5\text{x}10^4 < z < 2\text{x}10^5$, *JCAP* **1209** (2012) 016, [arXiv:1207.6654].

[231] W. Hu, D. Scott, and J. Silk, *Reionization and cosmic microwave background distortions: A Complete treatment of second order Compton scattering*, *Phys. Rev.* **D49** (1994) 648–670, [astro-ph/9305038].

[232] B. B. Nath and J. Silk, *Heating of the intergalactic medium due to structure formation*, *Mon. Not. Roy. Astron. Soc.* **327** (2001) L5, [astro-ph/0107394].

[233] E. Komatsu and U. Seljak, *The Sunyaev-Zel'dovich angular power spectrum as a probe of cosmological parameters*, *Mon. Not. Roy. Astron. Soc.* **336** (2002) 1256, [astro-ph/0205468].

[234] J. C. Hill, N. Battaglia, J. Chluba, S. Ferraro, E. Schaan, and D. N. Spergel, *Taking the Universe's Temperature with Spectral Distortions of the Cosmic Microwave Background*, *Phys. Rev. Lett.* **115** (2015), no. 26 261301, [arXiv:1507.01583].

[235] C. Burigana, L. Danese, and G. de Zotti, *Formation and evolution of early distortions of the microwave background spectrum - A numerical study*, *Astron. Astrophys.* **246** (June, 1991) 49–58.

[236] J. Chluba, *Distinguishing different scenarios of early energy release with spectral distortions of the cosmic microwave background*, *Mon. Not. Roy. Astron. Soc.* **436** (2013) 2232–2243, [arXiv:1304.6121].

[237] J. Chluba and D. Jeong, *Teasing bits of information out of the CMB energy spectrum*, *Mon. Not. Roy. Astron. Soc.* **438** (2014), no. 3 2065–2082, [arXiv:1306.5751].

[238] J. Chluba, E. Dimastrogiovanni, M. A. Amin, and M. Kamionkowski, *Evolution of CMB spectral distortion anisotropies and tests of primordial non-Gaussianity*, arXiv:1610.08711.

[239] N. Padmanabhan and D. P. Finkbeiner, *Detecting dark matter annihilation with CMB polarization: Signatures and experimental prospects*, *Phys. Rev.D.* **72** (July, 2005) 023508, [astro-ph/0503486].

[240] R. A. Sunyaev and Y. B. Zeldovich, *Small scale entropy and adiabatic density perturbations - Antimatter in the Universe*, *Astrophys. Space Sci.* **9** (Dec., 1970) 368–382.

[241] W. Hu, D. Scott, and J. Silk, *Power spectrum constraints from spectral distortions in the cosmic microwave background*, *Astrophys. J.* **430** (1994) L5–L8, [astro-ph/9402045].

[242] J. Chluba, R. Khatri, and R. A. Sunyaev, *CMB at 2x2 order: The dissipation of primordial acoustic waves and the observable part of the associated energy release*, *Mon. Not. Roy. Astron. Soc.* **425** (2012) 1129–1169, [arXiv:1202.0057].

[243] E. Pajer and M. Zaldarriaga, *A hydrodynamical approach to CMB μ-distortion from primordial perturbations*, *JCAP* **1302** (2013) 036, [arXiv:1206.4479].

[244] P. J. E. Peebles, *Recombination of the Primeval Plasma*, *Astrophys. J.* **153** (July, 1968) 1.

[245] J. A. Rubino-Martin, J. Chluba, and R. A. Sunyaev, *Lines in the Cosmic Microwave Background Spectrum from the Epoch of Cosmological Hydrogen Recombination*, *Mon. Not. Roy. Astron. Soc.* **371** (2006) 1939–1952, [astro-ph/0607373].

[246] J. Chluba and R. A. Sunyaev, *Cosmological hydrogen recombination: influence of resonance and electron scattering*, *Astron. Astrophys.* **503** (Aug., 2009) 345–355, [arXiv:0904.2220].

[247] N. Kaiser, *Small-angle anisotropy of the microwave background radiation in the adiabatic theory*, *Mon. Not. Roy. Astron. Soc.* **202** (Mar., 1983) 1169–1180.

[248] S. Weinberg, *Entropy Generation and the Survival of Protogalaxies in an Expanding Universe*, *Astron. Astrophys.* **168** (Sept., 1971) 175.

[249] L. Danese and G. de Zotti, *The relic radiation spectrum and the thermal history of the Universe*, *Nuovo Cimento Rivista Serie* **7** (Sept., 1977) 277–362.

[250] W. Hu and J. Silk, *Thermalization and spectral distortions of the cosmic background radiation*, *Phys. Rev.D.* **48** (July, 1993) 485–502.

[251] S. Dodelson, *Modern cosmology*. Academic Press, 2003.

[252] R. Khatri, R. A. Sunyaev, and J. Chluba, *Mixing of blackbodies: entropy production and dissipation of sound waves in the early Universe*, *" Astron. Astrophys."* **543** (July, 2012) A136, [arXiv:1205.2871].

[253] L. Hui, J. P. Ostriker, S. Tremaine, and E. Witten, *On the hypothesis that cosmological dark matter is composed of ultra-light bosons*, arXiv:1610.08297.

[254] S. Agarwal, P. S. Corasaniti, S. Das, and Y. Rasera, *Small scale clustering of late forming dark matter*, arXiv:1412.1103.

[255] R. Hložek, D. J. E. Marsh, D. Grin, R. Allison, J. Dunkley, and E. Calabrese, *Future CMB tests of dark matter: ultra-light axions and massive neutrinos*, arXiv:1607.08208.

[256] A. Kogut et al., *The Primordial Inflation Explorer (PIXIE): A Nulling Polarimeter for Cosmic Microwave Background Observations*, *JCAP* **1107** (2011) 025, [arXiv:1105.2044].

[257] S. Bharadwaj and S. K. Sethi, *Decaying Neutrinos and Large-Scale Structure Formation*, *"Astrophys.J"* **114** (Jan., 1998) 37–57, [astro-ph/9707143].

[258] K. Ichiki, M. Oguri, and K. Takahashi, *Constraints from the Wilkinson Microwave Anisotropy Probe on Decaying Cold Dark Matter*, *Physical Review Letters* **93** (Aug., 2004) 071302, [astro-ph/0403164].

[259] J. Chluba, A. L. Erickcek, and I. Ben-Dayan, *Probing the inflaton: Small-scale power spectrum constraints from measurements of the CMB energy spectrum*, *Astrophys. J.* **758** (2012) 76, [arXiv:1203.2681].

[260] S. Clesse, B. Garbrecht, and Y. Zhu, *Testing Inflation and Curvaton Scenarios with CMB Distortions*, *JCAP* **1410** (2014), no. 10 046, [arXiv:1402.2257].

[261] L. V. E. Koopmans, *Gravitational-mass imaging of CDM substructure*, *Mon. Not. Roy. Astron. Soc.* **363** (2005) 1136, [astro-ph/0501324].

[262] Y. Hezaveh, N. Dalal, G. Holder, M. Kuhlen, D. Marrone, N. Murray, and J. Vieira, *Dark Matter Substructure Detection Using Spatially Resolved Spectroscopy of Lensed Dusty Galaxies*, *ApJ* **767** (Apr., 2013) 9, [arXiv:1210.4562].

[263] Y. Hochberg, T. Lin, and K. M. Zurek, *Absorption of light dark matter in semiconductors*, *Phys. Rev.* **D95** (2017), no. 2 023013, [arXiv:1608.01994].